Tidal Disruption Events in the Era of the Large Synoptic Survey Telescope: Testing the Supermassive Black Hole Mass Distribution

Katja Bricman

Center for Astrophysics and Cosmology, University of Nova Gorica, Vipavska 13, SI-5000 Nova Gorica

Abstract

The Large Synoptic Survey Telescope (LSST) will produce a multi-color survey of 25000 deg^2 of Southern sky during its 10 years of operations. Besides observing a large number of galaxies, stars, Solar System objects and probing the dark matter and the dark energy, it is also expected to discover thousands of transients every night. Due to its large coverage of the sky and its cadence it will be a perfect tool in search for rare Tidal Disruption Events (TDEs), which occur when a star passes close by a supermassive black hole (SMBH) and gets disrupted by its tidal forces. These events emit a bright flare of light and can be observed to cosmological distances. In this work we aim to address the prospects of the LSST in discovering TDEs and probing the SMBH mass distribution in the Universe. With the LSST simulation framework we have simulated observations of TDEs in a small field of 25 deg^2 of the sky, centered on $\alpha = 180^\circ$ and $\delta = -45^\circ$. From the resulting light curves we have studied the distributions of detected TDEs over the SMBH mass and compare them to the underlying distributions of SMBH masses in TDE host galaxies, which we used as an input for our simulations. We find that the LSST should detected between 10^3 and 10^5 new TDEs and that from their distribution over black hole mass, it is possible to predict whether an observed sample of TDEs follows any of the input distributions.

Keywords: stars:black holes, telescopes, surveys

1. Introduction

The Large Synoptic Survey Telescope (LSST, [1]) is an upcoming ground based sky survey project, which will conduct a 10 year long survey of the dynamic Universe and will be able to map the entire visible sky in just a few nights. With its large field of view of 9.6 deg^2 and its ability to achieve very faint magnitudes, up to 24.5 in optical *r* band, the LSST will map tens of billions of stars and galaxies in optical wavelengths, and by doing so, create a multi-color overview of the Universe [2, 3]. It will monitor 25000 deg^2 of the visible sky in the Southern hemisphere, and will enable studies of small objects in the Solar System, the structure of the Milky Way, galactic evolution, transients, properties of dark matter and dark energy, and discoveries of new astrophysical objects.

Images obtained with the LSST will be analyzed straight away in order to identify any objects that might have changed their brightness since the previous observation, or that might have moved. Therefore, the LSST will be a powerful tool in search for transients, including Tidal Disruption Events (TDEs), a phenomenon observed when a star is torn apart by the tidal forces of a supermassive black hole (SMBH).

TDEs are one of the most promising phenomena which enable the studies of SMBHs found in centers of most galaxies. A star passing close enough to an otherwise quiescent SMBH gets disrupted due to the strong tidal force [4, 5], emitting a bright flare of light, which then decays on time scales from months to years.

The observed emission of a TDE depends on different parameters concerning the objects and orbital dynamics involved, such as the mass of the black hole, the mass of the star, the radius of the star, the composition of the star, the distance from the black hole at which the star gets disrupted, and many others [6–11]. Therefore, it is reasonable to expect that the observed light curves of these events would provide us with information about the SMBHs in the centers of galaxies.

TDEs are rare events, with only around 70 candidates discovered so far. In this work we present the first results on the simulated observations of TDEs with the upcoming LSST project. For our simulations we used a unique approach, that has so far not

been explored yet. We have simulated TDE observations with the LSST simulation framework [1, 12–14], which includes all the components which may largely affect the data provided, from the design of the telescope, to conditions at the observing site, and the survey strategy. We used the simulation framework to reproduce the LSST observations of TDEs in 10 years on a small field of the sky covering 25 deg^2 centered on right ascension $\alpha = 180°$ and declination $\delta = -45°$. We used two different models for TDEs, a theoretical one [7, 9]) and `MOSFiT` model, which is based on the hydrodynamical simulations of TDEs [10, 11].

One of the inputs for our simulations was also the distribution of the SMBHs over their masses, which is still ambiguous, especially at the low mass end. For this purpose, we have used eight different distributions [15, 16] assuming all SMBHs in the Universe should follow a global distributions over mass, which may or may not vary only with the redshift. We compared the resulting sample of SMBH masses to the input distributions to test whether the simulated properties of TDEs coincide with the initial SMBH mass distribution.

This work is organized as follows: in section 2 we describe the theoretical background to the problem at hand by introducing some of the main characteristics of the LSST and its simulation framework in 2.1, TDEs in 2.2, and the spectral energy distribution (SED) models we used in our simulations (2.2.2, 2.2.3). Then, we continue by introducing different SMBH mass distributions we used as an input for our simulations in 2.3, describe our simulations in 3 and present our results in 4.

2. Theoretical background

2.1. LSST

LSST is an upcoming ground based system in Northern Chile, with its main purpose being wide field astronomical imaging. The LSST will survey the visible Southern sky in six optical bands u, g, r, i, z and y, covering the wavelength range between 320 nm and 1050 nm [1]. With its large field of view of 9.6 deg^2, the telescope will cover wide portions of the sky with declination $<+35.5°$ each night. Its large primary mirror with 8.4 m in diameter will enable imaging to very faint magnitudes, up to 24.5 in r band in a single exposure [2, 17]. The survey will cover 10000 deg^2 per night and will continuously scan a total of 25000 deg^2 of the sky [3], thus producing photometric and astrometric data on at least 20 billion objects. Objects that are otherwise rare will be commonly observed, and discoveries of yet unknown objects are expected.

Each visit to a given field of the sky will consist of two 15 second exposures, made with a 3.2 Gpx camera [18]. The same field will be visited again in a time interval raging from 1 hour to 3 days, based on the following ranking algorithm [3]. After a visit of a given field, all possible next observations will be assigned a score, which will depend on their locations, times of previous observations and filters. Therefore, the cadence (i.e. the next visit to the same field) of observations will be irregular, and some fields might be visited more frequently than the others [1].

LSST's capabilities will enable fast and deep imaging of the whole visible sky on short time scales, which will, among other things, be an important tool in discovering transient astrophysical sources. To understand how different components of the telescope, such as its design, the conditions at the observing site, and the observing strategy will affect the properties of the produced data, a simulation framework has been designed in order to simulate the whole operation of the telescope [1, 12–14]. The simulator can be used to simulate the observations of different astrophysical objects the LSST should provide in its 10 years of observations. From simulations of Solar System objects to the most distant active galaxies in the Universe, the LSST simulator also enables simulating observations of transient events. For the purpose of this paper, we have for the first time included TDEs into the LSST simulator, and simulated their observations.

The simulation framework consists of catalogs of astronomical objects, `CatSim` [13], a tool for simulating the operation of the telescope `OpSim` [14], and a tool for image simulations `PhoSim` [19]. `CatSim` is the base catalog of the simulations, containing catalogs of Solar System objects, stars, galaxies, and transients. It represents a view of the Universe above the Earth's atmosphere. `OpSim` uses data from the `CatSim` and simulates the LSST observations. It contains detailed models of atmospheric site conditions, telescope hardware performance, and observations scheduler. Each simulated pointing of the telescope provides a sky position and time of the observations, with corresponding sky conditions such as seeing, Moon phase and angle, and sky brightness. Magnitudes of the sources are derived using the atmospheric and filter response functions. The resulting catalogs from `OpSim` are then formatted for output to users or to be used as an input for `PhoSim`.

2.2. Tidal Disruption Events and SED Models

SMBHs, with masses ranging from 10^5 to 10^9 Solar masses, are common in the nuclei of galaxies, including our own [5]. Since nothing can escape black holes, not even light, it is generally challenging to study them. One way of detecting dormant

black holes in cores of galaxies is by studying TDEs. These events occur when a star passes the SMBH close enough, so that it gets disrupted by its tidal forces. TDEs produce luminous flares, which can be observed to cosmological distances. Most of the emitted energy is usually in optical and UV wavelengths, however some of the observed TDEs have been discovered in X-rays. To date, TDE observations in other wavelengths or messengers (such as gravitational waves, neutrinos or cosmic rays) have not been detected yet.

The rate at which the stars are disrupted depends on how the stars scatter off each other in the cores of galaxies. Dynamical models of stellar orbits in central regions of galaxies predict the rate of TDEs is $10^{-4} - 10^{-5}$ per galaxy per year [20]. Therefore, in a galaxy, only once in 10 000 to 100 000 years a star will be kicked into its fatal trajectory. Due to this low rate the events are rare, and large surveys monitoring hundreds of thousands of galaxies are more likely to catch TDEs.

2.2.1. *Dynamics of TDEs*

Consider a star of mass M_* and radius R_* moving on a highly eccentric orbit under the sole influence of the SMBH of mass $M_{\rm BH}$. If the distance of the closest approach to the black hole, the pericenter distance $R_{\rm p}$, lies within the tidal sphere with tidal radius

$$R_{\rm t} = R_* \left(\frac{M_{\rm BH}}{M_*} \right)^{1/3}, \tag{1}$$

then the tidal forces of the black hole overcome the star's self gravity, and the star is ripped apart [4]. The penetration factor is defined as the ratio of two distances $\beta = R_{\rm t}/R_{\rm p}$.

To simplify the model, we assume the star is on a parabolic orbit [7]. The minimum energy required for the star to be disrupted is of the order of star's self binding energy, $\frac{GM_*^2}{R_*}$. The star can be approximated as a point source in the gravitational field of the black hole at distances $r \gg R_{\rm t}$, however, its size becomes important when it approaches the tidal radius. Close to the tidal radius different fluid elements of the disrupting star lie at different distances to the black hole, which causes a sizable spread in specific orbital energy ϵ within the star. The parts furthest from the black hole have a positive specific binding energy, while the energy of parts closest to the black hole is negative [4]. If we assume the mass is uniformly distributed in the star, the specific energy spread can be estimated as [5]

$$\Delta\epsilon = \pm \frac{GM_*}{R_*} \left(\frac{M_{\rm BH}}{M_*} \right)^{1/3} = \pm \frac{GM_{\rm BH}}{R_{\rm p}^2} R_*. \tag{2}$$

Thus, approximately one half of the stellar debris (with $\epsilon < 0$) remains bound to the black hole, while the rest (with $\epsilon > 0$) becomes gravitationally unbound and escapes the black hole. Note that the ratio of bound and unbound debris might vary, if the stellar orbit is not parabolic.

The most bound matter, which is after the disruption on a highly eccentric orbit, returns back to the pericenter after one period, in time

$$t_{\rm fb} = \frac{2\pi G M_{\rm BH}}{(2\Delta\epsilon)^{3/2}}, \tag{3}$$

also called the fallback time. The rate, at which the material returns, is called the fallback rate $\dot{M}_{\rm fb}$ and it depends on the black hole mass, stellar mass and the internal structure of the disrupted star, more specifically, on the distribution of the mass over energy within the star. Assuming the latter distribution is flat [5], then the fallback rate scales with time as $\dot{M}_{\rm fb} \propto t^{-5/3}$. This behavior of the fallback rate is expected in the case of an idealized, incompressible star with a uniform density, which of course does not hold for typical stars. If we were to take a polytropic stellar model instead of a uniform one, then the the fallback rate would depart from the $t^{-5/3}$ behavior in the first few months after the disruption and would also result in a smaller peak fallback rate with a gentler rise to the peak, see [6].

The returning bound debris circularizes around the black hole and eventually forms an accretion disk [4]. The accretion disk is consumed by the black hole on a time scale from months to years. The gas in the disk is viscously heated as it is funneled down to the black hole, and therefore emits a flare of light, which fades as feeding subsides.

The fallback rate can be directly translated into the accretion rate onto the black hole, since the inflow time through accretion disk is $\ll t_{\rm fb}$ [7]. It is possible that, initially, the accretion rate exceeds the Eddington limit above which the outward radiation pressure wins over the gravity and only a small fraction of the material is accreted to the black hole, while the rest is blown away in a form of an outflow. The emission of the outflow is estimated to dominate the light curve on a time scale between a few weeks and a year. Afterwards the emission of the disk takes over.

The accretion disk forms just outside the black hole's event horizon, which lies at a distance of $R_{\rm S} = 2GM_{\rm BH}/c^2$ from the black hole [8]. Typically, $R_{\rm S} \ll R_{\rm t}$, however $R_{\rm S}$ grows faster with the mass of the black hole. Once it catches up with $R_{\rm t}$, the star disappears beyond the event horizon before it can be disrupted. There exist a limiting mass of the black hole, at which the black hole can still disrupt a star of certain radius and mass. For a Solar type star this limit is $10^8 M_\odot$.

2.2.2. Theoretical SED model

Based on the basic description of the dynamics of TDEs and assuming the emitted light of the TDE has two components, an outflow and an accretion disk, we constructed a theoretical model for light curves and spectral energy distributions (SEDs) of TDEs. Our treatment was similar to that in [7] and [9].

We assume the distribution of mass over energies inside the star is flat and that, in all cases, a Solar type star is being disrupted. This assumption might be too broad, since different types of stars are expected to orbit close enough to the central black hole to be disrupted. However, for now, we will assume most of the stars in the galactic centers are of Solar type and assume only such stars are being disrupted.

Initially, when the fallback rate is super-Eddington, the high radiation pressure results in an outflow of wind, which emits light from the photosphere, where the optical depth is of order unity [9]. The evolution of emission shows a relatively gentle rise with time and it reaches a peak luminosity of $10^{41} - 10^{43}$ erg/s at $t_{\rm fb}$. Afterwards, the density of the outflow falls and the emission declines with time as the fallback rate decreases. The photospheric radius, $R_{\rm ph}$, from which the light is emitted, declines in the same manner as does the fallback rate ($\propto t^{-5/3}$), however the corresponding temperature at this radius increases as $T_{\rm ph} \propto t^{25/36}$. Assuming the escaping photons have a black body spectrum, the resulting spectrum of the outflow evolves as

$$\lambda L_\lambda \sim 4\pi^2 R_{\rm ph}^2 \lambda B_\lambda(T_{\rm ph}), \tag{4}$$

where B_λ is the spectral radiance according to Planck's law. In the Rayleigh-Jeans approximation valid for optical wavelengths, the spectrum decreases with time as $t^{-95/36} \approx t^{-2.6}$.

The contribution of the accretion disk to the total spectrum of a TDE can be estimated by assuming a thin disk geometry, where the accretion rate follows a simple power-law decline at all times. If we keep the fraction of the mass ejected in an outflow at a constant, and assume the motion around the black hole is Keplerian, then the effective temperature of the disk as a function of radius can be calculated. For a more detailed calculation, see [9] and [21]. Using the relation for the effective temperature of the disk they obtained, we conclude that the spectrum of the disk scales as

$$\lambda L_\lambda \propto T_{\rm eff} \propto \dot{M}_{\rm fb}^{1/4} \propto t^{-5/12}. \tag{5}$$

Combining the two contributions, we were able to calculate the spectral energy distribution at any given time after the disruption. The theoretical SED models depend on the black hole mass $M_{\rm BH}$, stellar mass M_*, stellar radius R_*, penetration factor β, and the fraction of the mass, which is ejected as an outflow. We kept this fraction at a constant of 10%. In general, the first few days after the disruption are dominated by the outflow, whose peak is initially in the UV wavelengths. As the time passes, the outflow becomes hotter, but less luminous, and at the same time the disk emission becomes significant. At late times, the outflow emission subsides and only disk emission contributes to the luminosity. The peak of the SED moves to the optical wavelengths and the peak itself is decreasing.

2.2.3. MOSFiT model

In addition to testing a theoretical model described in section 2.2.2, we have also used a SED model calculated with The Modular Open Source Fitter for Transients, `MOSFiT` [22]. The problem with the theoretical model is that, even though it is simple and produces reasonable light curves, it often fails to describe previous observations of TDEs. The most obvious discrepancy is in the time evolution of the light curve. From the theoretical prediction, the light curve should evolve as $t^{-2.6}$ in the outflow phase and as $t^{-5/12}$ in the disk phase. However, most of the previous observations rather exhibit light curves with time evolution coinciding with that of the fallback rate, i.e. $t^{-5/3}$. In addition, the luminosity peak of the theoretical light curves is typically of order of two magnitudes smaller than that of the observed ones.

`MOSFiT` model, which uses `FLASH` simulations of the fallback rate [10], seems to solve the problem of the time evolution and peak luminosity of the light curves. With `MOSFiT`, previous observations of tidal disruption can be fitted, as was done in [11], and the model is observed to produce reasonable fits to the observed data (see Figure 1 in [11]).

From fitting the observations, the model can provide measurements on the black hole masses, penetration factors, stellar masses, type of the disrupted star, etc. However, `MOSFiT` might as well be used to generate SEDs of a generic TDE with desired input parameters.

For this purpose we have generated a library of SEDs for different events, where we have changed only two parameters: the black hole mass, and the penetration factor β. All of the events were assumed to include a Solar type star, described by a polytropic model with polytropic index $\gamma = 4/3$, and were placed at redshift $z = 0$, in order to obtain the intrinsic SEDs. Other input parameters (see [11], Table 1) for the `MOSFiT` model were kept at a constant.

2.3. *Supermassive Black Hole Mass Distributions*

One of the most important input parameters for our simulations, and evidently the one we wish to test, was the distribution of SMBHs in the centers of galaxies over their masses. We distributed the black hole masses in centers of galaxies in the LSST catalog simulator (see section 3 for more details) according to eight different distributions; we will call them `D1`-`D8`, all of which are plotted in Figure 1.

Distributions `D1` and `D2` and `D3` are derived by solving continuity equation of the final mass function of astrophysical sources and reconstructing the SMBH mass function from the active galactic nucleus (AGN) luminosity functions. The procedure for `D1` and `D2` is described in [15] and for `D3` in [16]. In all cases the resulting SMBH mass function is described by a modified Schechter function and results in a number of black holes in a $\log M_{\rm BH}$ bin per unit volume. Apart from the distribution `D2`, we have assumed that the parameters of the volume density of the SMBH mass do not change with redshift. The only thing that does change with redshift is the volume, using which leads us to results for the number density $n = N/V$. With `D2`, however, we have also allowed for the parameters to change with redshift, which means we have also taken into account that masses of SMBH are not stationary with time, but rather evolve from Solar mass black holes to SMBHs. All of the distributions described here only seem to be valid from $10^6 M_\odot$ on, however we have extrapolated them towards the low mass end as well (down to $10^5 M_\odot$).

Distributions `D4` and `D5` are artificially modified versions of distribution `D1` at low mass end of the SMBH mass distribution. In distribution `D4` we extrapolated the distribution below $10^6 M_\odot$ to be "flat" towards $10^5 M_\odot$, while `D5` was modified in a way that it shows a increasing tendency towards the peak at $10^{6.5} M_\odot$ and then decreases towards larger masses.

The remaining distributions were calculated using relations for the total stellar mass vs. black hole mass (`D6`), the dark matter halo mass vs. black hole mass (`D7`) and galaxy color vs. total stellar mass (`D8`). We have obtained the total stellar mass, the dark matter halo mass and colors of all of the galaxies from the `CatSim` database and have calculated the distributions of the black hole masses in the simulator. The relations we used were the following

$$\log\left(\frac{M_{\rm BH}}{M_\odot}\right) = 1.21 \log\left(\frac{M_*}{10^{11} M_\odot}\right) + 8.33 \qquad (6)$$

for `D6` [23], where M_* is the total stellar mass in the galaxy,

$$\log\left(\frac{M_{\rm BH}}{M_\odot}\right) = 1.33 \log\left(\frac{M_{\rm DM}}{10^{12} M_\odot}\right) + 7.85 \qquad (7)$$

for `D7` [24], where $M_{\rm DM}$ is the mass in the dark matter halo of a galaxy, and

$$\log\left(\frac{M_*}{M_\odot}\right) = 1.097(g-r) - 0.4\left(r - 5\log\frac{d}{10\,\mathrm{pc}}\right) - 0.19z + 1.462 \qquad (8)$$

for `D8` [25], where g and r are magnitudes of the galaxy in g and r bands. We then used equation (6) to get the corresponding black hole masses for `D8`.

3. Simulations

The light curves of tidal disruption events were simulated with the LSST simulation software stack [13, 14]. For the simulations, we have first generated a catalog of galaxies, which will host a TDE in 10 years of LSST operations and then used this catalog as a database, from which properties of simulated TDEs were drawn.

We assumed the rate of TDEs is 10^{-5} per galaxy per year and that only stars similar to the Sun ($M = M_\odot$, $R = R_\odot$, $\gamma = 4/3$) are disrupted. We queried the `CatSim` galaxy database, which covers approximately 25 deg^2 on the sky and contains around 17 million galaxies. We have centered our simulated field to right ascension $\alpha = 180^\circ$ and declination $\delta = -45^\circ$ to avoid being too close to the edge of the defined coordinates. We randomly chose TDE host galaxies based on the rate and the fact that one galaxy can experience only one TDE in 10 years of the LSST observations. We assigned each TDE a starting time, drawn randomly from the beginning to the end of the LSST era, and obtained a catalog of host galaxies with desired parameters (such as coordinates, redshift, extinction, etc.). At the same time we distributed the black hole masses according to 8 different distributions described in subsection 2.3, and randomly assigned them with β values.

For the `MOSFiT` model we let β vary from 0.6 to 4.0, where values between 0.6 and 1.8 correspond to a partial disruption, and values between 1.85 and 4.0 correspond to a full disruption of the star [10]. Both, partial and full disruption in this case produce flares, which are luminous enough to be detected.

In case of the theoretical model from subsection 2.2.2, we let β vary from 0.6 (partial disruption) to $11.8 M_{\rm BH}^{-2/3}$, which is the upper limit on β, if we let the pericenter passage to be well inside the tidal radius, at $2R_{\rm S}$. One does not expect the star to travel any further into the gravitational field of the black hole before it gets disrupted. In fact, we have ran several simulations using larger penetration factors

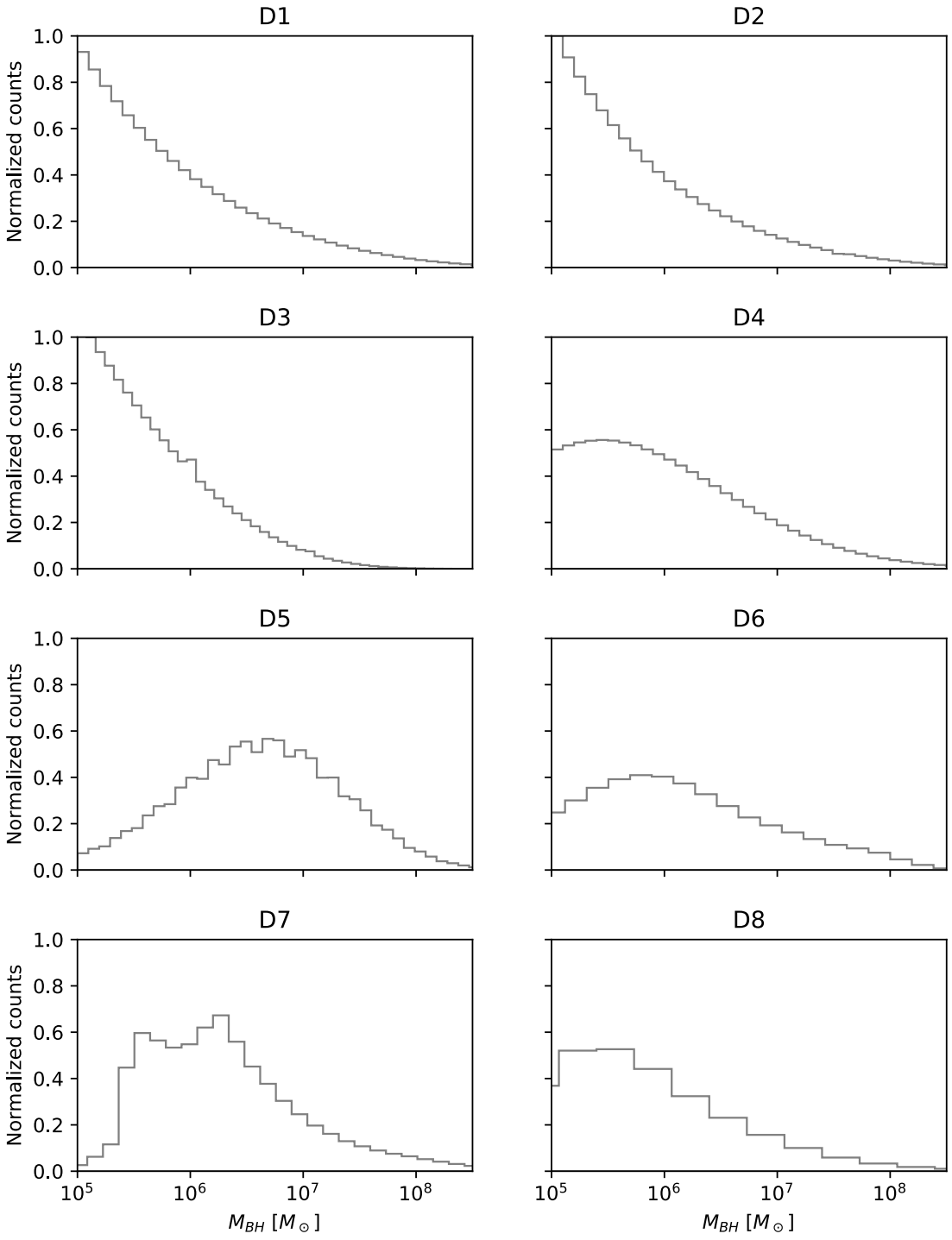

Figure 1: The initial supermassive black hole normalized count distributions in the simulation catalogue as a function of black hole mass $M_{\rm BH}$. The black hole masses of $\sim$ 17 million galaxies are distributed according to probability distributions `D1-D8`. The surface of each plot is normalized to 1.

β (corresponding to $R_S < R_p < 2R_S$), but those simulations did not produce any light curves, since the flux of these events was too small.

In principle, one would think that for the `MOSFiT` model the stars can also enter the tidal radius and travel all the way down to $2R_S$. However, [10] have noticed that larger β values do not produce any substantial change in the behavior of the fallback rate.

The resulting catalog with TDE host galaxies contained around 1700 members, including active galaxies (around 1% were AGNs), which we have eliminated from further investigation, since we do not know the nature of TDEs inside AGNs, and since it is usually assumed TDEs occur in non-active galaxies with preference towards E+A host galaxy type [26].

With the produced catalog we have simulated light curves of 1683 TDEs in the catalog eight times, one simulations for each of the input SMBH distributions. The whole procedure has been ran 3 times, meaning all in all we had to run 24 simulations. During the simulations, the internal dust and the Milky Way dust extinction were applied to each event according to the model in [27]. For every TDE, the flux was calculated by applying the cosmological redshift of the host galaxy to the SED [1]. The wavelengths were also redshifted with a LSST built-in function, which simply multiplies the emitted wavelength by $1 + z$.

Simulations of light curves were done in all six LSST bands, for galaxies with redshift $z < 3.0$, since events at larger redshifts are not expected to produce events bright enough to be observed. Based on α and δ, we queried the `Minion1016` database, which contains a simulated observing cadence of the LSST. At each time a certain TDE in the sky is observed, a point in the light curve is calculated along with an error-bar. The errors were calculated by the standard way used in the LSST light curve simulator.

Light curves of three simulated events are shown in Figure 2. The three events have different parameters and are at different redshifts. TDE1 is at $z = 0.078$, where the disrupting black hole has a mass of $M_{BH} = 4.27 \times 10^5 M_\odot$, and the penetration factor is $\beta = 5.1$. TDE2 is at $z = 0.242$, with $M_{BH} = 1.29 \times 10^6 M_\odot$ and $\beta = 4.8$, while TDE3 is at $z = 0.268$ with $M_{BH} = 1.42 \times 10^7 M_\odot$ and $\beta = 1.8$.

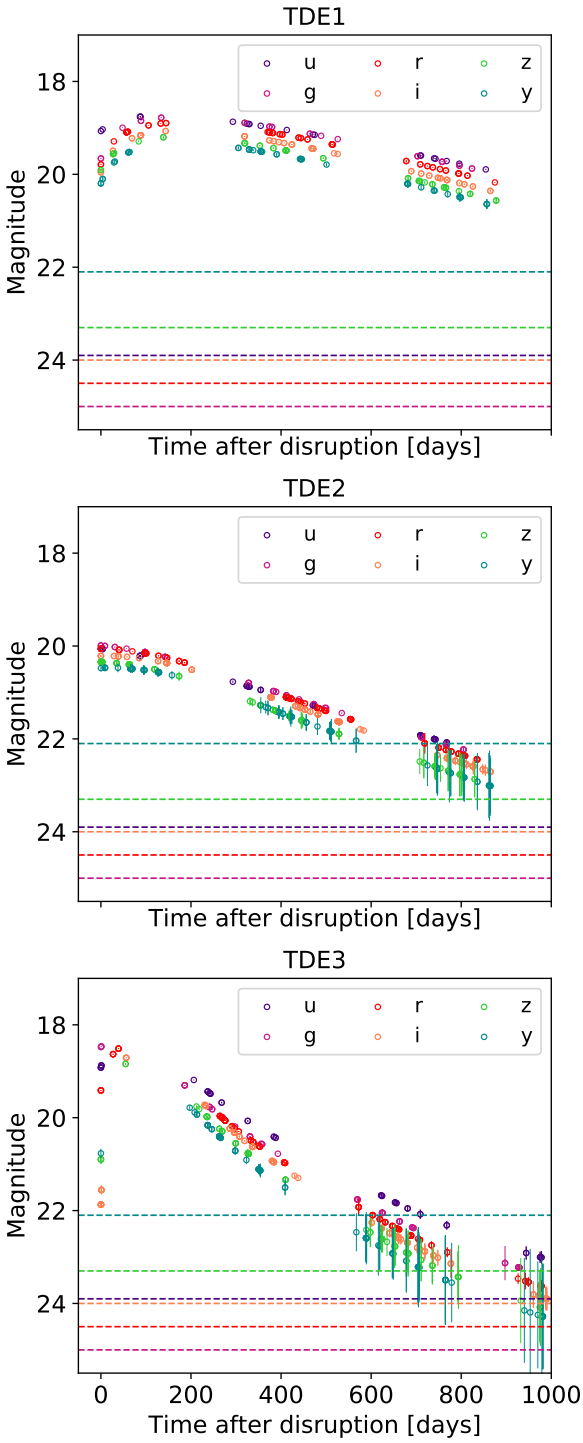

Figure 2: Simulated light curves of three different events in all six LSST bands (u, g, r, i, z and y). TDE1 is a disruption with redshift $z = 0.078$, $M_{BH} = 4.27 \times 10^5 M_\odot$ and $\beta = 5.1$, TDE2 at $z = 0.242$, $M_{BH} = 1.29 \times 10^6 M_\odot$ and $\beta = 4.8$, and TDE3 at $z = 0.268$, $M_{BH} = 1.42 \times 10^7 M_\odot$ and $\beta = 1.8$. Error-bars (vertical lines) are also plotted together with limiting magnitudes for each filter (horizontal dashed lines).

4. Results and discussion

Out of 1683 simulated TDEs we have included in our further analysis only those events, which had

[1] We assumed a flat Universe with cosmological parameters $\Omega_0 = 0.25$, $\Omega_\Lambda = 0.75$ and $H_0 = 73$ km/s/Mpc.

at least six observing points brighter than the limiting magnitude of the telescope in any of the LSST bands. Less observing points would mean one cannot assure a positive identification of the object as a TDE, since the recognition of these objects and their classification with the LSST are not well established yet. We chose six LSST observing points as a boundary for a positive identification of a discovered transient source being an actual TDE, however this number might actually be larger or become smaller once a well performing classification tool for identifying TDEs out of a large number of transients is produced.

Figure 3 shows the numbers of detected TDEs for each of the SMBH mass distributions discussed in 2.3 and for two SED models used: the theoretical SED model (section 2.2.2) and the `MOSFiT` model (section 2.2.3). Plotted are the expected numbers of TDEs with more than 6 observing points in 10 years of the LSST both on the simulated 25 deg^2 of the sky and on the whole sky observed by the LSST[2].

We expect the LSST should discover on average between 10^3 and 10^4 TDEs in case of using the theoretical SED model or 10^4 to 10^5 TDEs when using the `MOSFiT` model. Previous estimates have been done in [28] and in [2].In [28] the authors have estimated the LSST should discover around 40000 new TDEs in 10 years based on the previous observations, while in [2] this number was estimated to be 60000, based on the universal TDE rates from [29] and the references therein.

The final distributions of SMBHs of detected TDEs with more than six observations over the black hole masses for both models and all eight initial distributions are shown in Figure 4. In red the initial distributions are plotted, while the black histograms represent the results with the theoretical SED model and in green are shown the results with `MOSFiT` model. Ideally, we would expect the black and the green lines to follow the red line.

Despite the large difference in the number of detected TDEs based on the SED model, the shapes of the final BH mass distributions look quite similar. The peak of the distribution is always shifted towards larger BH masses for the theoretical SED model. This is justified by the fact that more massive black holes produce more luminous flares when disrupting a Yolar type star. Since the theoretical model is $\sim$ two orders of magnitude dimmer than the `MOSFiT` SED model, it requires a larger black hole mass to produce enough optical emission to be detected.

It is reasonable to assume that the `MOSFiT` SED model describes the underlying distribution better than the theoretical model, since it seems to sample the low mass end of the SMBH mass distribution more frequently than the theoretical SED model.

Except for a few initial distributions (`D1`, `D5` and `D7`) it is hard to say that the simulated distributions really follow the predicted distributions in the initial catalog of all galaxies in the field of 25 deg^2. The main reason for this is the small number of events which are detected in the simulated field on the sky. For a more accurate distribution, it would be reasonable to simulate TDEs on the whole sky and compare this final distribution to the initial distribution of BH masses in galaxies in `CatSim`. However, we realize, this would take much more computing time and power, since there are 17 million galaxies in 25 deg^2 only, and we expect the number on the entire sky observed by the LSST to be at least 3 orders of magnitude larger.

We emphasize that for a more realistic distributions, the simulations need to be ran over the whole observable sky and more times to get a better estimate on the systematic error. With this we could perhaps estimate which SED model is better and which initial SMBH distributions will be sampled the best. We expect that, if the number of detected TDEs in our simulations is large enough, the distribution of SMBH masses in the detected sample should converge to the initial distribution. However, as already discussed, some absence of representatives is expected towards the low mass end of the distributions, since it is heavier SMBHs that produce brighter events and it might happen, that even if a lower mass SMBH disrupts a star passing by, the flare is not bright enough to be seen from the Earth.

The low mass end of the SMBH mass distribution is believed to contain more members than the high mass end in almost every theoretical distribution proposed in the literature, however the low mass end of the distribution is currently still ambiguous. It would be interesting to see, whether the LSST will contribute to the exploration of this low mass end of the SMBH mass distribution and perhaps offer a validation of the model for the true mass distribution of SMBHs in the Universe.

Once the LSST will start observing TDEs on daily basis, the masses of black holes responsible for the triggering of the events will be determined by fitting the observed light curve with a TDE light curve model - either `MOSFiT` or the theoretical model in our case (or perhaps some other model, which can prove

[2]This area is 25000 deg^2 minus the part of the sky covered by the Milky Way, since we do not expect detections of extragalactic objects in optical wavelengths in the direction of the Milky Way. The size of the Milky Way on the Southern sky is 6500 deg^2, therefore we estimate detections on the area of 18500 deg^2 of the sky.

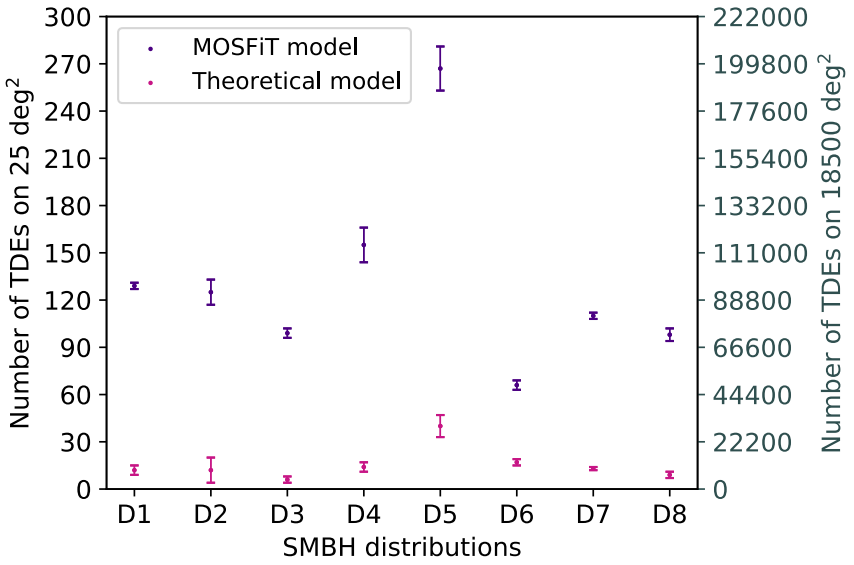

Figure 3: Number of detected TDEs with 6 or more observing points for both models used (`MOSFiT` and the theoretical model) for each of the distributions `D1-D8`. The number of detected TDEs was simulated on 25 deg^2 and this number was used to estimate the number of detected TDEs on the whole observable sky (25000 deg^2 - are of the Milky Way = 18500 deg^2). The uncertainties of the number of detections are the standard deviations from the mean calculated from resulting numbers of each simulation. Note that the uncertainties are not well determined yet, since the simulations have only been run a few times ($\sim$ 3) so far.

to describe previous observations of TDEs more accurately). Surely the follow-up observations will be vital for determining any of the parameters of the discovered TDE, due to the irregular LSST cadence. It will also be vital to classify the discovered TDE as an actual TDE as soon as possible after the detection, a problem which we plan to address in our future work.

5. Conclusion

Based on the results in Figure 3 we expect the LSST to discover on average between $10^4 - 10^5$ or $10^3 - 10^4$ TDEs in 10 years of observations, depending on which SED model was used to simulate the events. The `MOSFiT` model is of $\sim$ two orders of magnitude brighter than the theoretically predicted model we used in our work, therefore the number of detected TDEs is larger when applying `MOSFiT` to the events. It is reasonable to assume, that the LSST should extend our current sample of observed TDEs, the statistics concerning their properties, and should highly improve our understanding of TDEs.

The distributions of simulated detected TDEs are to some extent in agreement with the initial distribution of SMBHs in the LSST catalog. Based on the results shown in Figure 4, some preliminary decision on which distribution is the true underlying SMBH mass distribution could be made once the LSST will start observing TDEs by comparing the observed distribution to the predicted ones.

A more precise and well defined final distribution of the observed TDEs over their SMBH masses is expected, if the simulations would be done on the whole observable sky instead of a small patch. The number of observed TDEs would be much larger in this case, and we expect the observed SMBH mass distribution would converge towards the underlying one. Therefore, we conclude that discovering TDEs with the LSST promises a good chance of defining the true SMBH mass distribution in the Universe, or to at least omit some of the possible theoretical distributions predicted now. Moreover, we expect the LSST to largely improve our current understanding of TDEs and enable detailed studies of a large population of quiescent SMBHs residing in centers of most galaxies in the Universe.

References

[1] Ž. Ivezić, et al., preprint (2008). `arXiv:0805.2366`.

[2] P. A. Abell, et al., preprint (2009). `arXiv:0912.0201`.

[3] Ž. Ivezić, et al., Lsst science requirements document (2013).
URL `http://ls.st/LPM-17`

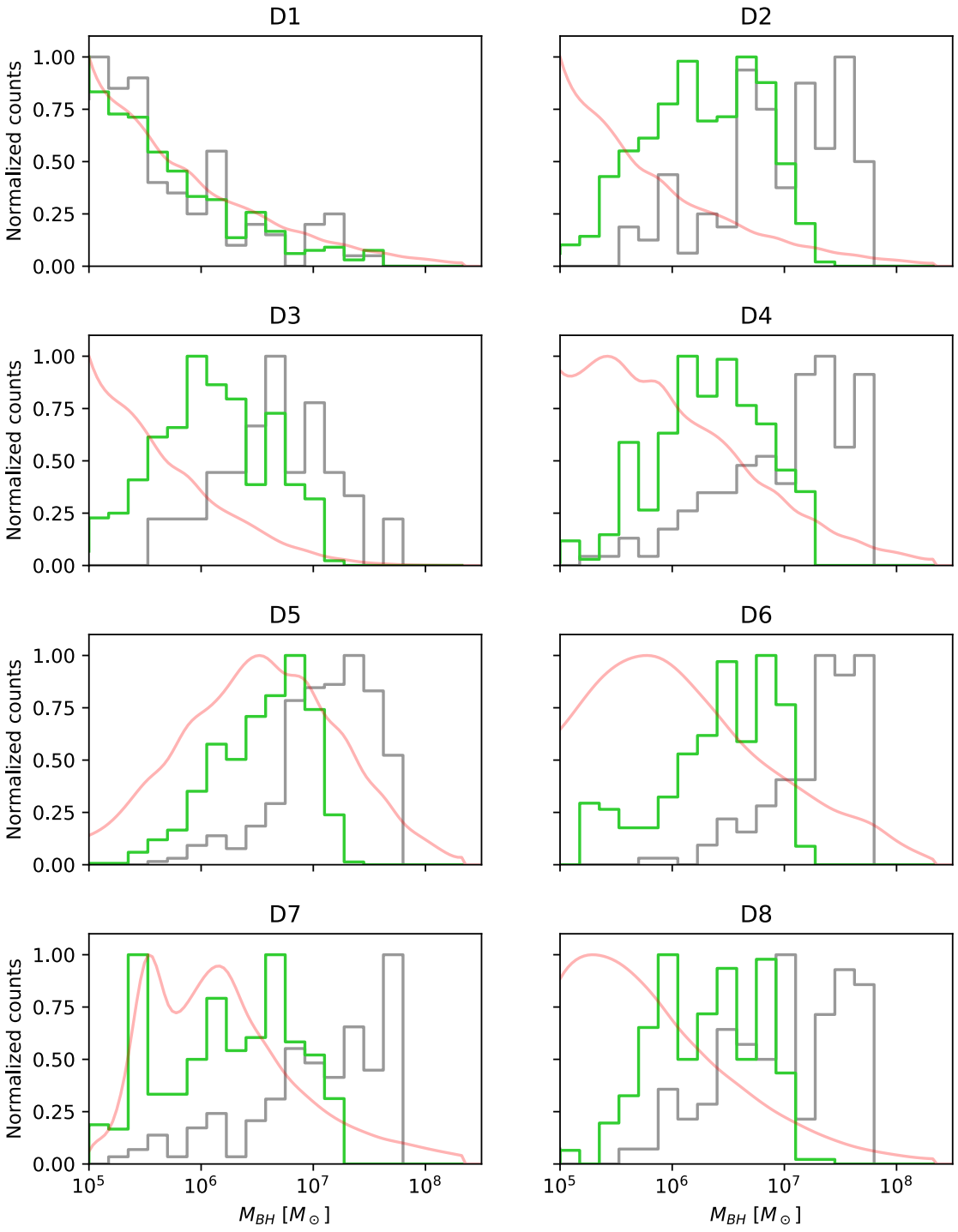

Figure 4: The resulting supermassive black hole normalized count distributions of host galaxies of the detected TDEs (with more than six observations) as a function of black hole mass $M_{\rm BH}$. The black lines represent the theoretical SED model, the green lines represent the `MOSFiT` SED model and the red lines are the initial distributions in the simulation catalog according to probability distributions `D1-D8` (same as in Figure 1, but approximated with a smooth line). The surface of each plot is normalized to 1

[4] M. J. Rees, Tidal disruption of stars by black holes of 10 to the 6th-10 to the 8th solar masses in nearby galaxies, Nature 333 (1988) 523–528. doi:10.1038/333523a0.

[5] E. S. Phinney, The center of the galaxy, IAU Symposium 136 (1989) 345.

[6] G. Lodato, A. R. King, J. E. Pringle, Stellar disruption by a supermassive black hole: is the light curve really proportional to $t^{-5/3}$?, MNRAS 392 (2009) 332. arXiv:0810.1288, doi:10.1111/j.1365-2966.2008.14049.x.

[7] G. Lodato, E. Rossi, Multiband lightcurves of tidal disruption events, MNRAS 410 (2011) 359. arXiv:1008.4589, doi:10.1111/j.1365-2966.2010.17448.x.

[8] S. Gezari, et al., The tidal disruption of stars by supermassive black holes, Physics Today 67 (2014) 37. doi:10.1063.PT.3.2382.

[9] L. E. Strubbe, E. Quataert, Optical Flares from the Tidal Disruption of Stars by Massive Black Holes, MNRAS 400 (2009) 2070. arXiv:0905.3735, doi:10.1111/j.1365-2966.2009.15599.x.

[10] J. Guillochon, E. Ramirez-Ruiz, Hydrodynamical Simulations to Determine the Feeding Rate of Black Holes by the Tidal Disruption of Stars: The Importance of the Impact Parameter and Stellar Structure, ApJ 767 (2013) 25, [Erratum: ApJ798,no.1,64(2015)]. arXiv:1206.2350, doi:10.1088/0004-637X/798/1/64,10.1088/0004-637X/767/1/25.

[11] B. Mockler, J. Guillochon, E. Ramirez-Ruiz, preprint (2018). arXiv:1801.08221.

[12] A. J. Connolly, et al., Simulating the lsst system, in: Proceeding of the SPIE, Vol. 778, 2010.

[13] A. J. Connolly, et al., An end-to-end simulation framework for the large synoptic survey telescope, in: Proceeding of the SPIE, Vol. 9150, 2014.

[14] F. Delgado, M. A. Reuter, The lsst scheduler from design to construction, in: Proceeding of the SPIE, Vol. 9910, 2016.

[15] R. Aversa, et al., Black Hole and Galaxy Coevolution from Continuity Equation and Abundance Matching, ApJ 810 (1) (2015) 74. arXiv:1507.07318, doi:10.1088/0004-637X/810/1/74.

[16] P. F. Hopkins, G. T. Richards, L. Hernquist, An Observational Determination of the Bolometric Quasar Luminosity Function, ApJ 654 (2007) 731–753. arXiv:astro-ph/0605678, doi:10.1086/509629.

[17] W. J. Gressler, Lsst telescope and site status, in: Proceeding of the SPIE, Vol. 9906, 2016.

[18] S. M. Kahn, et al., Design and development of the 3.2 gigapixel camera for the large synoptic survey telescope, in: Proceeding of the SPIE, Vol. 7735, 2010.

[19] J. R. Peterson, et al., Simulations of astronomical images from optical survey telescopes using a comprehensive photon monte carlo approach, The ApJ Supplement Series 218.1 (2015) 14.

[20] J. Magorrian, S. Tremaine, Rates of tidal disruption of stars by massive central black holes, MNRAS 309 (1999) 447. arXiv:astro-ph/9902032, doi:10.1046/j.1365-8711.1999.02853.x.

[21] S. L. Shapiro, S. A. Teukolsky, Black Holes, White Dwarfs and Neutron Stars, Wiley-VCH Verlag GmbH, 1983, ch. 14.5.

[22] J. Guillochon, M. Nicholl, V. A. Villar, B. Mockler, G. Narayan, K. S. Mandel, E. Berger, P. K. G. Williams, MOSFiT: Modular Open-Source Fitter for Transients, ApJ Suppl. 236 (1) (2018) 6. arXiv:1710.02145, doi:10.3847/1538-4365/aab761.

[23] R. van den Bosch, Unification of the Fundamental Plane and Super-Massive Black Holes Masses, ApJ 831 (2016) 134. arXiv:1606.01246, doi:10.3847/0004-637X/831/2/134.

[24] T. Di Matteo, R. A. C. Croft, V. Springel, L. Hernquist, Black hole growth and activity in a lambda CDM universe, ApJ 593 (2003) 56–68. arXiv:astro-ph/0301586, doi:10.1086/376501.

[25] M. Bernardi, F. Shankar, J. B. Hyde, S. Mei, F. Marulli, R. K. Sheth, Galaxy luminosities, stellar masses, sizes, velocity dispersions as a function of morphological type, MNRAS 404 (2010) 2087. arXiv:0910.1093, doi:10.1111/j.1365-2966.2010.16425.x.

[26] J. Law-Smith, E. Ramirez-Ruiz, S. L. Ellison, R. J. Foley, Tidal Disruption Event Host Galaxies in the Context of the Local Galaxy Population, ApJ 850 (1) (2017) 22. arXiv:1707.01559, doi:10.3847/1538-4357/aa94c7.

[27] J. E. O'Donnell, R_v-dependent optical and near-ultraviolet extinction, ApJ 422 (1994) 158.

[28] S. van Velzen, et al., Optical discovery of probable stellar tidal disruption flares, ApJ 741 (2011) 73. arXiv:1009.1627, doi:10.1088/0004-637X/741/2/73.

[29] A. Rau, et al., Exploring the Optical Transient Sky with the Palomar Transient Factory, Publ. Astron. Soc. Pac. 121 (2009) 1334–1351. arXiv:0906.5355, doi:10.1086/605911.

Developing a real time photon search for The Astrophysical Multimessenger Observatory Network with the Pierre Auger Observatory

Lukas Zehrer*

Center for Astrophysics and Cosmology, University of Nova Gorica, Vipavska, 11c, 5270, Ajdovscina, Slovenia

Abstract

With the recent discovery of gravitational waves and high-energy cosmic neutrinos, we are witnessing the beginning of a new era in multimessenger astronomy. The exploration of the Universe through these new messengers, along with electromagnetic radiation and cosmic rays, gives us new insights into the most extreme energetic cosmic events, environments and particle accelerators. The large collection area of the Pierre Auger Observatory (PAO) and the availability of a variety of composition-sensitive parameters provide an excellent opportunity to search for photons in the cosmic ray flux above 10^{18} eV. Upper limits published previously, using data from the Observatory, placed severe constraints on top-down models. Now, the increase in exposure by more than a factor 2 since 2008 together with the combination of different observables means that the detection of GZK-photons predicted using bottom-up models is almost within reach. In this paper the status of these investigations and perspectives for further studies are summarized. Current results on triggering variables for photons from the PAO for The Astrophysical Multimessenger Observatory Network (AMON) are presented and their implications will be discussed.

Keywords: GZK effect, showers: air, photon: showers, showers: energy, cosmic rays, air showers, Ultra High Energy Photons, Pierre Auger Observatory, PAO, Trigger, New Triggers, MoPS and ToTd, data analysis, real time photon search, Astrophysical Multimessenger Observatory Network, AMON

1. Introduction

Multi-messenger astrophysics is a quest to use the messenger particles of all four of natures fundamental forces to explore the most energetic phenomena in the universe based on the coordinated observation and interpretation of disparate "messenger" signals. The four extrasolar messengers are electromagnetic (EM) radiation, gravitational waves, neutrinos, and cosmic rays (CRs). They are created by different astrophysical processes, and thus reveal different information about their sources. Just one example these facilities collectively promise is the resolution of the mystery surrounding the origins of ultra high energy cosmic rays (UHECR).

The main multi-messenger sources outside the heliosphere are expected to be compact binary pairs (black holes (BH) and neutron stars (NS)), supernovae, irregular neutron stars (INS), gamma-ray bursts (GRB), active galactic nuclei (AGN), and relativistic jets [1, 2].

In order to interpret cosmic ray observations, detailed modelling of propagation effects invoking all important messengers is necessary. There is a correlation between acceleration sites of UHE cosmic rays and the emission of high-energy photons and neutrinos. The observation and interpretation of these particles in different energy regimes in a so-called multi-messenger approach allows for maximizing the scientific information and will increase the chances of identifying the sources of UHE cosmic rays.

In addition to the nuclear component of the UHE Cosmic Rays, a substantial photon flux, with fractions up to 50% at the highest energies, is expected according to the predictions of the non-acceleration models. Fractions at the level of 0.1% expected from the decay of neutral pions produced in the interaction of nucleons with the cosmic microwave background (GZK effect). Discrimination between the different scenarios for the origin of the UHECR is possible, based on observables sensitive to the distinctive characteristics of extensive atmospheric showers (EAS). Deviation of data from expectations for showers induced by nuclear primaries can offer a clear signature for photons, detectable by fluorescence telescopes as well as by arrays of surface detectors.

The detection of primary photons at these extreme energies will open a new window to the Universe, with large impact also on fundamental physics. So far no observation of UHE photons has been claimed, but stringent limits on their fraction in the integral CR flux have been placed [3, 4]. These limits help to reduce uncertainties related to photon contamination in other air shower mea-

*Corresponding author
Email address: lukas.zehrer@ung.si (Lukas Zehrer)
URL: http://www.ung.si/en/research/cac/staff/ (Lukas Zehrer)

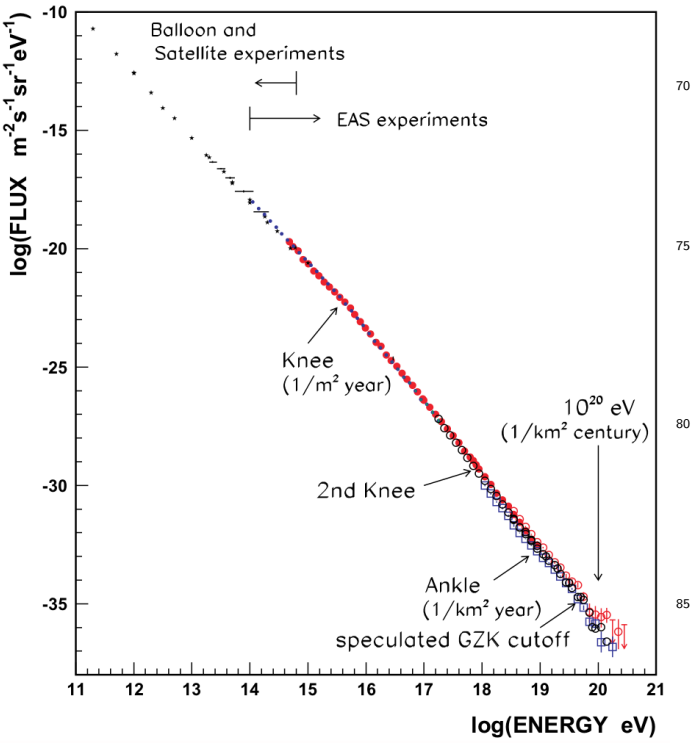

Figure 1: Energy spectrum of primary cosmic rays. Results from Akeno-AGASA, which cover the energy range (10^{15}-10^{20} eV), are shown by red closed and open circles. Direct observations with balloon- and satellite-borne detectors are plotted as dots below the knee, around 10^{15} eV. Tibet results, which cover the energy region below and above the knee, are plotted as blue circles. In the high- est energy region, results from HiRes and Auger are shown as open black circles and open blue squares, respectively. The overall spectrum is expressed by a power law from 10^{11} to 10^{20} eV with only small changes of slope around $10^{15.5}$ eV (the knee), $10^{17.8}$ eV (the second knee) and 10^{19} eV (the ankle). Figure taken from [5].

surements like the determination of the primary composition and of energy spectrum and the derivation of the proton-air inelastic cross-section.

The paper is structured as follows: In Section 2 I start with providing an introduction on observations in sec. 2.1 and 2.2. In 2.3 possible origins of cosmic rays are discussed. Section 2.4 explains the connection between cosmic rays and photons and what we can explore with them. In sec. 3 and 4 an short introduction to AMON and the PAO respectively is given. Section 5 presents a discussion of my work so far and an outlook of the work to be done, before sec 6 presents my summary and conclusions.

2. Ultra High Energy Photons

2.1. The energy spectrum of cosmic rays

The CR spectrum extends over many orders of magnitude, reaching energies above 10^{20} eV, this is millions of times greater than the energies achieved in the most powerful accelerators on Earth (see fig. 1).

Ultra high energy cosmic rays denotes a cosmic ray particle with kinetic energy $> 10^{18}$ eV and extreme energy cosmic ray (EECR) is a UHECR with energy exceeding $5{\cdot}10^{19}$ eV (about 8 joule), the so-called *GZK limit*. Experimental work is being done, gathering information about particles arriving at Earth, and also theoretical work regarding models of possible sources. In the high energy region of fig. 1 there are two important characteristics observed:

- The *ankle*, which could represent the transition from a galactic power-law behaviour (power-law energy flux of $J \propto E^{-\gamma}$) to an extragalactic contribution, or it could be a "dip" due to $e^{\pm}$ pair production in a cosmic-ray spectrum that is dominated by protons of extragalactic origin.
- A *cut-off* at $\approx 4{\cdot}10^{19}$ eV, which is found with more than 20σ significance and could be related to the GZK effect or to the maximum energy reached by the acceleration sources ("bottom-up" models).

The spectrum (fig. 1) flattens from a power law with index (3.29 ± 0.02(stat) $\pm$ 0.05(sys)) to one with index (2.60 ± 0.02(stat) $\pm$ 0.1(sys)) at $E_{ankle} = 4.8 \pm 0.1 \pm 0.8$ EeV. A clear suppression is observed at a significance in excess of 20σ beyond $E_s = 42.1 \pm 1.7 \pm 7.6$ EeV, the energy at which the differential flux is reduced to one-half of that expected from the extrapolation of the power law above the ankle. [6]

2.2. The GZK limit

The Greisen-Zatsepin-Kuzmin limit (GZK limit) is a theoretical upper limit on the energy of cosmic ray protons travelling from other galaxies through the intergalactic medium to our galaxy. The limit is $5 \cdot 10^{19}$ eV (or about 8 joules). The limit is set by slowing-interactions of the protons with the microwave background radiation over long distances ($\approx$ 160 million light-years). The limit is at the same order of magnitude as the upper limit for energy at which cosmic rays have experimentally been detected. The GZK limit is derived under the assumption that UHECRs are protons.

It is computed based on interactions between cosmic rays and the photons of the cosmic microwave background radiation (CMB). Predicted that cosmic rays with energies over the threshold energy of $5 \cdot 10^{19}$ eV would interact with CMB photons (γ_{CMB}), relatively blueshifted by the speed of the cosmic rays, to produce pions via the Δ-resonance,

$$\gamma_{CMB} + p \rightarrow \Delta^+ \rightarrow p + \pi^0 \ , \qquad (1)$$

or

$$\gamma_{CMB} + p \rightarrow \Delta^+ \rightarrow n + \pi^+ \ . \qquad (2)$$

Pions produced in this manner proceed to decay in the standard pion channels - ultimately to photons for neutral pions, and photons, positrons, and various neutrinos for

positive pions. Neutrons decay also to similar products, so that ultimately the energy of any cosmic ray proton is drained off by production of high energy photons plus (in some cases) high energy electron/positron pairs and neutrino pairs.

The pion production process continues until the cosmic ray energy falls below the pion production threshold. *Due to the mean path associated with this interaction, extragalactic cosmic rays travelling over distances larger than 50 Mpc (163 Mly) and with energies greater than this threshold should never be observed on Earth. This distance is also known as GZK horizon.*

The GZK limit should be the maximum energy of a cosmic ray protons, since higher-energy protons would have lost energy over that distance due to scattering from photons in the cosmic microwave background (CMB). It follows that EECR could not be survivors from the early universe, but are cosmologically "**young**", emitted somewhere in the Local Supercluster by some unknown physical process.

Measurements by the largest cosmic-ray observatory, the Pierre Auger Observatory (see sec. 4), suggest that most UHECRs are heavier elements. In this case, the argument behind the GZK limit does not apply in the originally simple form and there is no fundamental contradiction in observing cosmic rays with energies that violate the limit.

If an EECR is not a proton, but a nucleus with A nucleons, then the GZK limit applies to its nucleons, which carry only a fraction 1/A of the total energy of the nucleus. For an iron nucleus, the corresponding limit would be $2.8 \cdot 10^{21}$ eV. These particles are extremely rare; between 2004 and 2007, the initial runs of the Pierre Auger Observatory (PAO) detected 27 events with estimated arrival energies above $5.7 \cdot 10^{19}$ eV, i.e., about one such event every four weeks in the 3000 km^2 area surveyed by the observatory.

Given the small numbers of UHECRs on which the PAO results are based, some care must be taken with statistical methods, both to ensure that all the available information is utilised and to avoid over-interpretation. These aims are achieved by adopting a Bayesian approach in which the relevant stochastic processes (e.g. the GZK interactions of the UHECRs with the CMB, deflection by the Galaxys magnetic field, measurement errors) are explicitly modelled.

Even though the details of some of these processes are not well known (most relevantly the strength of the magnetic fields and the energy calibration of the UHECRs), such uncertainties are accounted for by marginalisation.

There is evidence that these highest-energy cosmic rays might be iron nuclei, rather than the protons that make up most cosmic rays. [7]

In the past, the apparent violation of the GZK limit has inspired cosmologists and theoretical physicists to suggest other ways that circumvent the limit. These theories propose that ultra-high energy cosmic rays are *produced nearby our galaxy* or that *Lorentz covariance is violated* in such a way that protons do not lose energy on their way to our galaxy.

These observations appear to contradict the predictions of special relativity and particle physics as they are presently understood. However, there are a number of possible explanations for these observations that may resolve this inconsistency.

- The observations could be due to an instrument error or an incorrect interpretation of the experiment, especially wrong energy assignment.
- The cosmic rays could have local sources well within the GZK horizon (although it is unclear what these sources could be).
- Cosmic rays are mostly heavier nuclei with A nucleons. This pushes the effective GZK limit for the whole nucleus up (factor A). For iron nuclei (the heaviest abundant element in cosmic rays) the corresponding energy limit is well beyond the energies of detected ultra-high-energy cosmic rays.

Several theoretical models present explanation of the non-observation of UHE photons possibly produced as a consequence of aforementioned scenarios. For example, in Lorentz Invariance Violation (LIV) scenarios based on the concept of photon decay (see Ref. [8] for a review on various concepts) the lifetime of a UHE photon would be extremely short ($\ll 1$ s), which would dramatically reduce its chances of reaching the Earth. On the other hand, one might approach observing the result of a UHE photon decay, an extensive cascade composed mainly of photons below the decay threshold. These cascades can be considered in a general way, regardless of the primary process, and call them cosmic-ray cascades (CRC) or *superpreshowers* (SPS, more see sec. 2.4.1) (per analogiam to the preshower effect of a UHE photon with the geomagnetic field - see e.g. Ref. [9] and references therein).

Several approaches to quantum gravity predict LIV at high energies (e.g. Horava-Lifshitz [10]). (Lorentz violations are allowed in string theory, supersymmetry and Horava-Lifshitz gravity.)

- If Lorentz-invariance is broken, the reaction threshold may be upshifted (and Universe becomes transparent for UHE photons) $\Rightarrow$ no observed cut-off [11]

2.3. Origin of cosmic rays

There are two different approaches that try to describe the origin of these UHECRs, namely due to particle acceleration, called "**bottom-up**" model and exotic models, called "**top-down**" model.

2.3.1. Particle acceleration - "*bottom-up*"

Here the four most prominent mechanisms are mentioned in short. The first is the *fermi acceleration* on shock waves, where the energy depends on the sources size, its magnetic field and the particle charge. The second source for UHECRs could be *supernova remnants*, which maximum energy attainable is limited ($\lesssim 10^{15}$ eV). Higher energies can be reached in larger objects or in stronger magnetic fields, with examples for this third solution: *active galactic nuclei* (AGN, also see sec. 2.4.2), or *colliding galaxies*. The high magnetic fields and strong astrophysical shocks observed in some of these objects are expected to be responsible for the acceleration of cosmic rays up to the highest observable energies. But its not certain if the particles with the highest observed energies can be produced there. And fourth the before mentioned GZK effect (interaction with microwave background photons) which limits the range of particles with the highest energies.

Gamma-ray bursts (GRBs) are just a small fraction of UHECR and would (probably) not contribute to the ultra high energy photons, because they come from far away, isotropically in the universe and loose most of the energy on its way.

Just to mention in short one of the models of GRBs that may contribute to *UHE photons* are the traditional or "classical" long-duration, high-luminosity gamma-ray bursts (HL-GRBs). They are the most common type of GRB detected by satellite experiments, being observed as bright seconds- to minutes-long bursts of γ-radiation from high-redshift (z=1). HL-GRBs are believed to arise when a massive star ($M \approx M_{\odot}$) undergoes a core collapse to a black hole (BH); confirmation of this "collapsar" model [12] for the HL-GRBs has been most dramatically provided by spectroscopic observations of ensuing type Ibc super-novae (SNe), with other lines of evidence also contributing [13].

2.3.2. Exotic models - "*top-down*"

Particles with the highest observed energies may not be the result of acceleration, but rather a product of interactions or decays of particles yet to be discovered directly.

Some of the proposed scenarios of cosmic ray production are *superheavy dark matter* (SHDM, [16–19]) - possibly concentrated near galaxies/clusters, which are metastable particles that could decay or annihilate, *relic topological defects* (TD; monopoles, cosmic strings or others [20, 21]) - which undergo decays and produce cascades of energetic particles, the before mentioned "*Z-Burst*" (ZB) model - in which highest energy neutrinos annihilate on background antineutrinos, producing Z bosons (Z-resonance) that decay into observed particles (producing secondary protons, neutrinos and photons) [22–24], and others [25–29].

All these models predict a large fraction of photons and neutrinos (tens of percent) in the cosmic rays of highest energies. And therefore ***UHE photons*** *would be a smoking gun for non-acceleration models!*

2.4. UHE Photons - γ_{UHE}

The search of UHE photons can help to solve these before-mentioned mysteries. The photon and the electron are observed fundamental particles and their interactions are well understood. Photons, as the gauge bosons of the EM force, at such enormous energy are unique messengers and probes of extreme and, possibly, new physics. Propagation features of UHE photons are sensitive to the MHz radio background [30]. The photon flux at Earth is also sensitive to extragalactic magnetic fields [31].

Already a small sample of photon-induced showers may provide relatively clean probes of aspects of quantum electrodynamics (QED) and quantum chromodynamics (QCD) at ultra-high energy via the preshower process and photonuclear interactions (see, e.g., [32]).

For sources more than a few tens of Mpc away the energy in the produced UHE-photon population may go into the development of a full electromagnetic cascade, with the energy flux arriving mainly at GeV-TeV energies, such sources either contributing to the diffuse gamma-ray background at these energies, or being individually resolvable in some scenarios, depending on the strength of the inter- or extragalactic magnetic fields. However, for a more nearby source, the electromagnetic cascades development has insufficient time to develop, with only the appreciable production of a first generation of UHE photons, leading to their contribution to the diffuse UHE photon background. *Thus, the search for UHE photons in the arriving UHECR flux can provide information about the* ***local*** *UHECR sources on these scales.*

Photon-induced showers are mostly electromagnetic with the first interaction dominated by electron-positron pair production in the Coulomb field. At the highest energies (above 10 EeV) two additional effects come into play: the Landau, Pomeranchuk and Migdal (LPM) effect and preshower in the geomagnetic field (for more see sec. 2.4.1).

It is interesting to check whether UHE photon propagation could be affected by the presence of axions or scalar bosons. The formal requirements for photon-axion conversion regarding photon energy and magnetic field strength, appear to be fulfilled [33]. Photon conversions to non-electromagnetic channels may differ from the standard QED process due to an absence of electromagnetic sub-cascade. Photon-axion conversion may ultimately increase the propagation distance of the UHE photons thus allowing to identify distant sources [34].

Above the GeV energy range, photons cannot conceivably be generated by thermal emission from hot celestial objects. Instead, UHE photons probe the non-thermal Universe where other mechanisms allow the concentration of large amounts of energy into a single particle. Typically, the production is associated with the decay of a neutral pion previously produced by a primary process (compare eq. (1)). UHE photons are mainly produced as either secondaries of the photo-pion production (GZK effect) of nuclei with a photon fraction at Earth of $\approx$ 0.1-1%

[35], or are a product in top-down models with a photon fraction at Earth of $\gtrsim 10\%$ (up to c.a. 50%) [36]. The main production process at UHE are photo-pion interactions where a nucleon N interacts with a background photon γ producing charged and neutral pions (see eq. (1) and (2)) in a GZK-type process. In the channel that conserves the charge of the original nucleon mostly neutral pions are produced which decay into secondary gamma rays

$$\pi^0 \quad \rightarrow \quad \gamma + \gamma \quad . \tag{3}$$

UHECR protons undergo these photo-pion interaction with background radiation fields (predominantly the CMB) producing both neutral and charged pions and hence a secondary UHE photon and neutrino flux around the source region. With the propagation of these UHE photons in turn being limited through $\gamma\gamma$ interactions with background photons, a region of space should exist around the source in which this UHE-photon flux is maximal. Due to the $\gamma\gamma$ cross-section and the dominant photon background targeting to these photons, the cosmic radio background (CRB) the interaction lengths for this process, above threshold, are a few Mpc. Thus, the distance for which the generated UHE photon flux is maximum would lie between a few Mpc and a few tens of Mpc from the source. It shall be noted here that though the CMB presents a much larger photon background target in terms of number density, the interaction of UHE photons (and UHE electrons) with it is suppressed due to the Klein Nishina suppression in the cross section for center-of-mass energies.

Depending on the energy of interest, other production mechanisms may become important, such as photons from photo-disintegration, elastic scattering, pair-production processes, radiative decay or synchrotron emission. The highest energies in the universe are only indirect accessible, e.g. via extensive air showers.

2.4.1. *Super-preshowers*

The complexity of the UHECR puzzle indirectly supports an alternative scenario that could be capable of generating UHE particles without an absolute need for correlation with the sources. While gravitational properties of SHDM particles are rather unquestioned, the distribution of SHDM particles seems to be disputable, e.g. not every galaxy can be an SHDM source. It is for instance not clear in the case of our Galaxy [37]. If SHDM distribution is not too far from uniform on a scale of super galaxy cluster, or if the propagation horizon of UHE photons is more limited than we extrapolate, we might not see SHDM sources. On the other hand, conclusions about the constraints on the sources or processes leading to the production of UHE photons require a number of fundamental assumptions concerning the electrodynamics at the grand unified theory (GUT) energies [38], hadronic properties of UHE photons, or space-time structure [39]. Also, modelling the propagation of UHE photons through the intergalactic, interstellar and even inter-

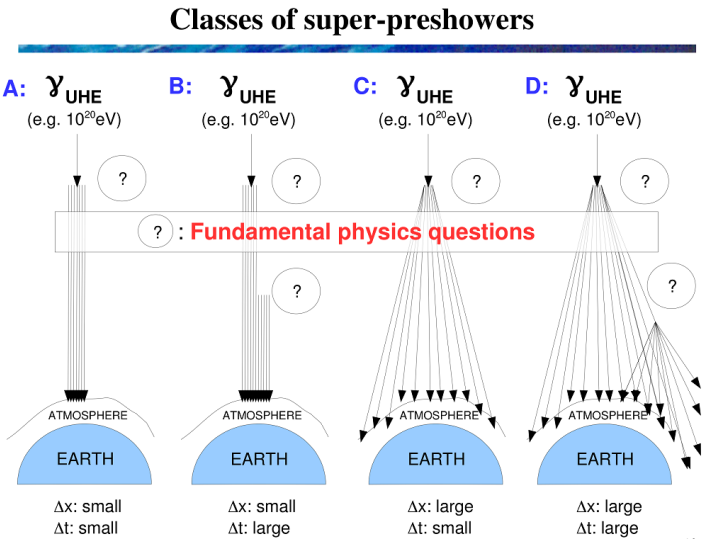

Figure 2: A basic observational classification of super-preshowers. Different classes refer to different widths of spatial and temporal distributions of super-preshower particles. The question marks represent the uncertainties about the fundamental physisc processes at E=10^{20} eV or larger. Figure taken from [41].

planetary medium requires assumptions difficult to verify. In addition uncertainty about the physics processes at GUT energies, i.e. expectations of deviations from the Standard Models in cosmology and particle physics because of the apparent difficulties in reconcilement between theories of General Relativity and Quantum Field Theory (see e.g. Ref. [40]). Therefore, any conclusions where the GUT uncertainties are involved, in particular the conclusions based on the *upper limits to UHE photons*, are disputable. Physical mechanisms which lead to a cascading of most of the UHE photons before they reach the Earth and consequently shrink their astrophysical horizon are illustrated in Fig. 2. Given the occurrence of such mechanisms or processes in reality, UHE photons have little chance to reach the Earth, and what can be observed on the Earth is the resulting particles most likely in a form of large electromagnetic cascades. One example of such a cascading process is the preshower effect [9] which is due to an interaction of a UHE photon and secondary electrons with the geomagnetic field. Although this does not produce an extended cascade, a generalized notion to the same phenomena to a UHE photon travelling towards the Earth through close distance of the Sun can produce an extended cascade at the Earth. Particles (mainly photons and a few electrons/positrons) in a cascade initiated due to preshower effect in the geomagnetic field have very narrow spatial and temporal extents and fall under class "A". For same effect occurring at the vicinity of the Sun, one would expect particles with narrow time distribution but large spatial extent as the cascade arrives at the top of the Earths atmosphere (class C). Also, other less known scenarios might cause distribution of arrival times of the particles quite extended with narrow spatial distribution

(class B), or both distributions are extended (class D).

2.4.2. UHE Photons from AGN

First-order Fermi acceleration in collisionless shocks is supposed to operate in the central regions of active galactic nuclei (AGNs). Most of the shock energy is channeled into relativistic protons. Protons are effectively "cooled" as a result of interactions with the soft radiation produced by accreting matter. Among final products of such collisions are UHE photons.

3. AMON

The Astrophysical Multimessenger Observatory Network (AMON) [44] provides a framework for correlating high energy astrophysical signals across all possible astronomical messengers: photons, neutrinos, cosmic rays, and gravitational waves.

The primary goals of the program are: (1) To allow participating observatories to share their data with one another with strict anonymity, confidentiality and in accordance with their blind analysis procedures, (2) to enhance the combined sensitivity of participating observatories to astrophysical transients by enabling them to search for coincidences in their sub-threshold archival data and then in their sub-threshold real-time data and (3) to enable follow-up imaging of possible astrophysical sources with minimal latency.

In addition, AMON stores events from participating observatories into its database to perform archival searches for significant coincidences. AMON also receives events and broadcasts them immediately to the astronomical community for follow-up.

AMON will weave together existing and forthcoming high-energy astrophysical observatories into a single virtual system, capable of sifting through the various data streams in near real-time, identifying candidate and high-significance multimessenger transient events, and providing alerts to interested observers. AMON represents a natural next step in the extension of the global astronomical communitys vision beyond the EM spectrum.

Detection from one messenger and non-detection from a different messenger can also be informative [45]. AMON is structured as an open and extensible network, with an Memorandum of Understanding (MOU) that allows straightforward incorporation of new triggering and follow-up facilities.

Participants in AMON can be characterized as either "*triggering*", "*follow-up*" or both. Triggering participants are generally wide field-of-view observatories that feed a stream of sub-threshold events into the AMON framework. These events are processed to search for temporal and spatial correlations, leading to AMON-generated "alerts". Follow-up participants generally search for electromagnetic counterparts to the alerts with high-throughput, smaller field-of-view instruments.

The sensitivities of the non-electromagnetic observatories are naturally limited, with rates of detection for transient events of publishable significance known or expected to be low, approximately a handful up to a few dozen per year. [46]

During the intervals prior to and between detection of these rare high-significance events, the multimessenger facilities will be buffeted by signals from a far greater number of lower-significance events that will be statistically indistinguishable from background or noise processes. Such "*subthreshold*" events are, by definition, unrecoverable as astrophysical signals in the data stream of any individual facility. However, if they are accompanied by a subthreshold signal in another multimessenger channel they can be identified, and potentially achieve high significance, via careful coincidence analysis of the data streams from multiple facilities. [46]

In this paper I present the scientific case of a real time photon alert of the Pierre Auger Observatory (PAO) for AMON and describe its important elements.

4. Pierre Auger Observatory - Triggers

The Pierre Auger Observatory is the world's largest ultra-high energy cosmic ray detector, located at an altitude of about 1400 m above sea level near Malarge, in the province of Mendoza, Argentina. It provides an unprecedented sensitivity to search for photons at UHEs due to its vast collecting area, and also a large integrated aperture for the search of photons with energy above 100 PeV. The observatory is a *hybrid* detector, a combination of a large surface detector array (**SD**) and fluorescence detectors (**FD**). The SD consists of 1660 water Cherenkov particle detectors of a surface of 10 m^2 each, covering an area of 3000 km^2 on a grid with 1.5 km spacing (SD-1500), and a smaller area extension to a lower energy threshold with an infill grid with a detector spacing of 750 m (SD-750). The FD includes 27 individual fluorescence telescopes overlooking the SD array from four different sites. There are also other extensions of the observatory not mentioned here, that can be looked up for example in Ref. [4]. While the SD has a duty cycle of nearly 100%, the FD can only operate on dark clear nights resulting in a duty cycle of 10-15%. The hybrid design of the Pierre Auger Observatory has a great advantage of providing a variety of composition-sensitive parameters, which offer an excellent opportunity to search for photons in the cosmic ray flux at ultra high energies.

Delayed air showers. The assumption of delayed air shower development is, that at the highest energies the pair production formation length gets elongated so much that the destructive interference of the fields associated with the atoms and particles nearby the primary suppresses the pair production process in the upper atmosphere, thus delaying the first interaction and the consequent air shower

development. This is so-called *LPM effect* [53-55], a standard in air shower modelling [56].

It is important to note that the LPM suppression is sensitive to the possible LIV effects including both increase and reduction of the pair production formation length. While the former would strengthen the UHE photon discrimination power based on delayed air shower development, the latter would do the opposite: reduce or even invert the LPM effect, and hence make photon-induced air showers develop more similarly to those initiated by nuclei.

The present state-of the art photon identification methods involving the expectation of a delayed development of an air shower induced by a photon assume the standard LPM effect, without any LIV effects.

4.1. The role of a triggering observatory in AMON

From all the possibilities within the PAO in this paper two topics are dealt with: the first is the contribution to real-time photon search with the Auger data, the second is to develop photon triggers for AMON for multi-messenger studies.

From the Auger datasets of interest to AMON are not the UHE hadrons (because they are deflected by (poorly known) magnetic fields and have therefore a delayed arrival), but the UHE Galactic neutrons, UHE photons and UHE neutrinos.

4.2. UHE Photons withe the PAO

The PAO provides an unprecedented integrated aperture for the search of photons with energy above 100 PeV. There are recent results including the diffuse search for photons and the directional search for photon point sources. The derived limits are of considerable astrophysical interest: Diffuse limits place severe constraints on top-down models and start to touch the predicted GZK photon flux range while directional limits can exclude the continuation of the electromagnetic flux from measured TeV sources with a significance of more than 5σ and also prospects of neutral particle searches for the upcoming detector upgrade AugerPrime are highlighted in Ref. [3] and [4].

There are two ways to search for photons, with its properties used for photons identification:

1. Events observed by SD-alone:
   - Radius of curvature R and;
   - Risetime $t_{1/2}$ (at 1000 m from the shower core);
2. Search for photons with hybrid events
   - (Larger) X_{max} (FD) - what means that γ-induced showers reach maximum deeper in the atmosphere than nucleonic ones, see fig. 3;
   - Signal at a given distance is smaller (SD);
   - Fewer triggered stations (SD);

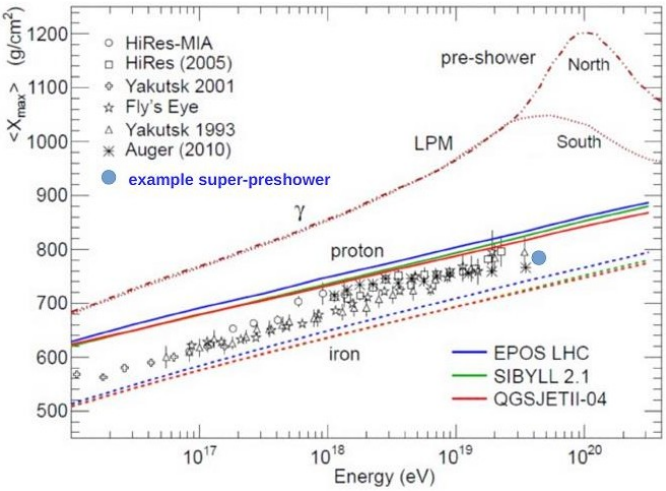

Figure 3: Variation of depth of air shower maximum with the primary energy: data collection and model predictions for different primaries. Figure taken from [41].

The two main discriminating observables, the radius of curvature of shower front and the time structure of shower front (risetime) are both correlated to X_{max}. A Larger X_{max} results in a larger curvature and therefore smaller radius. The reason for the risetime is due to the muonic component, since the μ are less delayed than e and γ. (The risetime is the time it takes the amplitude of the signal to go from 10% to 50%.)

The different variables can be combined to multivariate analysis observables. With UHE Photons (1-100 EeV), which have a loss length up to 30 Mpc (comp. fig. 4), there is the opportunity for AMON to identify nearby AGN flares, nearby sources of UHECRs (e.g. tidal disruptions, pulsars) and galactic sources. Another advantage of these UHE photon searches is the lower energy threshold than for neutrons. The AMON alerts with "photon"-like showers have a relaxed threshold compared to standard Auger searches.

The absence of point source photons does not mean that sources are extragalactic, they may be produced in transient sources (e.g. GRB or SN), may be emitted in jets not pointing to Earth, or may be EeV protons from sources with much lower optical depth (comp. to TeV sources).

4.2.1. Variables

Auger Triggers. The "new triggers" in Auger can be combined and used as a quick and rough discriminating observable. In June 2013, the Observatory installed across the entire array two additional SD T1 triggers [57]. These triggers build upon the ToT trigger in two ways, applying more sophisticated analysis to the event signal. The time-over-threshold-deconvolved (**ToTd**) trigger deconvolves the exponential tail of the diffusely reflected Cherenkov light pulses before applying the ToT condition. This has the effect of reducing the influence of muons in the trig-

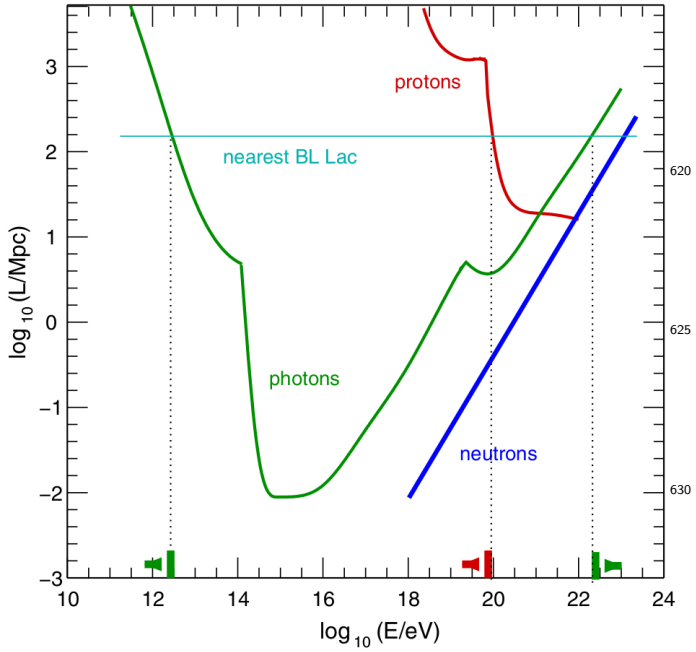

Figure 4: Attenuation length of different kinds of particles as compared to the distance to the nearest BL Lac (blue horizontal line) and the size of the Universe (upper bound of the plot). The green line corresponds to photons, blue to neutrons and red (shown for comparison) to protons. Figure taken from [34].

ger, since the typical signal from a muon, with fast rise time and ≈ 60 ns decay constant, is compressed into one or two time bins. The multiplicity-of-positive-steps trigger (**MoPS**), on the other hand, counts the number of positive-going signal steps in two of three photo-multiplier tubes (PMTs) within a 3 s sliding window. The steps are required to be above a small signal energy value (≈ 5·RMS noise) and below a moderate value (≈ 12 vertical muon step). This reduces the influence of muons in the trigger. Both the ToTd and MoPS triggers also require the integrated signal to be above ≈ 0.5 VEM. (The Cherenkov light recorded by a surface detector is measured in units of the signal produced by a muon traversing the tank on a central vertical trajectory. This unit is termed the Vertical Equivalent Muon (VEM). The goal of the surface detector calibration is to measure the value of 1 VEM in hardware units. During shower reconstruction, the signal recorded by the tanks is converted into units of VEM, and the total shower energy and arrival direction are fitted using a lateral distribution function and energy conversion based upon hybrid analysis using the FD measurements. The conversion to units of VEM is done both to provide a common reference level between tanks and to calibrate against the detector simulations.) Because these triggers minimize the influence of single muons, they reduce the energy threshold of the array, while keeping random triggers at an acceptable level. Thus they improve the energy reach of the SD, as well as improve the trigger efficiency for photon and neutrino showers. [4]

5. Data Analysis

The first steps in this work are to reproduce results (see fig. 5) from the earliest attempts in investigating and rough and quick discriminating variable to send an photon trigger from the PAO to AMON. This is done with data from Herald [61]. The CDAS (central data acquisition system) Herald is an automatic reconstruction running in the Lyon cluster. It uses the CDAS [4] reconstruction used to deliver the ICRC data set. The used herald distribution includes all data up to 31/5/2017. This version is corrected for weather and geomagnetic effects. Herald uses latest stable CDAS release to perform reconstructions for SD-1500 and SD-750 array. As is further described on the website, the ASCII format gives access to 48 shower reconstruction variables and quality. The website also lists a number of suggested cuts that should be applied.

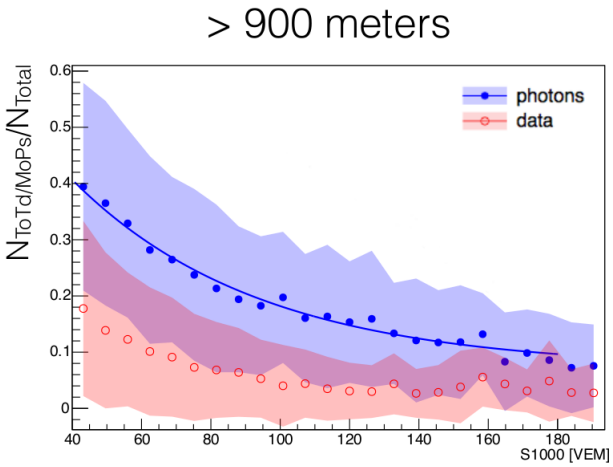

Figure 5: Preliminary results from previous working group obtained in 2015.

This rough and quick discriminating variable is the ratio of numbers of stations with new triggers to the number of all triggered stations plotted over another SD variable, S_{1000}.

5.1. Results and Discussion

In fig. 6 results are shown, using stations farther than a certain distance (900 m) from the shower axis, at a range where the difference between photon and hadron showers is more pronounced. A satisfactory qualitative agreement with the three-year old previous study has been found, see figures 5 and 6. The difference must be due to the evolution of the Auger analysis software.

For fitting the data in the selected region, in both figures 5 and 6, the following function

$$f(x) = p_0 + e^{p_1 + p_2 \cdot x} \quad (4)$$

has been used. The values of the best fit, the parameters p_0, p_1 and p_2, are provided in fig. 6.

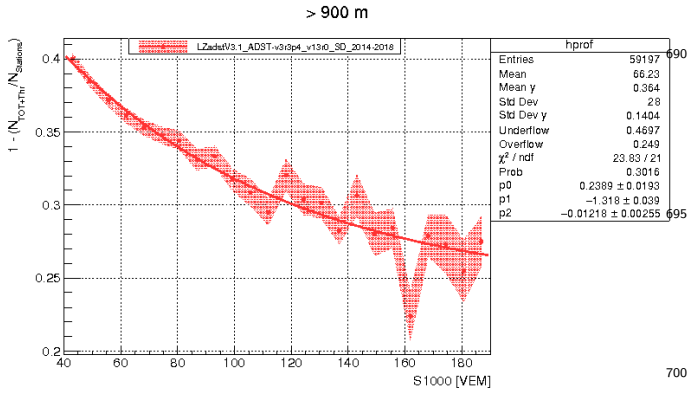

Figure 6: Trigger ratio vs S_{1000}.

6. Summary and Conclusion

In the highest observed energy region, the suppression of the flux above about $6{\cdot}10^{19}$ eV, which corresponds to the so-called "Greisen- Zatsepin-Kuzmin (GZK) cutoff energy", is confirmed by the results from the High-Resolution Flys Eye (HiRes) and the Pierre Auger Observatory (Auger). Summarizing the spectra observed from 10^{14} to 10^{20} eV with world wide experiments, there is still room for further investigations on the energy scale and the flux of primary cosmic rays. In order to establish the energy scale, it is necessary not only to understand the optical technique further, but also to determine the primary species in the highest energy region. Also, it is important to make more detailed measurements on the energy spectrum in the 10^{17} - 10^{18} eV region. To observe the super-GZK events and the anticipated recovery of the spectrum above the GZK cutoff, the search for the end of cosmic-ray energy spectrum will be continued even after a century since the discovery of cosmic rays in 1912.

The image of a mixed composition around the ankle and a heavier composition at the highest energies is strengthened by different composition studies, and by anisotropy searches at small angular scales at the highest energies. The present photon limits also disfavour pure proton composition models. Top-down models were already disfavoured by results on UHE neutrino and photon fluxes, leading to an astrophysical source explanation, but no clear clue on any existing UHECR source has been revealed so far. The hint of dipolar structure in the arrival direction is a step forward in the understanding of the transitions between the galactic and extragalactic components. The comparison of measurements with model predictions remains a delicate operation, knowing that serious hints for deficiencies in UHE interaction models have been observed. The astrophysical scenario resulting from Auger measurements is very complex and cannot at present be understood in terms of a unique interpretation for the sources, propagation and composition of the UHECRs. The great value of these overall results will be reinforced by the knowledge of the nature of the UHECR primaries, event by event. This will be the key to answering the open questions on the highest energy and the suppression region.

Search for ultra-high energy photons is an interesting field with high discovery potential. With new triggering algorithm and additional composition sensitivity of the planned upgrade of the Pierre Auger Observatory "*AugerPrime*" will increase the sensitivity to photons significantly. By 2024 it is expected to lower the photon limits with the PAO to reach the band of even conservative predictions for GZK photons - or discover ultra-high energy photons. It is expected that the limits will improve further, mainly at the low-energy end, due to optimized trigger algorithms. So it is just a matter of time until A) EeV photons are detected (with sufficient statistics), what would open a new window of astronomy, or B) the existence of EeV photons is disproved, what would role up the current understanding of physical principles. The directional search will also profit from the upgrade enabling sophisticated point source studies or even allow a detection of photons from specific sources.

The astrophysical puzzle is not only the pure existence of particles with energies exceeding 10^{20} eV, but added to the puzzle is the fact that the reconstructed directions of UHECRs do not point back to astrophysical sources [63].

Determining the UHECR mass composition, including identification of photons or setting upper limits on their fluxes ([4]), is an effort towards distinguishing between the two major classes which should give a hint on photon production and properties at the highest energies. Moreover, it is worth emphasizing that any result on UHE photons, including non-observation, is meaningful for the foundations of physics at the highest energies, allowing constraints on e.g. Lorentz invariance violation (LIV), QED nonlinearities, space-time structure or the already mentioned "top-down" scenarios (sec. 2.3.2). [3]

Acknowledgement

I would like to thank my colleagues from the Center for Astrophysics and Cosmology (from the University of Nova Gorica) and the Pierre Auger Collaboration for many fruitful discussions. I also thank the reviewers for their valuable comments on earlier versions of the manuscript, which helped to improve the paper. This work is supported by **coffee**.

Vielen Dank euch allen!

AppendixA. Difficult Stuff

AppendixB. More Difficult Stuff

AppendixB.1. Extreme Difficult Stuff

References

[1] I. Bartos, M. Kowalski, *Multimessenger Astronomy*, 2399-2891, IOP Publishing, 2017. doi:10.1088/978-0-7503-1369-8 URL http://dx.doi.org/10.1088/978-0-7503-1369-8

[2] M. Branchesi, *Multi-messenger astronomy: gravitational waves, neutrinos, photons, and cosmic rays*, Journal of Physics: Conference Series 718 (2) (2016) 022004. URL http://stacks.iop.org/1742-6596/718/i=2/a=022004

[3] P. Homola, for the Pierre Auger Collaboration, *Search for Ultra-High Energy Photons with the Pierre Auger Observatory*, ArXiv e-prints arXiv:1804.05613

[4] A. Aab, et al., *The Pierre Auger Observatory Upgrade - Preliminary Design Report* arXiv:1604.03637

[5] M. Nagano, *Search for the end of the energy spectrum of primary cosmic rays*, New Journal of Physics 11 (6) (2009) 065012. URL http://stacks.iop.org/1367-2630/11/i=6/a=065012

[6] Berat, Corinne, *The Pierre Auger Observatory status and latest results*, EPJ Web Conf. 136 (2017) 02017. doi:10.1051/epjconf/201713602017. URL https://doi.org/10.1051/epjconf/201713602017

[7] L. J. Watson, D. J. Mortlock, A. H. Jaffe, *A Bayesian analysis of the 27 highest energy cosmic rays detected by the Pierre Auger Observatory*, Mon. Not. Roy. Astron. Soc. 418 (2011) 206. arXiv:1010.0911, doi:10.1111/j.1365-2966.2011.19476.x.

[8] S. Liberati, *Quantum gravity phenomenology via Lorentz violations*, PoS P2GC (2007) 018. arXiv:0706.0142, doi:10.22323/1.034.0018.

[9] P. Homola, D. Gora, D. Heck, H. Klages, J. Pekala, M. Risse, B. Wilczynska, H. Wilczynski, *Simulation of ultrahigh energy photon propagation in the geomagnetic field*, Comput. Phys. Commun. 173 (2005) 71. arXiv:astro-ph/0311442, doi:10.1016/j.cpc.2005.07.001.

[10] M. G. Aartsen, et al., *Neutrino Interferometry for High-Precision Tests of Lorentz Symmetry with IceCube* arXiv:1709.03434

[11] S. R. Coleman, S. L. Glashow, *High-energy tests of Lorentz invariance*, Phys. Rev. D59 (1999) 116008. arXiv:hep-ph/9812418, doi:10.1103/PhysRevD.59.116008.

[12] A. MacFadyen, S. E. Woosley, *Collapsars: Gamma-ray bursts and explosions in 'failed supernovae'*, Astrophys. J. 524 (1999) 262. arXiv:astro-ph/9810274, doi:10.1086/307790.

[13] S. E. Woosley, J. S. Bloom, *The Supernova Gamma-Ray Burst Connection*, Ann. Rev. Astron. Astrophys. 44 (2006) 507–556. arXiv:astro-ph/0609142, doi:10.1146/annurev.astro.43.072103.150558.

[14] E. Waxman, J. N. Bahcall, *High-energy neutrinos from cosmological gamma-ray burst fireballs*, Phys. Rev. Lett. 78 (1997) 2292–2295. arXiv:astro-ph/9701231, doi:10.1103/PhysRevLett.78.2292.

[15] J. P. Rachen, P. Meszaros, *Photohadronic neutrinos from transients in astrophysical sources*, Phys. Rev. D58 (1998) 123005. arXiv:astro-ph/9802280, doi:10.1103/PhysRevD.58.123005.

[16] V. Berezinsky, M. Kachelriess, A. Vilenkin, *Ultrahigh-energy cosmic rays without GZK cutoff*, Phys. Rev. Lett. 79 (1997) 4302–4305. arXiv:astro-ph/9708217, doi:10.1103/PhysRevLett.79.4302.

[17] M. Birkel, S. Sarkar, *Extremely high-energy cosmic rays from relic particle decays*, Astropart. Phys. 9 (1998) 297–309. arXiv:hep-ph/9804285, doi:10.1016/S0927-6505(98)00028-0.

[18] V. A. Kuzmin, V. A. Rubakov, *Ultrahigh-energy cosmic rays: A Window to postinflationary reheating epoch of the universe?*, Phys. Atom. Nucl. 61 (1998) 1028. arXiv:astro-ph/9709187.

[19] P. Blasi, R. Dick, E. W. Kolb, *Ultra-high energy cosmic rays from annihilation of superheavy dark matter*, Astroparticle Physics 18 (1) (2002) 57 – 66. doi:https://doi.org/10.1016/S0927-6505(02)00113-5. URL http://www.sciencedirect.com/science/article/pii/S0927650502001135

[20] C. T. Hill, *Monopolonium*, Nuclear Physics B 224 (3) (1983) 469 – 490. doi:https://doi.org/10.1016/0550-3213(83)90386-3. URL http://www.sciencedirect.com/science/article/pii/0550321383903863

[21] P. Goddard, P. Mansfield, *Topological structures in field theories*, Reports on Progress in Physics 49 (7) (1986) 725. URL http://stacks.iop.org/0034-4885/49/i=7/a=001

[22] T. Weiler, *Resonant Absorption of Cosmic-Ray Neutrinos by the Relic-Neutrino Background*, Phys. Rev. Lett. 49 (1982) 234–237. doi:10.1103/PhysRevLett.49.234. URL https://link.aps.org/doi/10.1103/PhysRevLett.49.234

[23] T. J. Weiler, *Cosmic ray neutrino annihilation on relic neutrinos revisited: A Mechanism for generating air showers above the Greisen-Zatsepin-Kuzmin cutoff*, Astropart. Phys. 11 (1999) 303–316. arXiv:hep-ph/9710431, doi:10.1016/S0927-6505(98)00068-1.

[24] D. Fargion, B. Mele, A. Salis, *Ultra-High-Energy Neutrino Scattering onto Relic Light Neutrinos in the Galactic Halo as a Possible Source of the Highest Energy Extragalactic Cosmic Rays*, The Astrophysical Journal 517 (2) (1999) 725. URL http://stacks.iop.org/0004-637X/517/i=2/a=725

[25] J. Ellis, V. E. Mayes, D. V. Nanopoulos, *Ultrahigh-energy cosmic rays particle spectra from crypton decays*, Phys. Rev. D 74 (2006) 115003. doi:10.1103/PhysRevD.74.115003. URL https://link.aps.org/doi/10.1103/PhysRevD.74.115003

[26] Z. Fodor, S. D. Katz, *Grand unification signal from ultrahigh-energy cosmic rays?*, Phys. Rev. Lett. 86 (2001) 3224–3227. arXiv:hep-ph/0008204, doi:10.1103/PhysRevLett.86.3224.

[27] S. Sarkar, R. Toldr, *The high energy cosmic ray spectrum from relic particle decay*, Nuclear Physics B 621 (1) (2002) 495 – 520. doi:https://doi.org/10.1016/S0550-3213(01)00565-X URL http://www.sciencedirect.com/science/article/pii/S055032130100565X

[28] C. Barbot, M. Drees, *Detailed analysis of the decay spectrum of a super heavy X particle*, Astropart. Phys. 20 (2003) 5–44. arXiv:hep-ph/0211406, doi:10.1016/S0927-6505(03)00134-8.

[29] R. Aloisio, V. Berezinsky, M. Kachelriess, *Fragmentation functions in supersymmetric QCD and ultrahigh energy cosmic ray spectra produced in top-down models*, Phys. Rev. D 69 (2004) 094023. doi:10.1103/PhysRevD.69.094023. URL https://link.aps.org/doi/10.1103/PhysRevD.69.094023

[30] S. Sarkar, *New physics from ultrahigh-energy cosmic rays*, Acta Phys. Polon. B35 (2004) 351–364. arXiv:hep-ph/0312223.

[31] S. Lee, A. V. Olinto, G. Sigl, *Extragalactic Magnetic Field and the Highest Energy Cosmic Rays*, The Astrophysical Journal Letters 455 (1) (1995) L21. URL http://stacks.iop.org/1538-4357/455/i=1/a=L21

[32] M. Risse, P. Homola, R. Engel, D. Góra, D. Heck, J. Pekala, B. Wilczyńska, H. Wilczyński, *Photon air showers at ultra-high energy and the photonuclear cross-section*, Czechoslovak Journal of Physics 56 (1) (2006) A327–A336. doi:10.1007/s10582-006-0166-7. URL https://doi.org/10.1007/s10582-006-0166-7

[33] E. Gabrielli, K. Huitu, S. Roy, *Photon propagation in magnetic and electric fields with scalar/pseudoscalar couplings: A New look*, Phys. Rev. D74 (2006) 073002. arXiv:hep-ph/0604143, doi:10.1103/PhysRevD.74.073002.

[34] M. Fairbairn, T. Rashba, S. Troitsky, *Photon-axion mixing and ultra-high energy cosmic rays from BL Lac type objects: Shining light through the Universe*, Phys. Rev. D 84 (2011) 125019. doi:10.1103/PhysRevD.84.125019. URL https://link.aps.org/doi/10.1103/PhysRevD.84.125019

[35] G. B. Gelmini, O. E. Kalashev, D. V. Semikoz, *GZK Photons Above 10-EeV*, JCAP 0711 (2007) 002. arXiv:0706.2181, doi:10.1088/1475-7516/2007/11/002.

[36] P. Bhattacharjee, G. Sigl, *Origin and propagation of extremely high-energy cosmic rays*, Phys. Rept. 327 (2000) 109–247. arXiv:astro-ph/9811011, doi:10.1016/S0370-1573(99)00101-5.

[37] S. Sikora, Ł. Bratek, J. Jałocha, M. Kutschera, *Motion of halo tracer objects in the gravitational potential of a low- mass model of the Galaxy*, AAP 579 (2015) A134. doi:10.1051/0004-6361/201526189.

[38] L. Maccione, S. Liberati, *GZK photon constraints on Planck scale Lorentz violation in QED*, JCAP 0808 (2008) 027. arXiv:0805.2548, doi:10.1088/1475-7516/2008/08/027.

[39] J. Ellis, N. E. Mavromatos, D. V. Nanopoulos, *Space-time foam effects on particle interactions and the Greisen-Zatsepin-Kuzmin cutoff*, Phys. Rev. D 63 (2001) 124025. doi:10.1103/PhysRevD.63.124025. URL https://link.aps.org/doi/10.1103/PhysRevD.63.124025

[40] A. Almheiri, D. Marolf, J. Polchinski, J. Sully, *Black Holes: Complementarity or Firewalls?*, JHEP 02 (2013) 062. arXiv:1207.3123, doi:10.1007/JHEP02(2013)062.

[41] [link]. URL https://credo.science/

[42] F. Tavecchio, M. Roncadelli, G. Galanti, *Photons to axion-like particles conversion in Active Galactic Nuclei*, Physics Letters B 744 (2015) 375 – 379. doi:https://doi.org/10.1016/j.physletb.2015.04.017.
URL http://www.sciencedirect.com/science/article/pii/S0370269315002609

[43] C. Wang, D. Lai, *Axion-photon Propagation in Magnetized Universe*, JCAP 1606 (06) (2016) 006. arXiv:1511.03380, doi:10.1088/1475-7516/2016/06/006.

[44] [link]. URL http://www.amon.psu.edu/

[45] J. Abadie, et al., *Implications For The Origin Of GRB 051103 From LIGO Observations*, Astrophys. J. 755 (2012) 2. arXiv:1201.4413, doi:10.1088/0004-637X/755/1/2.

[46] M. W. E. Smith, et al., *The Astrophysical Multimessenger Observatory Network (AMON)*, Astropart. Phys. 45 (2013) 56–70. arXiv:1211.5602, doi:10.1016/j.astropartphys.2013.03.003.

[47] M. Risse, P. Homola, *Search for ultrahigh energy photons using air showers*, Mod. Phys. Lett. A22 (2007) 749–766. arXiv:astro-ph/0702632, doi:10.1142/S0217732307022864.

[48] J. Abraham, et al., *An upper limit to the photon fraction in cosmic rays above 10^{19}-eV from the Pierre Auger Observatory*, Astropart. Phys. 27 (2007) 155–168. arXiv:astro-ph/0606619, doi:10.1016/j.astropartphys.2006.10.004.

[49] Pierre Auger Collaboration, J. Abraham, P. Abreu, M. Aglietta, C. Aguirre, E. J. Ahn, D. Allard, I. Allekotte, J. Allen, P. Allison, et al., *Upper limit on the cosmic-ray photon fraction at EeV energies from the Pierre Auger Observatory*, Astroparticle Physics 31 (2009) 399–406. arXiv:0903.1127, doi:10.1016/j.astropartphys.2009.04.003.

[50] J. Abraham, et al., *Upper limit on the cosmic-ray photon flux above 10^{19} eV using the surface detector of the Pierre Auger Observatory*, Astropart. Phys. 29 (2008) 243–256. arXiv:0712.1147, doi:10.1016/j.astropartphys.2008.01.003.

[51] P. Abreu, et al., *The Pierre Auger Observatory III: Other Astrophysical Observations*, in: Proceedings, 32nd International Cosmic Ray Conference (ICRC 2011): Beijing, China, August 11-18, 2011, 2011. arXiv:1107.4805.
URL https://inspirehep.net/record/919729/files/arXiv:1107.4805.pdf

[52] A. Aab, P. Abreu, M. Aglietta, M. Ahlers, E. J. Ahn, I. Al Samarai, I. Albuquerque, I. Allekotte, J. Allen, P. Allison, A. Almela, J. Alvarez Castillo, J. Alvarez-Muiz, R. Alves Batista, M. Ambrosio, A. Aminaei, L. Anchordoqui, S. Andringa, C. Aramo, M. Ziolkowski, *PROBING THE RADIO EMISSION FROM COSMIC-RAY-INDUCED AIR SHOWERS BY POLARIZATION MEASUREMENTS*.

[53] L. D. Landau, I. Pomeranchuk, *Electron cascade process at very high-energies*, Dokl. Akad. Nauk Ser. Fiz. 92 (1953) 735–738.

[54] L. D. Landau, I. Pomeranchuk, *Limits of applicability of the theory of bremsstrahlung electrons and pair production at high-energies*, Dokl. Akad. Nauk Ser. Fiz. 92 (1953) 535–536.

[55] A. B. Migdal, *Bremsstrahlung and pair production in condensed media at high-energies*, Phys. Rev. 103 (1956) 1811–1820. doi:10.1103/PhysRev.103.1811.

[56] D. Heck, J. Knapp, J. N. Capdevielle, G. Schatz, T. Thouw, *CORSIKA: a Monte Carlo code to simulate extensive air showers.*, 1998.

[57] A. Aab, et al., *The Pierre Auger Cosmic Ray Observatory*, Nucl. Instrum. Meth. A798 (2015) 172–213. arXiv:1502.01323, doi:10.1016/j.nima.2015.06.058.

[58] A. Neronov, D. V. Semikoz, I. Vovk, R. Mirzoyan, *Cosmic-ray composition measurements and cosmic ray background-free γ-ray observations with Cherenkov telescopes*, Phys. Rev. D94 (12) (2016) 123018. arXiv:1610.01794, doi:10.1103/PhysRevD.94.123018.

[59] K. Almeida Cheminant, et al., *Search for electromagnetic superpreshowers using gamma-ray telescopes*, PoS ICRC2017 (2017) 860. arXiv:1709.05180.

[60] N. Dhital, P. Homola, J. F. Jarvis, P. Poznanski, K. Almeida Cheminant, Ł. Bratek, T. Bretz, D. Gora, P. Jagoda, J. Jałocha, K. Kopanski, D. Lemanski, M. Magrys, V. Nazari, J. Niedzwiedzki, M. Nocun, W. Noga, A. Ozieblo, K. Smelcerz, K. Smolek, J. Stasielak, S. Stuglik, M. Sułek, O. Sushchov, J. Zamora-Saa, *We are all the Cosmic-Ray Extremely Distributed Observatory*, ArXiv e-prints arXiv:1709.05196.

[61] [link]. URL http://ipnwww.in2p3.fr/~augers/AugerProtected/herald.php

[62] M. Niechciol, M. Risse, P. Ruehl, M. Settimo, P. W. Younk, A. Yushkov, *F: A new observable for photon-hadron discrimination in hybrid air shower events*, Astroparticle Physics 97 (2018) 88–95. arXiv:1710.06586, doi:10.1016/j.astropartphys.2017.10.004.

[63] Pierre Auger Collaboration, P. Abreu, M. Aglietta, E. J. Ahn, I. F. M. Albuquerque, D. Allard, I. Allekotte, J. Allen, P. Allison, J. Alvarez Castillo, et al., *Anisotropy and chemical composition of ultra-high energy cosmic rays using arrival directions measured by the Pierre Auger Observatory*, JCAP 6 (2011) 022. arXiv:1106.3048, doi:10.1088/1475-7516/2011/06/022.

Developing a real time photon search for The Astrophysical Multimessenger Observatory Network with the Pierre Auger Observatory

Lukas Zehrer*

Center for Astrophysics and Cosmology, University of Nova Gorica, Vipavska, 11c, 5270, Ajdovscina, Slovenia

Abstract

With the recent discovery of gravitational waves and high-energy cosmic neutrinos, we are witnessing the beginning of a new era in multimessenger astronomy. The exploration of the Universe through these new messengers, along with electromagnetic radiation and cosmic rays, gives us new insights into the most extreme energetic cosmic events, environments and particle accelerators. The large collection area of the Pierre Auger Observatory (PAO) and the availability of a variety of composition-sensitive parameters provide an excellent opportunity to search for photons in the cosmic ray flux above 10^{18} eV. Upper limits published previously, using data from the Observatory, placed severe constraints on top-down models. Now, the increase in exposure by more than a factor 2 since 2008 together with the combination of different observables means that the detection of GZK-photons predicted using bottom-up models is almost within reach. In this paper the status of these investigations and perspectives for further studies are summarized. Current results on triggering variables for photons from the PAO for The Astrophysical Multimessenger Observatory Network (AMON) are presented and their implications will be discussed.

Keywords: GZK effect, showers: air, photon: showers, showers: energy, cosmic rays, air showers, Ultra High Energy Photons, Pierre Auger Observatory, PAO, Trigger, New Triggers, MoPS and ToTd, data analysis, real time photon search, Astrophysical Multimessenger Observatory Network, AMON

1. Introduction

Multi-messenger astrophysics is a quest to use the messenger particles of all four of natures fundamental forces to explore the most energetic phenomena in the universe based on the coordinated observation and interpretation of disparate "messenger" signals. The four extrasolar messengers are electromagnetic (EM) radiation, gravitational waves, neutrinos, and cosmic rays (CRs). They are created by different astrophysical processes, and thus reveal different information about their sources. Just one example these facilities collectively promise is the resolution of the mystery surrounding the origins of ultra high energy cosmic rays (UHECR).

The main multi-messenger sources outside the heliosphere are expected to be compact binary pairs (black holes (BH) and neutron stars (NS)), supernovae, irregular neutron stars (INS), gamma-ray bursts (GRB), active galactic nuclei (AGN), and relativistic jets [1, 2].

In order to interpret cosmic ray observations, detailed modelling of propagation effects invoking all important messengers is necessary. There is a correlation between acceleration sites of UHE cosmic rays and the emission of high-energy photons and neutrinos. The observation and interpretation of these particles in different energy regimes in a so-called multi-messenger approach allows for maximizing the scientific information and will increase the chances of identifying the sources of UHE cosmic rays.

In addition to the nuclear component of the UHE Cosmic Rays, a substantial photon flux, with fractions up to 50% at the highest energies, is expected according to the predictions of the non-acceleration models. Fractions at the level of 0.1% expected from the decay of neutral pions produced in the interaction of nucleons with the cosmic microwave background (GZK effect). Discrimination between the different scenarios for the origin of the UHECR is possible, based on observables sensitive to the distinctive characteristics of extensive atmospheric showers (EAS). Deviation of data from expectations for showers induced by nuclear primaries can offer a clear signature for photons, detectable by fluorescence telescopes as well as by arrays of surface detectors.

The detection of primary photons at these extreme energies will open a new window to the Universe, with large impact also on fundamental physics. So far no observation of UHE photons has been claimed, but stringent limits on their fraction in the integral CR flux have been placed [3, 4]. These limits help to reduce uncertainties related to photon contamination in other air shower mea-

*Corresponding author
Email address: lukas.zehrer@ung.si (Lukas Zehrer)
URL: http://www.ung.si/en/research/cac/staff/ (Lukas Zehrer)

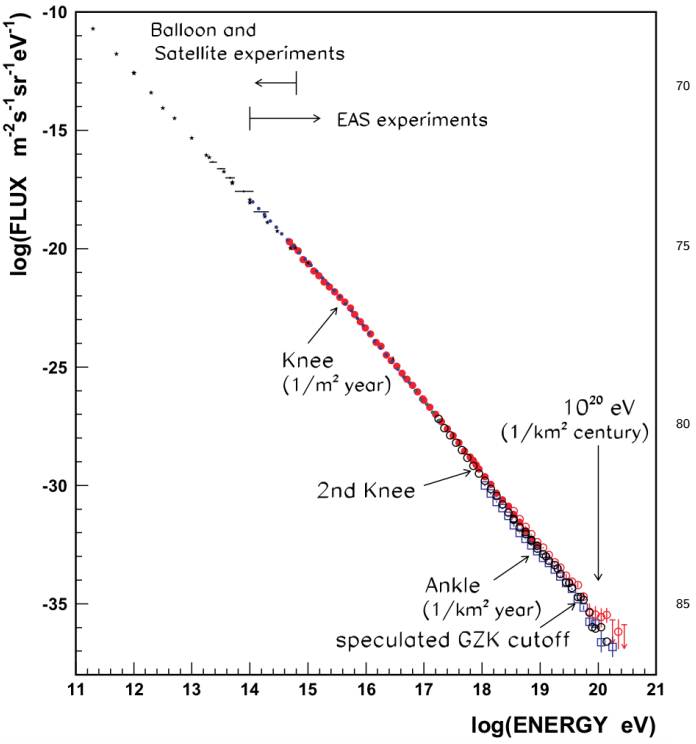

Figure 1: Energy spectrum of primary cosmic rays. Results from Akeno-AGASA, which cover the energy range (10^{15}-10^{20} eV), are shown by red closed and open circles. Direct observations with balloon- and satellite-borne detectors are plotted as dots below the knee, around 10^{15} eV. Tibet results, which cover the energy region below and above the knee, are plotted as blue circles. In the high- est energy region, results from HiRes and Auger are shown as open black circles and open blue squares, respectively. The overall spectrum is expressed by a power law from 10^{11} to 10^{20} eV with only small changes of slope around $10^{15.5}$ eV (the knee), $10^{17.8}$ eV (the second knee) and 10^{19} eV (the ankle). Figure taken from [5].

surements like the determination of the primary composition and of energy spectrum and the derivation of the proton-air inelastic cross-section.

The paper is structured as follows: In Section 2 I start with providing an introduction on observations in sec. 2.1 and 2.2. In 2.3 possible origins of cosmic rays are discussed. Section 2.4 explains the connection between cosmic rays and photons and what we can explore with them. In sec. 3 and 4 an short introduction to AMON and the PAO respectively is given. Section 5 presents a discussion of my work so far and an outlook of the work to be done, before sec 6 presents my summary and conclusions.

2. Ultra High Energy Photons

2.1. The energy spectrum of cosmic rays

The CR spectrum extends over many orders of magnitude, reaching energies above 10^{20} eV, this is millions of times greater than the energies achieved in the most powerful accelerators on Earth (see fig. 1).

Ultra high energy cosmic rays denotes a cosmic ray particle with kinetic energy $> 10^{18}$ eV and extreme energy cosmic ray (EECR) is a UHECR with energy exceeding $5{\cdot}10^{19}$ eV (about 8 joule), the so-called *GZK limit*. Experimental work is being done, gathering information about particles arriving at Earth, and also theoretical work regarding models of possible sources. In the high energy region of fig. 1 there are two important characteristics observed:

- The *ankle*, which could represent the transition from a galactic power-law behaviour (power-law energy flux of $J \propto E^{-\gamma}$) to an extragalactic contribution, or it could be a "dip" due to $e^{\pm}$ pair production in a cosmic-ray spectrum that is dominated by protons of extragalactic origin.
- A *cut-off* at $\approx 4{\cdot}10^{19}$ eV, which is found with more than 20σ significance and could be related to the GZK effect or to the maximum energy reached by the acceleration sources ("bottom-up" models).

The spectrum (fig. 1) flattens from a power law with index (3.29 ± 0.02(stat) $\pm$ 0.05(sys)) to one with index (2.60 ± 0.02(stat) $\pm$ 0.1(sys)) at $E_{ankle} = 4.8 \pm 0.1 \pm 0.8$ EeV. A clear suppression is observed at a significance in excess of 20σ beyond $E_s = 42.1 \pm 1.7 \pm 7.6$ EeV, the energy at which the differential flux is reduced to one-half of that expected from the extrapolation of the power law above the ankle. [6]

2.2. The GZK limit

The Greisen-Zatsepin-Kuzmin limit (GZK limit) is a theoretical upper limit on the energy of cosmic ray protons travelling from other galaxies through the intergalactic medium to our galaxy. The limit is $5 \cdot 10^{19}$ eV (or about 8 joules). The limit is set by slowing-interactions of the protons with the microwave background radiation over long distances ($\approx$ 160 million light-years). The limit is at the same order of magnitude as the upper limit for energy at which cosmic rays have experimentally been detected. The GZK limit is derived under the assumption that UHECRs are protons.

It is computed based on interactions between cosmic rays and the photons of the cosmic microwave background radiation (CMB). Predicted that cosmic rays with energies over the threshold energy of $5 \cdot 10^{19}$ eV would interact with CMB photons (γ_{CMB}), relatively blueshifted by the speed of the cosmic rays, to produce pions via the Δ-resonance,

$$\gamma_{CMB} + p \rightarrow \Delta^+ \rightarrow p + \pi^0 \ , \qquad (1)$$

or

$$\gamma_{CMB} + p \rightarrow \Delta^+ \rightarrow n + \pi^+ \ . \qquad (2)$$

Pions produced in this manner proceed to decay in the standard pion channels - ultimately to photons for neutral pions, and photons, positrons, and various neutrinos for

positive pions. Neutrons decay also to similar products, so that ultimately the energy of any cosmic ray proton is drained off by production of high energy photons plus (in some cases) high energy electron/positron pairs and neutrino pairs.

The pion production process continues until the cosmic ray energy falls below the pion production threshold. *Due to the mean path associated with this interaction, extragalactic cosmic rays travelling over distances larger than 50 Mpc (163 Mly) and with energies greater than this threshold should never be observed on Earth. This distance is also known as GZK horizon.*

The GZK limit should be the maximum energy of a cosmic ray protons, since higher-energy protons would have lost energy over that distance due to scattering from photons in the cosmic microwave background (CMB). It follows that EECR could not be survivors from the early universe, but are cosmologically "**young**", emitted somewhere in the Local Supercluster by some unknown physical process.

Measurements by the largest cosmic-ray observatory, the Pierre Auger Observatory (see sec. 4), suggest that most UHECRs are heavier elements. In this case, the argument behind the GZK limit does not apply in the originally simple form and there is no fundamental contradiction in observing cosmic rays with energies that violate the limit.

If an EECR is not a proton, but a nucleus with A nucleons, then the GZK limit applies to its nucleons, which carry only a fraction 1/A of the total energy of the nucleus. For an iron nucleus, the corresponding limit would be $2.8 \cdot 10^{21}$ eV. These particles are extremely rare; between 2004 and 2007, the initial runs of the Pierre Auger Observatory (PAO) detected 27 events with estimated arrival energies above $5.7 \cdot 10^{19}$ eV, i.e., about one such event every four weeks in the 3000 km^2 area surveyed by the observatory.

Given the small numbers of UHECRs on which the PAO results are based, some care must be taken with statistical methods, both to ensure that all the available information is utilised and to avoid over-interpretation. These aims are achieved by adopting a Bayesian approach in which the relevant stochastic processes (e.g. the GZK interactions of the UHECRs with the CMB, deflection by the Galaxys magnetic field, measurement errors) are explicitly modelled.

Even though the details of some of these processes are not well known (most relevantly the strength of the magnetic fields and the energy calibration of the UHECRs), such uncertainties are accounted for by marginalisation.

There is evidence that these highest-energy cosmic rays might be iron nuclei, rather than the protons that make up most cosmic rays. [7]

In the past, the apparent violation of the GZK limit has inspired cosmologists and theoretical physicists to suggest other ways that circumvent the limit. These theories propose that ultra-high energy cosmic rays are *produced nearby our galaxy* or that *Lorentz covariance is violated* in such a way that protons do not lose energy on their way to our galaxy.

These observations appear to contradict the predictions of special relativity and particle physics as they are presently understood. However, there are a number of possible explanations for these observations that may resolve this inconsistency.

- The observations could be due to an instrument error or an incorrect interpretation of the experiment, especially wrong energy assignment.
- The cosmic rays could have local sources well within the GZK horizon (although it is unclear what these sources could be).
- Cosmic rays are mostly heavier nuclei with A nucleons. This pushes the effective GZK limit for the whole nucleus up (factor A). For iron nuclei (the heaviest abundant element in cosmic rays) the corresponding energy limit is well beyond the energies of detected ultra-high-energy cosmic rays.

Several theoretical models present explanation of the non-observation of UHE photons possibly produced as a consequence of aforementioned scenarios. For example, in Lorentz Invariance Violation (LIV) scenarios based on the concept of photon decay (see Ref. [8] for a review on various concepts) the lifetime of a UHE photon would be extremely short ($\ll 1$ s), which would dramatically reduce its chances of reaching the Earth. On the other hand, one might approach observing the result of a UHE photon decay, an extensive cascade composed mainly of photons below the decay threshold. These cascades can be considered in a general way, regardless of the primary process, and call them cosmic-ray cascades (CRC) or *superpreshowers* (SPS, more see sec. 2.4.1) (per analogiam to the preshower effect of a UHE photon with the geomagnetic field - see e.g. Ref. [9] and references therein).

Several approaches to quantum gravity predict LIV at high energies (e.g. Horava-Lifshitz [10]). (Lorentz violations are allowed in string theory, supersymmetry and Horava-Lifshitz gravity.)

- If Lorentz-invariance is broken, the reaction threshold may be upshifted (and Universe becomes transparent for UHE photons) $\Rightarrow$ no observed cut-off [11]

2.3. Origin of cosmic rays

There are two different approaches that try to describe the origin of these UHECRs, namely due to particle acceleration, called "**bottom-up**" model and exotic models, called "**top-down**" model.

2.3.1. Particle acceleration - "*bottom-up*"

Here the four most prominent mechanisms are mentioned in short. The first is the *fermi acceleration* on shock waves, where the energy depends on the sources size, its magnetic field and the particle charge. The second source for UHECRs could be *supernova remnants*, which maximum energy attainable is limited ($\lesssim 10^{15}$ eV). Higher energies can be reached in larger objects or in stronger magnetic fields, with examples for this third solution: *active galactic nuclei* (AGN, also see sec. 2.4.2), or *colliding galaxies*. The high magnetic fields and strong astrophysical shocks observed in some of these objects are expected to be responsible for the acceleration of cosmic rays up to the highest observable energies. But its not certain if the particles with the highest observed energies can be produced there. And fourth the before mentioned GZK effect (interaction with microwave background photons) which limits the range of particles with the highest energies.

Gamma-ray bursts (GRBs) are just a small fraction of UHECR and would (probably) not contribute to the ultra high energy photons, because they come from far away, isotropically in the universe and loose most of the energy on its way.

Just to mention in short one of the models of GRBs that may contribute to *UHE photons* are the traditional or "classical" long-duration, high-luminosity gamma-ray bursts (HL-GRBs). They are the most common type of GRB detected by satellite experiments, being observed as bright seconds- to minutes-long bursts of γ-radiation from high-redshift (z=1). HL-GRBs are believed to arise when a massive star ($M \approx M_{\odot}$) undergoes a core collapse to a black hole (BH); confirmation of this "collapsar" model [12] for the HL-GRBs has been most dramatically provided by spectroscopic observations of ensuing type Ibc super-novae (SNe), with other lines of evidence also contributing [13].

2.3.2. Exotic models - "*top-down*"

Particles with the highest observed energies may not be the result of acceleration, but rather a product of interactions or decays of particles yet to be discovered directly.

Some of the proposed scenarios of cosmic ray production are *superheavy dark matter* (SHDM, [16–19]) - possibly concentrated near galaxies/clusters, which are metastable particles that could decay or annihilate, *relic topological defects* (TD; monopoles, cosmic strings or others [20, 21]) - which undergo decays and produce cascades of energetic particles, the before mentioned "*Z-Burst*" (ZB) model - in which highest energy neutrinos annihilate on background antineutrinos, producing Z bosons (Z-resonance) that decay into observed particles (producing secondary protons, neutrinos and photons) [22–24], and others [25–29].

All these models predict a large fraction of photons and neutrinos (tens of percent) in the cosmic rays of highest energies. And therefore ***UHE photons*** *would be a smoking gun for non-acceleration models!*

2.4. UHE Photons - γ_{UHE}

The search of UHE photons can help to solve these before-mentioned mysteries. The photon and the electron are observed fundamental particles and their interactions are well understood. Photons, as the gauge bosons of the EM force, at such enormous energy are unique messengers and probes of extreme and, possibly, new physics. Propagation features of UHE photons are sensitive to the MHz radio background [30]. The photon flux at Earth is also sensitive to extragalactic magnetic fields [31].

Already a small sample of photon-induced showers may provide relatively clean probes of aspects of quantum electrodynamics (QED) and quantum chromodynamics (QCD) at ultra-high energy via the preshower process and photonuclear interactions (see, e.g., [32]).

For sources more than a few tens of Mpc away the energy in the produced UHE-photon population may go into the development of a full electromagnetic cascade, with the energy flux arriving mainly at GeV-TeV energies, such sources either contributing to the diffuse gamma-ray background at these energies, or being individually resolvable in some scenarios, depending on the strength of the inter- or extragalactic magnetic fields. However, for a more nearby source, the electromagnetic cascades development has insufficient time to develop, with only the appreciable production of a first generation of UHE photons, leading to their contribution to the diffuse UHE photon background. *Thus, the search for UHE photons in the arriving UHECR flux can provide information about the* ***local*** *UHECR sources on these scales.*

Photon-induced showers are mostly electromagnetic with the first interaction dominated by electron-positron pair production in the Coulomb field. At the highest energies (above 10 EeV) two additional effects come into play: the Landau, Pomeranchuk and Migdal (LPM) effect and preshower in the geomagnetic field (for more see sec. 2.4.1).

It is interesting to check whether UHE photon propagation could be affected by the presence of axions or scalar bosons. The formal requirements for photon-axion conversion regarding photon energy and magnetic field strength, appear to be fulfilled [33]. Photon conversions to non-electromagnetic channels may differ from the standard QED process due to an absence of electromagnetic sub-cascade. Photon-axion conversion may ultimately increase the propagation distance of the UHE photons thus allowing to identify distant sources [34].

Above the GeV energy range, photons cannot conceivably be generated by thermal emission from hot celestial objects. Instead, UHE photons probe the non-thermal Universe where other mechanisms allow the concentration of large amounts of energy into a single particle. Typically, the production is associated with the decay of a neutral pion previously produced by a primary process (compare eq. (1)). UHE photons are mainly produced as either secondaries of the photo-pion production (GZK effect) of nuclei with a photon fraction at Earth of $\approx$ 0.1-1%

[35], or are a product in top-down models with a photon fraction at Earth of $\gtrsim 10\%$ (up to c.a. 50%) [36]. The main production process at UHE are photo-pion interactions where a nucleon N interacts with a background photon γ producing charged and neutral pions (see eq. (1) and (2)) in a GZK-type process. In the channel that conserves the charge of the original nucleon mostly neutral pions are produced which decay into secondary gamma rays

$$\pi^0 \quad \rightarrow \quad \gamma + \gamma \quad . \tag{3}$$

UHECR protons undergo these photo-pion interaction with background radiation fields (predominantly the CMB) producing both neutral and charged pions and hence a secondary UHE photon and neutrino flux around the source region. With the propagation of these UHE photons in turn being limited through $\gamma\gamma$ interactions with background photons, a region of space should exist around the source in which this UHE-photon flux is maximal. Due to the $\gamma\gamma$ cross-section and the dominant photon background targeting to these photons, the cosmic radio background (CRB) the interaction lengths for this process, above threshold, are a few Mpc. Thus, the distance for which the generated UHE photon flux is maximum would lie between a few Mpc and a few tens of Mpc from the source. It shall be noted here that though the CMB presents a much larger photon background target in terms of number density, the interaction of UHE photons (and UHE electrons) with it is suppressed due to the Klein Nishina suppression in the cross section for center-of-mass energies.

Depending on the energy of interest, other production mechanisms may become important, such as photons from photo-disintegration, elastic scattering, pair-production processes, radiative decay or synchrotron emission. The highest energies in the universe are only indirect accessible, e.g. via extensive air showers.

2.4.1. *Super-preshowers*

The complexity of the UHECR puzzle indirectly supports an alternative scenario that could be capable of generating UHE particles without an absolute need for correlation with the sources. While gravitational properties of SHDM particles are rather unquestioned, the distribution of SHDM particles seems to be disputable, e.g. not every galaxy can be an SHDM source. It is for instance not clear in the case of our Galaxy [37]. If SHDM distribution is not too far from uniform on a scale of super galaxy cluster, or if the propagation horizon of UHE photons is more limited than we extrapolate, we might not see SHDM sources. On the other hand, conclusions about the constraints on the sources or processes leading to the production of UHE photons require a number of fundamental assumptions concerning the electrodynamics at the grand unified theory (GUT) energies [38], hadronic properties of UHE photons, or space-time structure [39]. Also, modelling the propagation of UHE photons through the intergalactic, interstellar and even inter-

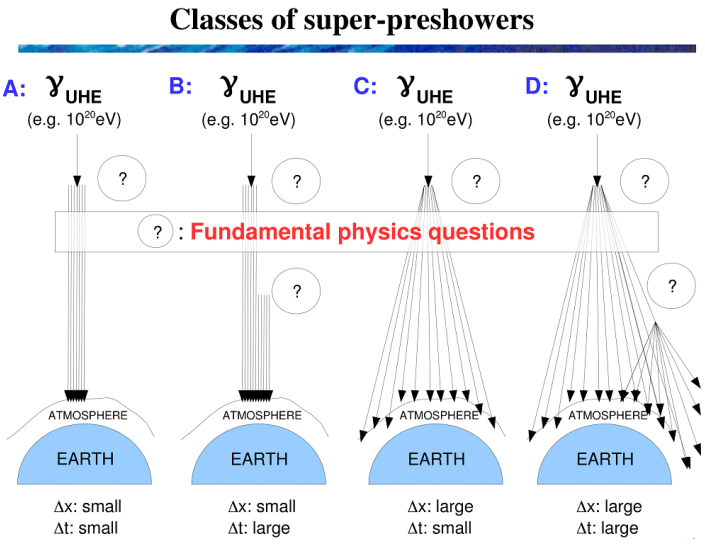

Figure 2: A basic observational classification of super-preshowers. Different classes refer to different widths of spatial and temporal distributions of super-preshower particles. The question marks represent the uncertainties about the fundamental physisc processes at E=10^{20} eV or larger. Figure taken from [41].

planetary medium requires assumptions difficult to verify. In addition uncertainty about the physics processes at GUT energies, i.e. expectations of deviations from the Standard Models in cosmology and particle physics because of the apparent difficulties in reconcilement between theories of General Relativity and Quantum Field Theory (see e.g. Ref. [40]). Therefore, any conclusions where the GUT uncertainties are involved, in particular the conclusions based on the *upper limits to UHE photons*, are disputable. Physical mechanisms which lead to a cascading of most of the UHE photons before they reach the Earth and consequently shrink their astrophysical horizon are illustrated in Fig. 2. Given the occurrence of such mechanisms or processes in reality, UHE photons have little chance to reach the Earth, and what can be observed on the Earth is the resulting particles most likely in a form of large electromagnetic cascades. One example of such a cascading process is the preshower effect [9] which is due to an interaction of a UHE photon and secondary electrons with the geomagnetic field. Although this does not produce an extended cascade, a generalized notion to the same phenomena to a UHE photon travelling towards the Earth through close distance of the Sun can produce an extended cascade at the Earth. Particles (mainly photons and a few electrons/positrons) in a cascade initiated due to preshower effect in the geomagnetic field have very narrow spatial and temporal extents and fall under class "A". For same effect occurring at the vicinity of the Sun, one would expect particles with narrow time distribution but large spatial extent as the cascade arrives at the top of the Earths atmosphere (class C). Also, other less known scenarios might cause distribution of arrival times of the particles quite extended with narrow spatial distribution

(class B), or both distributions are extended (class D).

2.4.2. UHE Photons from AGN

First-order Fermi acceleration in collisionless shocks is supposed to operate in the central regions of active galactic nuclei (AGNs). Most of the shock energy is channeled into relativistic protons. Protons are effectively "cooled" as a result of interactions with the soft radiation produced by accreting matter. Among final products of such collisions are UHE photons.

3. AMON

The Astrophysical Multimessenger Observatory Network (AMON) [44] provides a framework for correlating high energy astrophysical signals across all possible astronomical messengers: photons, neutrinos, cosmic rays, and gravitational waves.

The primary goals of the program are: (1) To allow participating observatories to share their data with one another with strict anonymity, confidentiality and in accordance with their blind analysis procedures, (2) to enhance the combined sensitivity of participating observatories to astrophysical transients by enabling them to search for coincidences in their sub-threshold archival data and then in their sub-threshold real-time data and (3) to enable follow-up imaging of possible astrophysical sources with minimal latency.

In addition, AMON stores events from participating observatories into its database to perform archival searches for significant coincidences. AMON also receives events and broadcasts them immediately to the astronomical community for follow-up.

AMON will weave together existing and forthcoming high-energy astrophysical observatories into a single virtual system, capable of sifting through the various data streams in near real-time, identifying candidate and high-significance multimessenger transient events, and providing alerts to interested observers. AMON represents a natural next step in the extension of the global astronomical communitys vision beyond the EM spectrum.

Detection from one messenger and non-detection from a different messenger can also be informative [45]. AMON is structured as an open and extensible network, with an Memorandum of Understanding (MOU) that allows straightforward incorporation of new triggering and follow-up facilities.

Participants in AMON can be characterized as either "*triggering*", "*follow-up*" or both. Triggering participants are generally wide field-of-view observatories that feed a stream of sub-threshold events into the AMON framework. These events are processed to search for temporal and spatial correlations, leading to AMON-generated "alerts". Follow-up participants generally search for electromagnetic counterparts to the alerts with high-throughput, smaller field-of-view instruments.

The sensitivities of the non-electromagnetic observatories are naturally limited, with rates of detection for transient events of publishable significance known or expected to be low, approximately a handful up to a few dozen per year. [46]

During the intervals prior to and between detection of these rare high-significance events, the multimessenger facilities will be buffeted by signals from a far greater number of lower-significance events that will be statistically indistinguishable from background or noise processes. Such "*subthreshold*" events are, by definition, unrecoverable as astrophysical signals in the data stream of any individual facility. However, if they are accompanied by a subthreshold signal in another multimessenger channel they can be identified, and potentially achieve high significance, via careful coincidence analysis of the data streams from multiple facilities. [46]

In this paper I present the scientific case of a real time photon alert of the Pierre Auger Observatory (PAO) for AMON and describe its important elements.

4. Pierre Auger Observatory - Triggers

The Pierre Auger Observatory is the world's largest ultra-high energy cosmic ray detector, located at an altitude of about 1400 m above sea level near Malarge, in the province of Mendoza, Argentina. It provides an unprecedented sensitivity to search for photons at UHEs due to its vast collecting area, and also a large integrated aperture for the search of photons with energy above 100 PeV. The observatory is a *hybrid* detector, a combination of a large surface detector array (**SD**) and fluorescence detectors (**FD**). The SD consists of 1660 water Cherenkov particle detectors of a surface of 10 m^2 each, covering an area of 3000 km^2 on a grid with 1.5 km spacing (SD-1500), and a smaller area extension to a lower energy threshold with an infill grid with a detector spacing of 750 m (SD-750). The FD includes 27 individual fluorescence telescopes overlooking the SD array from four different sites. There are also other extensions of the observatory not mentioned here, that can be looked up for example in Ref. [4]. While the SD has a duty cycle of nearly 100%, the FD can only operate on dark clear nights resulting in a duty cycle of 10-15%. The hybrid design of the Pierre Auger Observatory has a great advantage of providing a variety of composition-sensitive parameters, which offer an excellent opportunity to search for photons in the cosmic ray flux at ultra high energies.

Delayed air showers. The assumption of delayed air shower development is, that at the highest energies the pair production formation length gets elongated so much that the destructive interference of the fields associated with the atoms and particles nearby the primary suppresses the pair production process in the upper atmosphere, thus delaying the first interaction and the consequent air shower

development. This is so-called *LPM effect* [53-55], a standard in air shower modelling [56].

It is important to note that the LPM suppression is sensitive to the possible LIV effects including both increase and reduction of the pair production formation length. While the former would strengthen the UHE photon discrimination power based on delayed air shower development, the latter would do the opposite: reduce or even invert the LPM effect, and hence make photon-induced air showers develop more similarly to those initiated by nuclei.

The present state-of the art photon identification methods involving the expectation of a delayed development of an air shower induced by a photon assume the standard LPM effect, without any LIV effects.

4.1. The role of a triggering observatory in AMON

From all the possibilities within the PAO in this paper two topics are dealt with: the first is the contribution to real-time photon search with the Auger data, the second is to develop photon triggers for AMON for multi-messenger studies.

From the Auger datasets of interest to AMON are not the UHE hadrons (because they are deflected by (poorly known) magnetic fields and have therefore a delayed arrival), but the UHE Galactic neutrons, UHE photons and UHE neutrinos.

4.2. UHE Photons withe the PAO

The PAO provides an unprecedented integrated aperture for the search of photons with energy above 100 PeV. There are recent results including the diffuse search for photons and the directional search for photon point sources. The derived limits are of considerable astrophysical interest: Diffuse limits place severe constraints on top-down models and start to touch the predicted GZK photon flux range while directional limits can exclude the continuation of the electromagnetic flux from measured TeV sources with a significance of more than 5σ and also prospects of neutral particle searches for the upcoming detector upgrade AugerPrime are highlighted in Ref. [3] and [4].

There are two ways to search for photons, with its properties used for photons identification:

1. Events observed by SD-alone:
   - Radius of curvature R and;
   - Risetime $t_{1/2}$ (at 1000 m from the shower core);
2. Search for photons with hybrid events
   - (Larger) X_{max} (FD) - what means that γ-induced showers reach maximum deeper in the atmosphere than nucleonic ones, see fig. 3;
   - Signal at a given distance is smaller (SD);
   - Fewer triggered stations (SD);

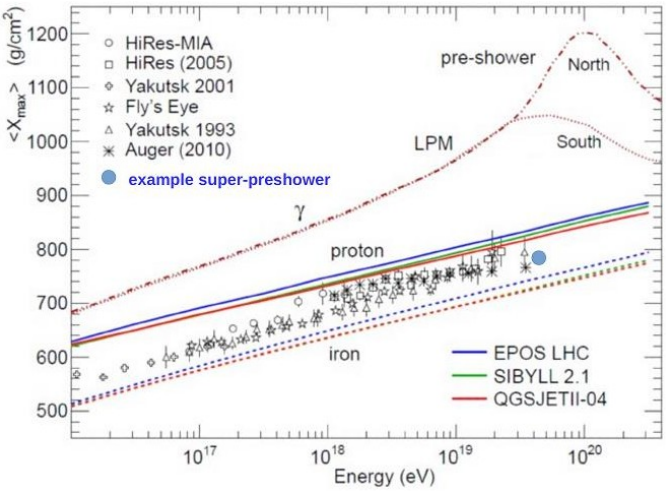

Figure 3: Variation of depth of air shower maximum with the primary energy: data collection and model predictions for different primaries. Figure taken from [41].

The two main discriminating observables, the radius of curvature of shower front and the time structure of shower front (risetime) are both correlated to X_{max}. A Larger X_{max} results in a larger curvature and therefore smaller radius. The reason for the risetime is due to the muonic component, since the μ are less delayed than e and γ. (The risetime is the time it takes the amplitude of the signal to go from 10% to 50%.)

The different variables can be combined to multivariate analysis observables. With UHE Photons (1-100 EeV), which have a loss length up to 30 Mpc (comp. fig. 4), there is the opportunity for AMON to identify nearby AGN flares, nearby sources of UHECRs (e.g. tidal disruptions, pulsars) and galactic sources. Another advantage of these UHE photon searches is the lower energy threshold than for neutrons. The AMON alerts with "photon"-like showers have a relaxed threshold compared to standard Auger searches.

The absence of point source photons does not mean that sources are extragalactic, they may be produced in transient sources (e.g. GRB or SN), may be emitted in jets not pointing to Earth, or may be EeV protons from sources with much lower optical depth (comp. to TeV sources).

4.2.1. Variables

Auger Triggers. The "new triggers" in Auger can be combined and used as a quick and rough discriminating observable. In June 2013, the Observatory installed across the entire array two additional SD T1 triggers [57]. These triggers build upon the ToT trigger in two ways, applying more sophisticated analysis to the event signal. The time-over-threshold-deconvolved (**ToTd**) trigger deconvolves the exponential tail of the diffusely reflected Cherenkov light pulses before applying the ToT condition. This has the effect of reducing the influence of muons in the trig-

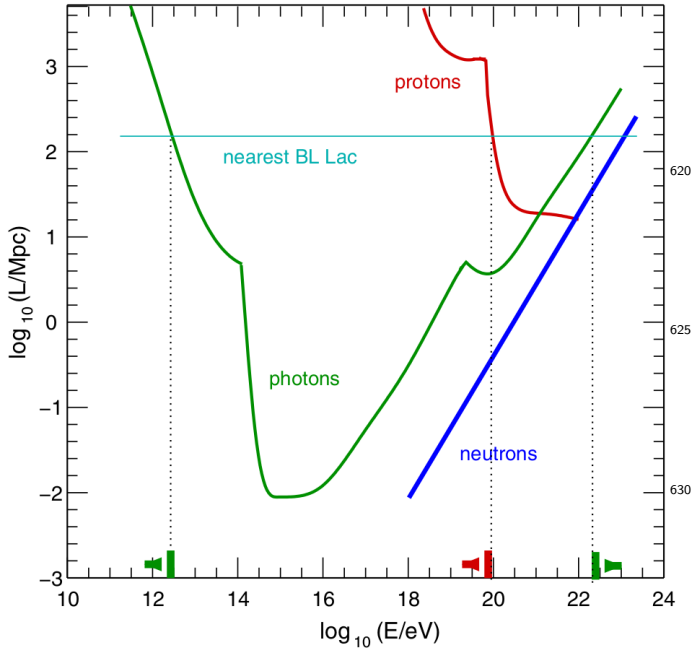

Figure 4: Attenuation length of different kinds of particles as compared to the distance to the nearest BL Lac (blue horizontal line) and the size of the Universe (upper bound of the plot). The green line corresponds to photons, blue to neutrons and red (shown for comparison) to protons. Figure taken from [34].

ger, since the typical signal from a muon, with fast rise time and ≈ 60 ns decay constant, is compressed into one or two time bins. The multiplicity-of-positive-steps trigger (**MoPS**), on the other hand, counts the number of positive-going signal steps in two of three photo-multiplier tubes (PMTs) within a 3 s sliding window. The steps are required to be above a small signal energy value (≈ 5·RMS noise) and below a moderate value (≈ 12 vertical muon step). This reduces the influence of muons in the trigger. Both the ToTd and MoPS triggers also require the integrated signal to be above ≈ 0.5 VEM. (The Cherenkov light recorded by a surface detector is measured in units of the signal produced by a muon traversing the tank on a central vertical trajectory. This unit is termed the Vertical Equivalent Muon (VEM). The goal of the surface detector calibration is to measure the value of 1 VEM in hardware units. During shower reconstruction, the signal recorded by the tanks is converted into units of VEM, and the total shower energy and arrival direction are fitted using a lateral distribution function and energy conversion based upon hybrid analysis using the FD measurements. The conversion to units of VEM is done both to provide a common reference level between tanks and to calibrate against the detector simulations.) Because these triggers minimize the influence of single muons, they reduce the energy threshold of the array, while keeping random triggers at an acceptable level. Thus they improve the energy reach of the SD, as well as improve the trigger efficiency for photon and neutrino showers. [4]

5. Data Analysis

The first steps in this work are to reproduce results (see fig. 5) from the earliest attempts in investigating and rough and quick discriminating variable to send an photon trigger from the PAO to AMON. This is done with data from Herald [61]. The CDAS (central data acquisition system) Herald is an automatic reconstruction running in the Lyon cluster. It uses the CDAS [4] reconstruction used to deliver the ICRC data set. The used herald distribution includes all data up to 31/5/2017. This version is corrected for weather and geomagnetic effects. Herald uses latest stable CDAS release to perform reconstructions for SD-1500 and SD-750 array. As is further described on the website, the ASCII format gives access to 48 shower reconstruction variables and quality. The website also lists a number of suggested cuts that should be applied.

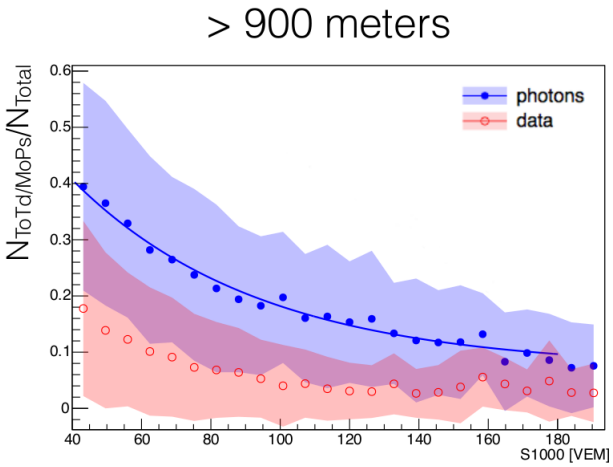

Figure 5: Preliminary results from previous working group obtained in 2015.

This rough and quick discriminating variable is the ratio of numbers of stations with new triggers to the number of all triggered stations plotted over another SD variable, S_{1000}.

5.1. Results and Discussion

In fig. 6 results are shown, using stations farther than a certain distance (900 m) from the shower axis, at a range where the difference between photon and hadron showers is more pronounced. A satisfactory qualitative agreement with the three-year old previous study has been found, see figures 5 and 6. The difference must be due to the evolution of the Auger analysis software.

For fitting the data in the selected region, in both figures 5 and 6, the following function

$$f(x) = p_0 + e^{p_1 + p_2 \cdot x} \quad (4)$$

has been used. The values of the best fit, the parameters p_0, p_1 and p_2, are provided in fig. 6.

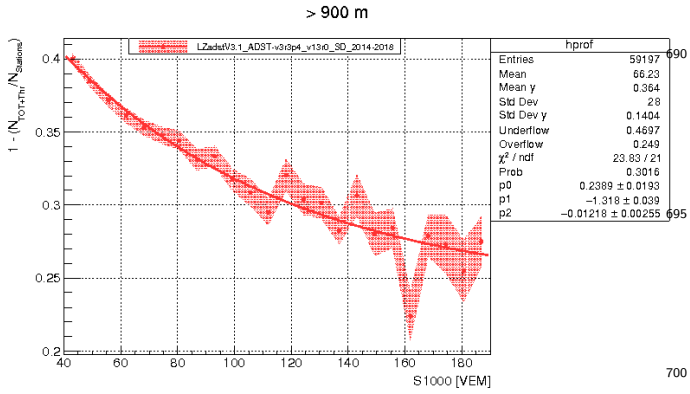

Figure 6: Trigger ratio vs S_{1000}.

6. Summary and Conclusion

In the highest observed energy region, the suppression of the flux above about $6{\cdot}10^{19}$ eV, which corresponds to the so-called "Greisen- Zatsepin-Kuzmin (GZK) cutoff energy", is confirmed by the results from the High-Resolution Flys Eye (HiRes) and the Pierre Auger Observatory (Auger). Summarizing the spectra observed from 10^{14} to 10^{20} eV with world wide experiments, there is still room for further investigations on the energy scale and the flux of primary cosmic rays. In order to establish the energy scale, it is necessary not only to understand the optical technique further, but also to determine the primary species in the highest energy region. Also, it is important to make more detailed measurements on the energy spectrum in the 10^{17} - 10^{18} eV region. To observe the super-GZK events and the anticipated recovery of the spectrum above the GZK cutoff, the search for the end of cosmic-ray energy spectrum will be continued even after a century since the discovery of cosmic rays in 1912.

The image of a mixed composition around the ankle and a heavier composition at the highest energies is strengthened by different composition studies, and by anisotropy searches at small angular scales at the highest energies. The present photon limits also disfavour pure proton composition models. Top-down models were already disfavoured by results on UHE neutrino and photon fluxes, leading to an astrophysical source explanation, but no clear clue on any existing UHECR source has been revealed so far. The hint of dipolar structure in the arrival direction is a step forward in the understanding of the transitions between the galactic and extragalactic components. The comparison of measurements with model predictions remains a delicate operation, knowing that serious hints for deficiencies in UHE interaction models have been observed. The astrophysical scenario resulting from Auger measurements is very complex and cannot at present be understood in terms of a unique interpretation for the sources, propagation and composition of the UHECRs. The great value of these overall results will be reinforced by the knowledge of the nature of the UHECR primaries, event by event. This will be the key to answering the open questions on the highest energy and the suppression region.

Search for ultra-high energy photons is an interesting field with high discovery potential. With new triggering algorithm and additional composition sensitivity of the planned upgrade of the Pierre Auger Observatory "*AugerPrime*" will increase the sensitivity to photons significantly. By 2024 it is expected to lower the photon limits with the PAO to reach the band of even conservative predictions for GZK photons - or discover ultra-high energy photons. It is expected that the limits will improve further, mainly at the low-energy end, due to optimized trigger algorithms. So it is just a matter of time until A) EeV photons are detected (with sufficient statistics), what would open a new window of astronomy, or B) the existence of EeV photons is disproved, what would role up the current understanding of physical principles. The directional search will also profit from the upgrade enabling sophisticated point source studies or even allow a detection of photons from specific sources.

The astrophysical puzzle is not only the pure existence of particles with energies exceeding 10^{20} eV, but added to the puzzle is the fact that the reconstructed directions of UHECRs do not point back to astrophysical sources [63].

Determining the UHECR mass composition, including identification of photons or setting upper limits on their fluxes ([4]), is an effort towards distinguishing between the two major classes which should give a hint on photon production and properties at the highest energies. Moreover, it is worth emphasizing that any result on UHE photons, including non-observation, is meaningful for the foundations of physics at the highest energies, allowing constraints on e.g. Lorentz invariance violation (LIV), QED nonlinearities, space-time structure or the already mentioned "top-down" scenarios (sec. 2.3.2). [3]

Acknowledgement

I would like to thank my colleagues from the Center for Astrophysics and Cosmology (from the University of Nova Gorica) and the Pierre Auger Collaboration for many fruitful discussions. I also thank the reviewers for their valuable comments on earlier versions of the manuscript, which helped to improve the paper. This work is supported by **coffee**.

Vielen Dank euch allen!

AppendixA. Difficult Stuff

AppendixB. More Difficult Stuff

AppendixB.1. Extreme Difficult Stuff

References

[1] I. Bartos, M. Kowalski, *Multimessenger Astronomy*, 2399-2891, IOP Publishing, 2017. doi:10.1088/978-0-7503-1369-8 URL http://dx.doi.org/10.1088/978-0-7503-1369-8

[2] M. Branchesi, *Multi-messenger astronomy: gravitational waves, neutrinos, photons, and cosmic rays*, Journal of Physics: Conference Series 718 (2) (2016) 022004. URL http://stacks.iop.org/1742-6596/718/i=2/a=022004

[3] P. Homola, for the Pierre Auger Collaboration, *Search for Ultra-High Energy Photons with the Pierre Auger Observatory*, ArXiv e-prints arXiv:1804.05613

[4] A. Aab, et al., *The Pierre Auger Observatory Upgrade - Preliminary Design Report* arXiv:1604.03637

[5] M. Nagano, *Search for the end of the energy spectrum of primary cosmic rays*, New Journal of Physics 11 (6) (2009) 065012. URL http://stacks.iop.org/1367-2630/11/i=6/a=065012

[6] Berat, Corinne, *The Pierre Auger Observatory status and latest results*, EPJ Web Conf. 136 (2017) 02017. doi:10.1051/epjconf/201713602017. URL https://doi.org/10.1051/epjconf/201713602017

[7] L. J. Watson, D. J. Mortlock, A. H. Jaffe, *A Bayesian analysis of the 27 highest energy cosmic rays detected by the Pierre Auger Observatory*, Mon. Not. Roy. Astron. Soc. 418 (2011) 206. arXiv:1010.0911, doi:10.1111/j.1365-2966.2011.19476.x.

[8] S. Liberati, *Quantum gravity phenomenology via Lorentz violations*, PoS P2GC (2007) 018. arXiv:0706.0142, doi:10.22323/1.034.0018.

[9] P. Homola, D. Gora, D. Heck, H. Klages, J. Pekala, M. Risse, B. Wilczynska, H. Wilczynski, *Simulation of ultrahigh energy photon propagation in the geomagnetic field*, Comput. Phys. Commun. 173 (2005) 71. arXiv:astro-ph/0311442, doi:10.1016/j.cpc.2005.07.001.

[10] M. G. Aartsen, et al., *Neutrino Interferometry for High-Precision Tests of Lorentz Symmetry with IceCube* arXiv:1709.03434

[11] S. R. Coleman, S. L. Glashow, *High-energy tests of Lorentz invariance*, Phys. Rev. D59 (1999) 116008. arXiv:hep-ph/9812418, doi:10.1103/PhysRevD.59.116008.

[12] A. MacFadyen, S. E. Woosley, *Collapsars: Gamma-ray bursts and explosions in 'failed supernovae'*, Astrophys. J. 524 (1999) 262. arXiv:astro-ph/9810274, doi:10.1086/307790.

[13] S. E. Woosley, J. S. Bloom, *The Supernova Gamma-Ray Burst Connection*, Ann. Rev. Astron. Astrophys. 44 (2006) 507–556. arXiv:astro-ph/0609142, doi:10.1146/annurev.astro.43.072103.150558.

[14] E. Waxman, J. N. Bahcall, *High-energy neutrinos from cosmological gamma-ray burst fireballs*, Phys. Rev. Lett. 78 (1997) 2292–2295. arXiv:astro-ph/9701231, doi:10.1103/PhysRevLett.78.2292.

[15] J. P. Rachen, P. Meszaros, *Photohadronic neutrinos from transients in astrophysical sources*, Phys. Rev. D58 (1998) 123005. arXiv:astro-ph/9802280, doi:10.1103/PhysRevD.58.123005.

[16] V. Berezinsky, M. Kachelriess, A. Vilenkin, *Ultrahigh-energy cosmic rays without GZK cutoff*, Phys. Rev. Lett. 79 (1997) 4302–4305. arXiv:astro-ph/9708217, doi:10.1103/PhysRevLett.79.4302.

[17] M. Birkel, S. Sarkar, *Extremely high-energy cosmic rays from relic particle decays*, Astropart. Phys. 9 (1998) 297–309. arXiv:hep-ph/9804285, doi:10.1016/S0927-6505(98)00028-0.

[18] V. A. Kuzmin, V. A. Rubakov, *Ultrahigh-energy cosmic rays: A Window to postinflationary reheating epoch of the universe?*, Phys. Atom. Nucl. 61 (1998) 1028. arXiv:astro-ph/9709187.

[19] P. Blasi, R. Dick, E. W. Kolb, *Ultra-high energy cosmic rays from annihilation of superheavy dark matter*, Astroparticle Physics 18 (1) (2002) 57 – 66. doi:https://doi.org/10.1016/S0927-6505(02)00113-5. URL http://www.sciencedirect.com/science/article/pii/S0927650502001135

[20] C. T. Hill, *Monopolonium*, Nuclear Physics B 224 (3) (1983) 469 – 490. doi:https://doi.org/10.1016/0550-3213(83)90386-3. URL http://www.sciencedirect.com/science/article/pii/0550321383903863

[21] P. Goddard, P. Mansfield, *Topological structures in field theories*, Reports on Progress in Physics 49 (7) (1986) 725. URL http://stacks.iop.org/0034-4885/49/i=7/a=001

[22] T. Weiler, *Resonant Absorption of Cosmic-Ray Neutrinos by the Relic-Neutrino Background*, Phys. Rev. Lett. 49 (1982) 234–237. doi:10.1103/PhysRevLett.49.234. URL https://link.aps.org/doi/10.1103/PhysRevLett.49.234

[23] T. J. Weiler, *Cosmic ray neutrino annihilation on relic neutrinos revisited: A Mechanism for generating air showers above the Greisen-Zatsepin-Kuzmin cutoff*, Astropart. Phys. 11 (1999) 303–316. arXiv:hep-ph/9710431, doi:10.1016/S0927-6505(98)00068-1.

[24] D. Fargion, B. Mele, A. Salis, *Ultra-High-Energy Neutrino Scattering onto Relic Light Neutrinos in the Galactic Halo as a Possible Source of the Highest Energy Extragalactic Cosmic Rays*, The Astrophysical Journal 517 (2) (1999) 725. URL http://stacks.iop.org/0004-637X/517/i=2/a=725

[25] J. Ellis, V. E. Mayes, D. V. Nanopoulos, *Ultrahigh-energy cosmic rays particle spectra from crypton decays*, Phys. Rev. D 74 (2006) 115003. doi:10.1103/PhysRevD.74.115003. URL https://link.aps.org/doi/10.1103/PhysRevD.74.115003

[26] Z. Fodor, S. D. Katz, *Grand unification signal from ultrahigh-energy cosmic rays?*, Phys. Rev. Lett. 86 (2001) 3224–3227. arXiv:hep-ph/0008204, doi:10.1103/PhysRevLett.86.3224.

[27] S. Sarkar, R. Toldr, *The high energy cosmic ray spectrum from relic particle decay*, Nuclear Physics B 621 (1) (2002) 495 – 520. doi:https://doi.org/10.1016/S0550-3213(01)00565-X URL http://www.sciencedirect.com/science/article/pii/S055032130100565X

[28] C. Barbot, M. Drees, *Detailed analysis of the decay spectrum of a super heavy X particle*, Astropart. Phys. 20 (2003) 5–44. arXiv:hep-ph/0211406, doi:10.1016/S0927-6505(03)00134-8.

[29] R. Aloisio, V. Berezinsky, M. Kachelriess, *Fragmentation functions in supersymmetric QCD and ultrahigh energy cosmic ray spectra produced in top-down models*, Phys. Rev. D 69 (2004) 094023. doi:10.1103/PhysRevD.69.094023. URL https://link.aps.org/doi/10.1103/PhysRevD.69.094023

[30] S. Sarkar, *New physics from ultrahigh-energy cosmic rays*, Acta Phys. Polon. B35 (2004) 351–364. arXiv:hep-ph/0312223.

[31] S. Lee, A. V. Olinto, G. Sigl, *Extragalactic Magnetic Field and the Highest Energy Cosmic Rays*, The Astrophysical Journal Letters 455 (1) (1995) L21. URL http://stacks.iop.org/1538-4357/455/i=1/a=L21

[32] M. Risse, P. Homola, R. Engel, D. Góra, D. Heck, J. Pekala, B. Wilczyńska, H. Wilczyński, *Photon air showers at ultra-high energy and the photonuclear cross-section*, Czechoslovak Journal of Physics 56 (1) (2006) A327–A336. doi:10.1007/s10582-006-0166-7. URL https://doi.org/10.1007/s10582-006-0166-7

[33] E. Gabrielli, K. Huitu, S. Roy, *Photon propagation in magnetic and electric fields with scalar/pseudoscalar couplings: A New look*, Phys. Rev. D74 (2006) 073002. arXiv:hep-ph/0604143, doi:10.1103/PhysRevD.74.073002.

[34] M. Fairbairn, T. Rashba, S. Troitsky, *Photon-axion mixing and ultra-high energy cosmic rays from BL Lac type objects: Shining light through the Universe*, Phys. Rev. D 84 (2011) 125019. doi:10.1103/PhysRevD.84.125019. URL https://link.aps.org/doi/10.1103/PhysRevD.84.125019

[35] G. B. Gelmini, O. E. Kalashev, D. V. Semikoz, *GZK Photons Above 10-EeV*, JCAP 0711 (2007) 002. arXiv:0706.2181, doi:10.1088/1475-7516/2007/11/002.

[36] P. Bhattacharjee, G. Sigl, *Origin and propagation of extremely high-energy cosmic rays*, Phys. Rept. 327 (2000) 109–247. arXiv:astro-ph/9811011, doi:10.1016/S0370-1573(99)00101-5.

[37] S. Sikora, Ł. Bratek, J. Jałocha, M. Kutschera, *Motion of halo tracer objects in the gravitational potential of a low- mass model of the Galaxy*, AAP 579 (2015) A134. doi:10.1051/0004-6361/201526189.

[38] L. Maccione, S. Liberati, *GZK photon constraints on Planck scale Lorentz violation in QED*, JCAP 0808 (2008) 027. arXiv:0805.2548, doi:10.1088/1475-7516/2008/08/027.

[39] J. Ellis, N. E. Mavromatos, D. V. Nanopoulos, *Space-time foam effects on particle interactions and the Greisen-Zatsepin-Kuzmin cutoff*, Phys. Rev. D 63 (2001) 124025. doi:10.1103/PhysRevD.63.124025. URL https://link.aps.org/doi/10.1103/PhysRevD.63.124025

[40] A. Almheiri, D. Marolf, J. Polchinski, J. Sully, *Black Holes: Complementarity or Firewalls?*, JHEP 02 (2013) 062. arXiv:1207.3123, doi:10.1007/JHEP02(2013)062.

[41] [link]. URL https://credo.science/

[42] F. Tavecchio, M. Roncadelli, G. Galanti, *Photons to axion-like particles conversion in Active Galactic Nuclei*, Physics Letters B 744 (2015) 375 – 379. doi:https://doi.org/10.1016/j.physletb.2015.04.017.
URL http://www.sciencedirect.com/science/article/pii/S0370269315002609

[43] C. Wang, D. Lai, *Axion-photon Propagation in Magnetized Universe*, JCAP 1606 (06) (2016) 006. arXiv:1511.03380, doi:10.1088/1475-7516/2016/06/006.

[44] [link]. URL http://www.amon.psu.edu/

[45] J. Abadie, et al., *Implications For The Origin Of GRB 051103 From LIGO Observations*, Astrophys. J. 755 (2012) 2. arXiv:1201.4413, doi:10.1088/0004-637X/755/1/2.

[46] M. W. E. Smith, et al., *The Astrophysical Multimessenger Observatory Network (AMON)*, Astropart. Phys. 45 (2013) 56–70. arXiv:1211.5602, doi:10.1016/j.astropartphys.2013.03.003.

[47] M. Risse, P. Homola, *Search for ultrahigh energy photons using air showers*, Mod. Phys. Lett. A22 (2007) 749–766. arXiv:astro-ph/0702632, doi:10.1142/S0217732307022864.

[48] J. Abraham, et al., *An upper limit to the photon fraction in cosmic rays above 10^{19}-eV from the Pierre Auger Observatory*, Astropart. Phys. 27 (2007) 155–168. arXiv:astro-ph/0606619, doi:10.1016/j.astropartphys.2006.10.004.

[49] Pierre Auger Collaboration, J. Abraham, P. Abreu, M. Aglietta, C. Aguirre, E. J. Ahn, D. Allard, I. Allekotte, J. Allen, P. Allison, et al., *Upper limit on the cosmic-ray photon fraction at EeV energies from the Pierre Auger Observatory*, Astroparticle Physics 31 (2009) 399–406. arXiv:0903.1127, doi:10.1016/j.astropartphys.2009.04.003.

[50] J. Abraham, et al., *Upper limit on the cosmic-ray photon flux above 10^{19} eV using the surface detector of the Pierre Auger Observatory*, Astropart. Phys. 29 (2008) 243–256. arXiv:0712.1147, doi:10.1016/j.astropartphys.2008.01.003.

[51] P. Abreu, et al., *The Pierre Auger Observatory III: Other Astrophysical Observations*, in: Proceedings, 32nd International Cosmic Ray Conference (ICRC 2011): Beijing, China, August 11-18, 2011, 2011. arXiv:1107.4805.
URL https://inspirehep.net/record/919729/files/arXiv:1107.4805.pdf

[52] A. Aab, P. Abreu, M. Aglietta, M. Ahlers, E. J. Ahn, I. Al Samarai, I. Albuquerque, I. Allekotte, J. Allen, P. Allison, A. Almela, J. Alvarez Castillo, J. Alvarez-Muiz, R. Alves Batista, M. Ambrosio, A. Aminaei, L. Anchordoqui, S. Andringa, C. Aramo, M. Ziolkowski, *PROBING THE RADIO EMISSION FROM COSMIC-RAY-INDUCED AIR SHOWERS BY POLARIZATION MEASUREMENTS*.

[53] L. D. Landau, I. Pomeranchuk, *Electron cascade process at very high-energies*, Dokl. Akad. Nauk Ser. Fiz. 92 (1953) 735–738.

[54] L. D. Landau, I. Pomeranchuk, *Limits of applicability of the theory of bremsstrahlung electrons and pair production at high-energies*, Dokl. Akad. Nauk Ser. Fiz. 92 (1953) 535–536.

[55] A. B. Migdal, *Bremsstrahlung and pair production in condensed media at high-energies*, Phys. Rev. 103 (1956) 1811–1820. doi:10.1103/PhysRev.103.1811.

[56] D. Heck, J. Knapp, J. N. Capdevielle, G. Schatz, T. Thouw, *CORSIKA: a Monte Carlo code to simulate extensive air showers.*, 1998.

[57] A. Aab, et al., *The Pierre Auger Cosmic Ray Observatory*, Nucl. Instrum. Meth. A798 (2015) 172–213. arXiv:1502.01323, doi:10.1016/j.nima.2015.06.058.

[58] A. Neronov, D. V. Semikoz, I. Vovk, R. Mirzoyan, *Cosmic-ray composition measurements and cosmic ray background-free γ-ray observations with Cherenkov telescopes*, Phys. Rev. D94 (12) (2016) 123018. arXiv:1610.01794, doi:10.1103/PhysRevD.94.123018.

[59] K. Almeida Cheminant, et al., *Search for electromagnetic superpreshowers using gamma-ray telescopes*, PoS ICRC2017 (2017) 860. arXiv:1709.05180.

[60] N. Dhital, P. Homola, J. F. Jarvis, P. Poznanski, K. Almeida Cheminant, Ł. Bratek, T. Bretz, D. Gora, P. Jagoda, J. Jałocha, K. Kopanski, D. Lemanski, M. Magrys, V. Nazari, J. Niedzwiedzki, M. Nocun, W. Noga, A. Ozieblo, K. Smelcerz, K. Smolek, J. Stasielak, S. Stuglik, M. Sułek, O. Sushchov, J. Zamora-Saa, *We are all the Cosmic-Ray Extremely Distributed Observatory*, ArXiv e-prints arXiv:1709.05196.

[61] [link]. URL http://ipnwww.in2p3.fr/~augers/AugerProtected/herald.php

[62] M. Niechciol, M. Risse, P. Ruehl, M. Settimo, P. W. Younk, A. Yushkov, *F: A new observable for photon-hadron discrimination in hybrid air shower events*, Astroparticle Physics 97 (2018) 88–95. arXiv:1710.06586, doi:10.1016/j.astropartphys.2017.10.004.

[63] Pierre Auger Collaboration, P. Abreu, M. Aglietta, E. J. Ahn, I. F. M. Albuquerque, D. Allard, I. Allekotte, J. Allen, P. Allison, J. Alvarez Castillo, et al., *Anisotropy and chemical composition of ultra-high energy cosmic rays using arrival directions measured by the Pierre Auger Observatory*, JCAP 6 (2011) 022. arXiv:1106.3048, doi:10.1088/1475-7516/2011/06/022.

NUMERICAL SIMULATIONS OF THE DOUBLE FLOW FOCUSING NOZZLES

Grega Belšak

Laboratory for Simulation of Materials and Processes

Institute of Metals and Technology

Lepi pot 11, SI-1000 Ljubljana, Slovenia

email: grega.belsak@imt.si

Abstract

The formation of a micro jet produced with a double flow focusing nozzle is studied numerically. A multiphase model is considered in which the fluid flow of three immiscible Newtonian fluids is axisymmetric and laminar. Two liquid phases are considered to be incompressible. A novelty of treating the gaseous phase as a compressible gas is introduced for the first time for such a three phase micrometer size nozzle system. The effects of operating parameters on the jets stability in the vacuum conditions are investigated. Simulation results are compared to the experimental results and show a good agreement in critical parameters.

Keywords: multiphase flow, micro jet, double flow focusing nozzle

1. Introduction

The function of a complex organic molecule is (largely) determined by its molecular structure. Therefore in order to fully understand the behavior of such biological nanocrystals their structure needs to be precisely studied. One of the possible ways of doing this is through the experiment called serial femtosecond crystallography (SFX) [2]. This experiment requires a steady supply of nanocrystals, which are delivered in a form of a high speed micro jet into a femtosecond long X-ray beams. Scattering of an intense X-ray light on the organic nanocrystals creates diffraction patterns, which are recorded on a detector. By collecting a vast amount of diffraction patterns, structure of

the studied biological sample can be deduced. The aforementioned delivery jets are an essential part of the SFX experiment and therefore the controlled production of these liquid micro jets is of great importance and is studied here numerically. Liquid micro jets are typically produced with nozzles by means of a co-flowing immiscible fluid stream. Manual preparation of such nozzles is limited to simple designs, non-reproducible and immensely time consuming. Ceramic micro-injection moulded nozzles [1] ensure faster assembly and better reproducibility but are still limiting to simple designs. A complex nozzle structure presented in this paper could not be manufactured in the conventional ways but it is easily constructed with a 3D printing technology [5]. This additive manufacturing technique allows for greater freedom in nozzle designs, speeds up the fabrication process and can create virtually identical nozzles with a very high precision. Numerical simulations presented here are complementary to the experimental data and give an insight in the fluid dynamics of such systems.

2. Double flow focusing nozzle

DePonte [3] proposed the production of the micro sized liquid jets through flow focusing apparatus called gas dynamic virtual nozzle (GDVN). This device uses two fluids and consists of two capillaries. The inner capillary is used to deliver the liquid sample (water) to the nozzle orifice while the outer capillary is fed with high pressure gas (helium). Gas phase, which is being hydro-dynamically focused by the converging nozzle structure, transfers the momentum and energy to the liquid phase and in the process thinness, prolongs and speeds up the jet. To get the (desired) stable jet with the GDVN structure, liquid flow rates of 20-40 $\mu L/min$ are necessary. Since the crystal samples used in SFX experiments are expensive and difficult to produce, it is necessary to minimize their consumption. This lowering of already minuscule liquid flow rate is achieved by the use of double flow focusing nozzles (DFFN). Double flow focusing nozzle [6] which is depicted in figure 1 uses an additional focusing liquid phase. In such a way a so called jet-in-jet structure is formed, meaning a jet which has inside another jet is produced. Main advantage behind choosing such a DFFN nozzle structure is that it produces longer jet compared to GDVN nozzle structure. Surface tension force in such liquid systems is a dominant force in droplet formation, meaning its value dictates where the transition from a continuous jet stream phase to the droplet phase will occur. Simply put, it dictated the length of

a jet. Higher the surface tension, shorter the jet length and vice-versa. For this reason the focusing liquid is chosen to have its surface tension lower than that of a sample liquid. With this kind of nozzle structure a stable jet can be obtained for sample liquid flow rates as low as 5 $\mu L/min$. In the Figure 1 a scheme of such system is depicted.

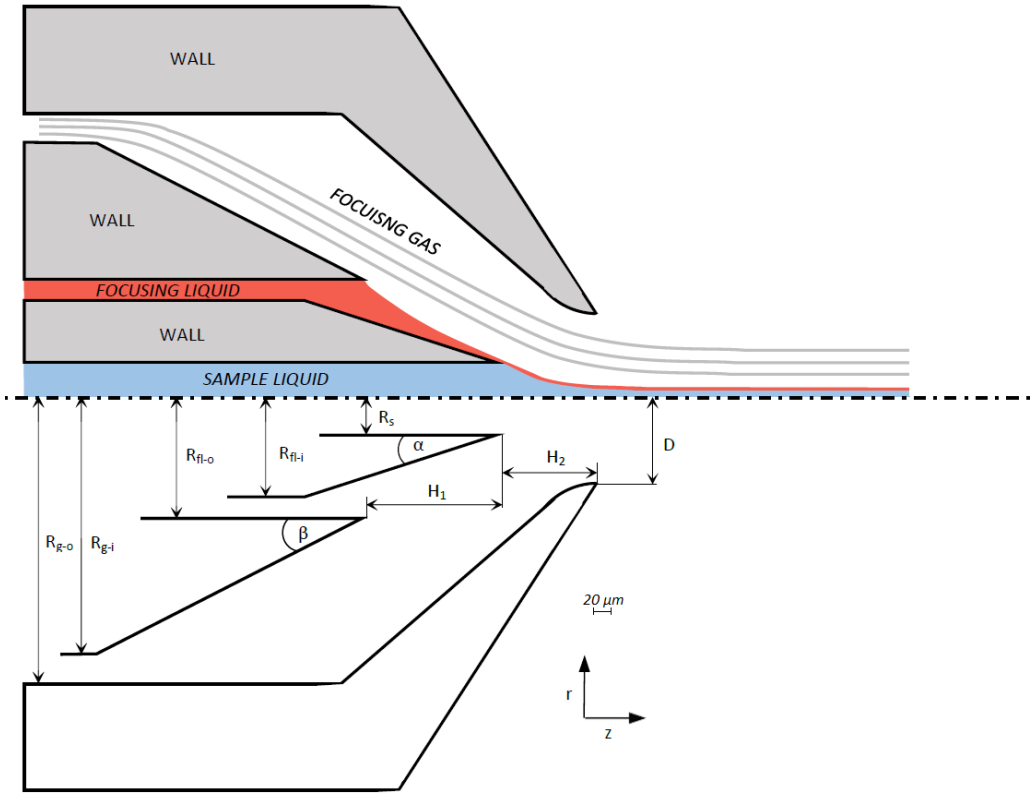

Figure 1: Schematic representation of the DFFN nozzle structure showing the capillaries by which the fluids are delivered into the nozzle. For scale typical orifice diameter D lies between 70 and 80 micrometers.

Physical properties of the three fluids used can be found in Table 1, followed by the operating conditions used for the simulations in Table 2.

	focusing gas **HELIUM**	focusing liquid **ALCOHOL**	sample liquid **WATER**
density [kg/m^3]	variable	789	1000
dynamic viscosity [kg/ms]	10^{-3}	$1.12*10^{-3}$	$1.9*10^{-3}$

Table 1: Physical properties of the fluids

case number	**helium** flow rate [mg/min]	**alcohol** flow rate $[\mu L/min]$	**water** flow rate $[\mu L/min]$
1	22	7	4.5
2	17	5.5	4.5
3	21	7	5
4	21	8.4	6.6

Table 2: Operating parameters for calculated cases.

3. Governing equation and numerical method

3.1. Governing equation

The physical problem of compressible flow is governed by a set of mass, momentum and energy conservation equations for each of the phases i:

$$\frac{\delta \rho_i}{\delta t} + \nabla \cdot (\rho_i \vec{u_i}) = 0 \tag{1}$$

$$\frac{\delta (\rho_i \vec{u_i})}{\delta t} + \nabla \cdot (\rho_i \vec{u_i} \vec{u_i}) = -\nabla P_i + \nabla \cdot \bar{\tau} + \rho_i \vec{g} + \vec{f_{\sigma,i}} \tag{2}$$

$$\frac{\delta (\rho_i e_i)}{\delta t} + \nabla \cdot (\rho_i \vec{u_i} e_i) = -\nabla \cdot (P_i \vec{u_i}) + \nabla \cdot (\bar{\tau} \vec{u_i}) - \nabla \cdot q \tag{3}$$

where $\bar{\tau}$ represents the viscous stress tensor $\bar{\tau} = \mu[(\nabla \vec{u_i}) + (\nabla \vec{u_i})^T]$, e_i total energy $e_i = c_{v,i} T_i + 0.5 \|\vec{u_i}\|^2$ and q conduction heat flux $q = -k \nabla T$. Velocity, density, viscosity, pressure, surface tension force, temperature, gravitational acceleration and thermal conductivity are given by $\vec{u_i}, \rho_i, \mu_i, P_i, \vec{f_{\sigma,i}}, T, \vec{g}$ and k, respectively.

3.2. Numerical method

The governing equations were solved using open source code for computational fluid dynamics called OpenFOAM [7], more specifically a slightly modified solver called compressibleMultiphaseInterFoam was used for the calculations. Symmetry of DFFN nozzle system allows for two dimensional numerical simulation with axis-symmetry, which greatly reduces the number of computational volumes needed to simulate such a complex system. To further decrease computational time, the mesh refinement was concentrated on the areas of the developing jet and a coarser mesh was used elsewhere (schematic of the mesh in presented in Figure 2). It was found that a mesh resolution of around 60 nm was needed to be able to distinguish between the two liquid phases in the thin jet. This resulted in a mesh consisting of around half a million cells. Even though the mesh was optimized the time needed to calculate one case exceeded one month on a supercomputer. For this reason a small number of cases were calculated.

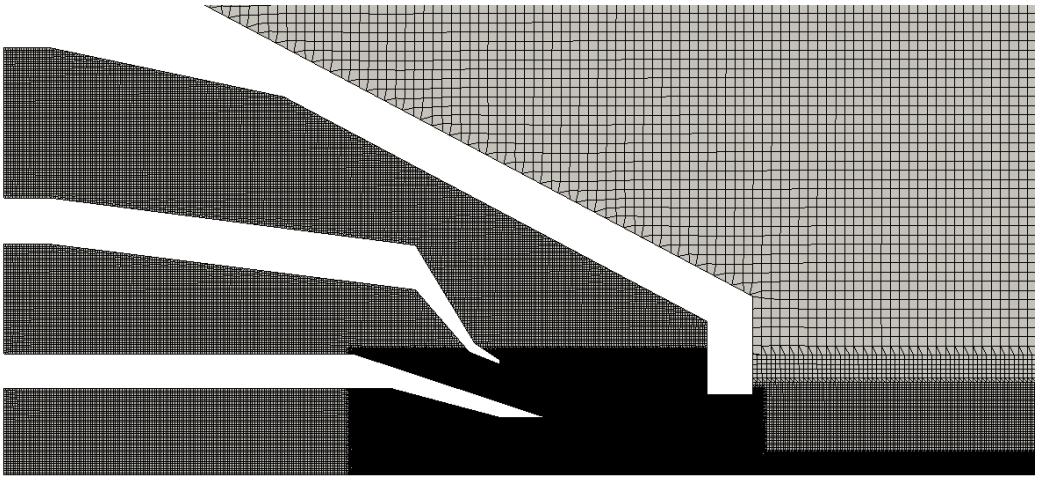

Figure 2: Sample mesh of the double flow focusing nozzle used in simulation. Mesh consists of approximately 300 000 cells where the highest resolution cells are the size of 0.25 μm and are concentrated in the jet forming region.

There are many difficulties in simulating the DFFN system and for the reasons described below this has not yet been attempted. Primary difference of this paper with respect to the others trying to tackle this problem is the treatment of the gaseous phase as a compressible fluid. The flow behaviour of a gas through the nozzle as an incompressible fluid differs notably in

comparison to the flow as a compressible fluid. At best we can say is that the incompressible treatment is a good approximations, but in no means properly describes realistic flow conditions. For this reason a physical model which incorporates the compressibility was chosen. Second difficulty arises from near perfect vacuum conditions used in the experiment. The treatment of extremely low pressures, low temperatures and high velocities that occur under such vacuum conditions are difficult to treat numerically.

4. Numerical results and discussion

The quality of the results from SFX experiments relay on four different jet properties: stability, length, diameter and velocity. Since the jet breakup process is difficult to describe numerically it falls out of the scope of the present paper. Other three crucial properties are extracted from the performed simulations and evaluated here.

4.1. Stability

In flow focusing problems three main regimes of operations exist: whipping, dripping and jetting mode [4]. Whipping mode usually occurs at high gas flow rates or non-axial alignments of the inner capillaries with the outer ones. In such a mode jet oscillates around its axis. This requires the simulations to be performed in three dimensions and because of this such modes will not be discussed here. The main distinction between other two modes is the behaviour of the jet meniscus. Dripping mode occurs when pulsating, time varying jet meniscus is observed. If the droplet separation does not cause the jet meniscus to fluctuate a jetting regime is achieved. All the cases considered here are of the jetting mode, hence stable.

4.2. Diameter

The SFX experiment strives for as thin of a jet as possible in order to get as little diffraction interference signal from the two liquids itself. This is constrained by previously mentioned stability parameter and the minimum liquid flow rates. Here the jet diameter is measured at the nozzle orifice and plotted with respect to sample liquid flow rate and focusing liquid flow rate.

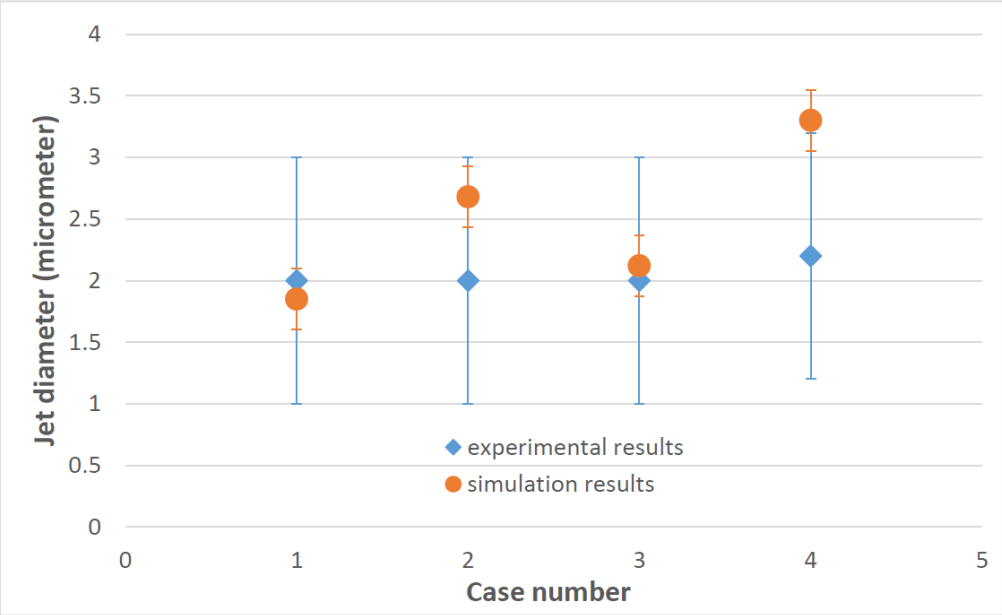

Figure 3: Graph comparing experimental (blue) and simulated (orange) diameter results for four different cases. Over-plotted are the error bars.

4.3. Velocity

As before mentioned the experiment uses a series of powerful x-ray beams which are focused to a point on a jet leaving the nozzle at around 100 m from the orifice. The energy intensity of a laser is such that it destroys the sample and it is necessary that the destroyed part is moved away quickly before new beam of light hits. It is for such a reason that SFX experiment requires jets as fast as possible.

Velocity profile through the jet axis is depicted in the figure 4. In order to visualize where the actual acceleration occurs the nozzle structure is over plotted with a black line. It can be observed that the jet gains its momentum partially inside the nozzle structure and partially outside in the vacuum chamber. This goes to show that even in very low density environment the high speed stream of gas is able to accelerate the jet. It can also be observed where the droplet separation starts happening (discontinued red line)

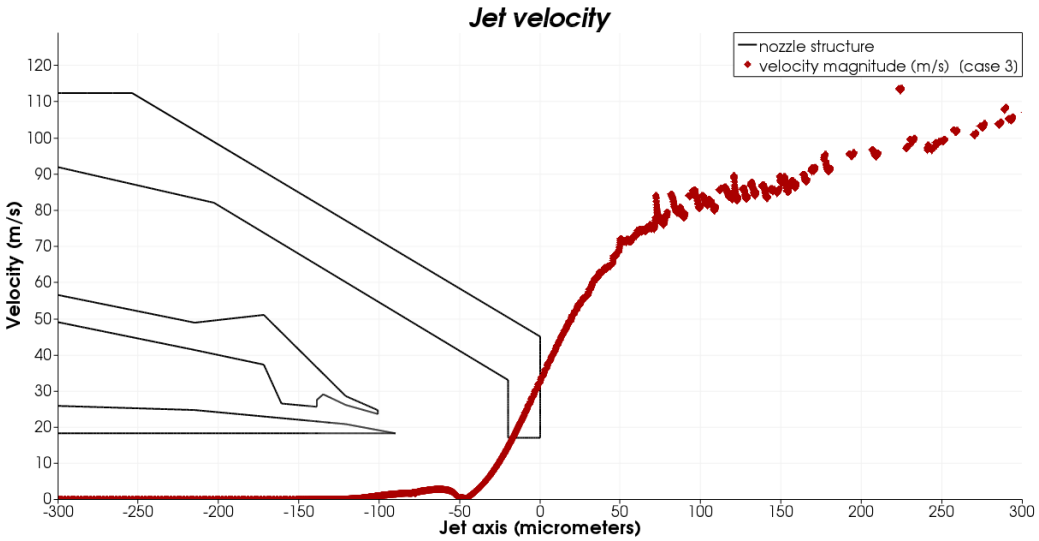

Figure 4: Simulated jet velocity as measured through the jet axis at one time step. Red is line showing jet velocity, where the breakage of the line denotes the formation of a droplet. In order to see where in the domain the jet is being accelerated the nozzle structure is depicted in black solid line.

5. Conclusions

Behaviour of DFFN was investigated numerically in order to compare it to the experimental results. To realistically describe a gas flow through a convergent nozzle into the vacuum chamber a compressible model was used. Since the operating condition of our system show the presence of the chocked flow in the nozzle throat and an expansion of the gas in the vacuum chamber compressibility needed to be taken into account. This step was essential and a big improvement from the simulations done earlier, where gas was treated as incompressible. Comparing the simulated results with the experiment show a good agreement with the experiment. Diameter matches in all four cases within the error bars and the diameter data extracted from future simulations is realible. Velocity profile revealed that the jet is being accelerated also when it exits the nozzle. It was previously believed that due to low pressure condition just outside the nozzle, basically vacuum conditions, the forces exerted on the jet are not sufficient in order to accelerate the jet. Simulation show, that this is not the case and the jet gains roughly half of its momentum outside the nozzle structure. It should be pointed out that there are mayor numerical difficulties in simulating the jet breakup process

and this is an active area of research. Future work will focus on simulating the total jet shape, not only diameter but also the length. Additionally the model can be improved by allowing for the variability of the gas viscosity and liquid surface tension with the temperature.

6. References

[1] Beyerlein, K.R., et al. 2015. Ceramic micro-injection molded nozzles for serial femtosecond crystallography sample delivery. Review of Scientific Instruments 86, 12.
doi:10.1063/1.4936843.

[2] Chapman, H.N., et al. 2011. Femtosecond X-ray protein nanocrystallography. Nature 470, 7332: 73–77.
doi:10.1038/nature09750.

[3] DePonte, D.P., et al. 2008. Gas dynamic virtual nozzle for generation of microscopic droplet streams. Journal of Physics D: Applied Physics 41, 19: 195505.
doi:10.1088/0022-3727/41/19/195505.

[4] Gañán-Calvo, A.M. 1998. Generation of Steady Liquid Microthreads and Micron-Sized Monodisperse Sprays in Gas Streams. Physical Review Letters
doi:10.1103/PhysRevLett.80.285.

[5] Nelson, G., et al. 2016. Three-dimensional-printed gas dynamic virtual nozzles for x-ray laser sample delivery. Optics Express
doi:10.1364/OE.24.011515.

[6] Oberthuer, D., et al. 2017. Double-flow focused liquid injector for efficient serial femtosecond crystallography. Scientific Reports 7: 44628.
doi:10.1038/srep44628.

[7] OpenFOAM. 2014. OpenFOAM - The Open Source CFD Toolbox - User Guide. Tehn. por.
doi:10.1023/A.

Phase field modeling of dendritic growth by local radial basis function collocation method

Tadej Dobravec[a], Boštjan Mavrič[a,b], Božidar Šarler[a,b,*]

[a]*Laboratory for Simulation of Materials and Processes, Institute of Metals and Technology, Lepi pot 11, 1000 Ljubljana, Slovenia*
[b]*Laboratory for Fluid Dynamics and Thermodynamics, Faculty of Mechanical Engineering, University of Ljubljana, Aškerčeva 6, 1000 Ljubljana, Slovenia*

Abstract

A two-dimensional model to simulate the dendritic growth in pure melt is developed. Phase field model is used to derive the system of partial differential equations describing the temporal evolution of the solid-liquid interface and temperature field. Quantitative simulations are assured by the use of model parameters obtained by the thin-interface limit of the phase field model. Local radial basis function collocation method and explicit Euler scheme are used for the spatial and temporal discretization of the phase field equations, respectively. The spatial and temporal convergence of the method on uniform and non-uniform node arrangements are verified by comparison with the solution obtained by Green function method. Dendrites at different preferential growth directions are compared to the reference state in order to examine the influence of node arrangement to the dendrite morphology. Advantages and shortcomings of the numerical method as well as further developments are discussed.

Keywords: solidification, pure melt, dendritic growth, phase field, meshless methods, radial basis function, local collocation method

1. Introduction

The microstructure evolution during solidification has a significant effect on the material properties of the final product. The morphologies of solid phases, distribution of impurities along solidified material and other features impact the material properties, e.g., large-scale construction engineering requires high strength steels consisting of combination of refined grains and dispersion of soft and hard phases. A large spectrum of different solidification patterns occurs, e.g., dendritic, eutectic and peritectic growth, when solidification in metals is considered [1–3]. The understanding of physical phenomena, determining those patterns, is crucial for the design and production of the high-quality castings for the scientific and industrial use [4].

Theoretical studies and numerical models represent a powerful tool for the prediction of the microstructure evolution and can be therefore used for the in-depth understanding and optimization of the solidification process [1]. The microstructure evolution is modelled by a set of mathematical equations incorporating the heat and solute transport along with appropriate boundary conditions between various phases. Example of such model is famous Stefan problem, describing solidification in pure material. Stefan problem is example of sharp-interface model, which operates on scales much larger than solid-liquid interface width and incorporate all information from the atomic scale through effective constants like the capillary length [5]. There are two main limitations in the sharp-interface models: 1. for many classes of phenomena appropriate sharp-interface models are not known, and 2. numerical implementation is very difficult.

In the 1980s continuum phase field method (PFM) was introduced in the field of modelling free boundary problems in materials science [6, 7]. There are two main reasons why PFM became ”the method of choice” for modelling of this phenomena: 1. it has fundamental origins in thermodynamics, and 2. it does not require explicit tracking of interfaces between phases.

The main hallmark of PFM is introduction of phase field (PF) or order parameter, a continuous field representing phases. PF is constant in the bulk of each phase and varies across the thin boundary layer between phases. From the point of view of condensed matter physics, PF can be seen as degree of crystallinity or atomic order in a phase, while the thin boundary layer represents an atomically diffuse interface. From the point of view of mathematical modelling, PF represents a tool for describing time evolution of phases, as tracking of exact position of interfaces between phases is no longer necessary.

PF models are to thermodynamics linked through free energy functional, dependent on PF and other relevant variables, e.g., temperature, solute concentration, etc. A dissipative minimization of free energy functional yields a set of non-linear partial differential equations governing the movement of interfaces between phases and the heat and mass transfer. Parameters of those equations are obtained through the use of asymptotic analysis, as PF model has to yield sharp-interface solution in the limit of very thin interfaces.

The name ”phase field model” was introduced in the realm of modelling free boundary problems in material science in the 1980s, when scientists, modelling the solidification in a pure melt, were trying to avoid the explicit tracking of the solid-liquid interface by introducing a diffuse interface [8–10]. The idea was not new; over a century ago in 1893, Van der Waals proposed diffuse-interface description of a density field

*Corresponding author.
Email address: bozidar.sarler@imt.si (Božidar Šarler)

in a liquid-gas system [11, 12]. Similar approach is used in magnetic domain theory by Landau and Lifshitz in 1935 [13]. In 1958 Cahn and Hilliard introduced diffuse-interface theory [14], followed by work of Cahn on spinodal decomposition [15]. In 1977 Allen and Cahn studied non-conserved long range order parameter [16], while Hohenberg and Halperin studied critical dynamics by diffuse interface models[17].

The numerical implementations of first PF models for simulating the solidification in a pure melt [8–10] are straightforward [18–20], due to fact, that they do not require explicit tracking of the solid-liquid interface. First PF models have, however, two limitations: 1. they are unable to simulate the important physical limit, when kinetic undercooling in Stefan Problem can be neglected, and 2. they use sharp-interface limit of PF model [9, 10, 18–22], which requires very thin interface width and consequently time-consuming simulations on large computational domains. Both limitations were removed with derivation of thin interface limit of PF model [23, 24], which allows quantitative modelling of dendritic growth in two and three dimensions.

Quantitative PF simulations of experimentally relevant situations are to a great extent possible due to fast growth of computational capabilities [25, 26]. A large number of different computational approaches have been developed in the last twenty years, e.g., 1. adaptive mesh refinement [27], 2. parallel simulations by using graphic processing units [28], 3. hybrid finite-difference and random-walk algorithms [29], 4. implicit time stepping and multi grid approaches [30, 31], and 5. up-scaling techniques [32].

In this paper meshless local radial basis function collocation method (LRBFCM) [33] is applied for spatial discretization of PF equations as simple explicit Euler scheme is used for time-marching. In LRBFCM the computational domain is divided into overlapping sub-domains. The collocation is performed in each sub-domain by using radial basis function and linear monomials as interpolation functions to calculate finite-difference-like coefficients of discretized differential operators. The simulation of dendritic growth using the LRBFCM is, to the best of our knowledge, reported for the first time in this study.

LRBFCM was first used to solve solid mechanics problems [34–36]. Considering transient problems, LRBFCM was first used for diffusion problems [33] and was later sucessfully applied to many different scientific and engineering problems, e.g, turbulent combined forced and natural convection problems [37], simulation of laminar backward facing step flow under magnetic field [38], simulation of macro-segregation [39], simulation of linear and transient thermoelasticity [40, 41] and multi-pass hot-rolling simulation [42].

The main advantages of LRBFCM and other meshless methods in comparison with mesh-based methods, e.g, finite difference, finite volume and finite element methods, are [43]: 1. easier implementation of h-adaptive algorithms, 2. easier treatment of free boundary problems, e.g., crack propagation, phase transformation, etc., 3. higher-order continuous shape functions, 4. non-local interpolation character, and 5. absence of mesh alignment sensitivity. The main shortcomings of meshless methods are [43]: 1. requirement for high order integration, 2. difficulties in implementation of essential boundary conditions, 3. difficulties in satisfying the Kronecker delta, and 4. in general are meshless methods computationally less effective than finite element method.

The contents of the paper are structured as follows. In Section 2 the governing equations are presented. The numerical model is formulated and verified in Sections 3 and 4, respectively. The conclusions and further directions are discussed in Section 5.

2. Governing equations

Solidification from a pure can be represented with the sharp-interface or the diffuse-interface models. In Section 2.1 sharp-interface model, also known as Stefan problem is presented, followed by introduction of diffuse-interface PF model in Section 2.2. Link between Stefan problem and PF model is presented in Section 2.3, since PF model has to yield sharp-interface solution in the limit, where interface can be assumed to be negligible compared to the other length scales, e.g, diffusion length, radius of curvature of a dendrite, etc. Initial and boundary conditions are presented in Section 2.4.

2.1. Sharp-interface model

By introducing dimensionless temperature $u = (T - T_m)/(L/c_p)$, where T, T_m, L and c_p stand for temperature, melting temperature, latent heat of fusion and specific heat at constant pressure, respectively, Stefan problem can be written as

$$\begin{aligned} \partial_t u &= \alpha \nabla^2 u, \\ \boldsymbol{v}^* \cdot \boldsymbol{n}^* &= \alpha \left(\nabla u_s|^* \cdot \boldsymbol{n}^* - \nabla u_\ell|^* \cdot \boldsymbol{n}^* \right), \\ u^* &= -d(\boldsymbol{n}^*)\kappa - \beta(\boldsymbol{n}^*)\boldsymbol{v}^* \cdot \boldsymbol{n}^*, \end{aligned} \tag{1}$$

where α, $\boldsymbol{v}^*$, $\boldsymbol{n}^*$, $\nabla u_s|^*$, $\nabla u_\ell|^*$, u^*, $d(\boldsymbol{n})$, κ and $\beta(\boldsymbol{n})$ stand for thermal diffusivity, the solid-liquid interface velocity, the normal to the solid-liquid interface, gradients of dimensionless temperature field at the solid-liquid interface in the solid (s) and in the liquid (ℓ) phase, dimensionless temperature at the solid-liquid interface, the capillarity length, the curvature of the solid-liquid interface and the kinetic coefficient, respectively. Thermal diffusivity is defined as $\alpha = k/(\rho c_p)$, where k and ρ stand for the thermal conductivity and density, respectively.

2.2. Diffuse-interface model

PF model is derived by introducing the order parameter ϕ, a continuous field, which is constant in the bulk of each phase and varies across the thin boundary layer between phases. The system of PF equations describing solidification from a pure melt is written as [5]

$$\begin{aligned} \tau(\boldsymbol{n})\partial_t \phi &= -g'(\phi) - \lambda u p'(\phi) + \nabla \cdot \left(W^2(\boldsymbol{n}) \nabla \phi \right) + \\ &+ \sum_{\xi=x,y} \partial_\xi \left(|\nabla \phi|^2 W(\boldsymbol{n}) \frac{\partial W(\boldsymbol{n})}{\partial(\partial_\xi \phi)} \right), \\ \partial_t u &= \alpha \nabla^2 u + h'(\phi) \partial_t \phi, \end{aligned} \tag{2}$$

where $g'(\phi)$, $p'(\phi)$ and $h'(\phi)$ stand for derivatives of dimensionless functions determining two stable phases at the melting temperature, ϕ-u coupling and excess heat production during solidification, respectively. $\lambda = \rho L^2/(Hc_pT_m)$ is the dimensionless parameter that controls the strength of the ϕ-u coupling, respectively, where H is the energy jump between two stable phases at the melting temperature. $\tau(\boldsymbol{n})$ and $W(\boldsymbol{n})$ stand for the characteristic time of attachment of atoms at the interface and the interface thickness, respectively, both dependent on the normal $\boldsymbol{n} = \nabla\phi/|\nabla\phi|$.

2.3. Thin-interface limit

The thin interface limit of PF equations, valid for $W(\boldsymbol{n}) \ll \alpha/v$, where v stand for characteristic interface velocity, links the functions $W(\boldsymbol{n})$ and $\tau(\boldsymbol{n})$ from PF model to functions $d(\boldsymbol{n})$ and $\beta(\boldsymbol{n})$ from sharp-interface model at the chosen values of the parameter λ and functions $g'(\phi)$, $p'(\phi)$ and $h'(\phi)$. It yields following relations [24]

$$d(\boldsymbol{n}) = \frac{a_1}{\lambda}\left(W(\boldsymbol{n}) + \partial_\theta^2 W(\boldsymbol{n})\right), \tag{3}$$

and

$$\beta(\boldsymbol{n}) = \frac{a_1}{\lambda}\frac{\tau(\boldsymbol{n})}{W(\boldsymbol{n})}\left(1 - a_2\lambda\frac{W(\boldsymbol{n})^2}{\alpha\tau(\boldsymbol{n})}\right), \tag{4}$$

where θ is angle between preferential growth direction and $\boldsymbol{n}$, while a_1 and a_2 stand for constants, dependent on the PF functions $g'(\phi)$, $p'(\phi)$, $h'(\phi)$. The choice of functions

$$\begin{aligned} g'(\phi) &= -\phi - \phi^3, \\ p'(\phi) &= (1-\phi^2)^2, \\ h'(\phi) &= \frac{1}{2}, \end{aligned} \tag{5}$$

yields $a_1 = 0.8839$, $a_2 = 0.6267$ and defines the operating window for order parameter $-1 \le \phi \le 1$.

In this paper we consider the case of negligible interface kinetics, i.e., $\beta(\boldsymbol{n}) = 0$, particular relevant for solidification at low undercoolings in metallic systems. Consequently, only the capillarity length needs to be obtain from the sharp-interface model

$$d(\boldsymbol{n}) = d_0 a(\boldsymbol{n}), \tag{6}$$

where d_0 stand for the constant capillarity length. A standard fourfold anisotropy function is defined as

$$\begin{aligned} a(\boldsymbol{n}) &= (1-3\epsilon_4)\left(1 + \frac{4\epsilon_4}{1-3\epsilon_4}\left(\tilde{n}_x^4 + \tilde{n}_y^4\right)\right) \\ &= (1-3\epsilon_4)\left(1 + \frac{4\epsilon_4}{1-3\epsilon_4}\left(\sin^4\theta + \cos^4\theta\right)\right), \end{aligned} \tag{7}$$

where ϵ_4 stand for anisotropy strength. Vector $\tilde{\boldsymbol{n}} = (\tilde{n}_x, \tilde{n}_y)$ is defined as

$$\tilde{\boldsymbol{n}} = \boldsymbol{R}(\theta_0)\boldsymbol{n}, \tag{8}$$

where $\boldsymbol{R}(\theta_0)$ is rotation matrix and θ_0 angle, determining preferential growth direction. Combining Eqs. (3) and (6) yields

$$W(\boldsymbol{n}) = W_0 a(\boldsymbol{n}), \quad W_0 = d_0\lambda/a_1, \tag{9}$$

where W_0 is constant interface thickness. Applying condition $\beta(\boldsymbol{n}) = 0$ to Eq. (4) yields

$$\tau(\boldsymbol{n}) = \tau_0 a^2(\boldsymbol{n}), \quad \tau_0 = a_2\lambda W_0^2/\alpha, \tag{10}$$

where τ_0 is constant characteristic time of attachment of atoms at the interface.

It is convenient to rewrite model from Eq. (2) to non-dimensional form by using Eqs. (9) and (10). By rescaling time and space as $\bar{t} = t/\tau_0$, $\bar{x} = x/W_0$ and $\bar{y} = y/W_0$, PF model with zero interface kinetics is rewritten as

$$\begin{aligned} a^2(\boldsymbol{n})\partial_{\bar{t}}\phi = -g'(\phi) - \lambda u p'(\phi) + \overline{\nabla}\cdot\left(a^2(\boldsymbol{n})\overline{\nabla}\phi\right) + \\ + \sum_{\bar{\xi}=\bar{x},\bar{y}} \partial_{\bar{\xi}}\left(|\overline{\nabla}\phi|^2 a(\boldsymbol{n})\frac{\partial a(\boldsymbol{n})}{\partial(\partial_{\bar{\xi}}\phi)}\right), \end{aligned} \tag{11}$$

$$\partial_{\bar{t}} u = \bar{D}\overline{\nabla}^2 u + h'(\phi)\partial_{\bar{t}}\phi, \tag{12}$$

where and and $\bar{D} = \alpha\tau_0/W_0^2$.

2.4. Initial and boundary conditions

The system of equations from Eqs. (11) and (12) is solved in the computational domain Ω with boundary Γ. Initial conditions at $\boldsymbol{r} = (\bar{x}, \bar{y}) \in \Omega + \Gamma$ are given as

$$u(\boldsymbol{r}, \bar{t} = 0) = -\Delta, \tag{13}$$

where Δ stands for the initial dimensionless undercooling, and

$$\phi(\boldsymbol{r}, \bar{t} = 0) = -\tanh\left(\frac{|\boldsymbol{r} - \boldsymbol{r}_0|^2 - R_0^2}{\sqrt{2}}\right), \tag{14}$$

where $\boldsymbol{r}_0$ stands for the center of the solid nuclei with the radius R_0. Zero flux boundary condition are used for both fields at $\boldsymbol{r} \in \Gamma$

$$\frac{\partial u(\boldsymbol{r}, \bar{t})}{\partial n_\Gamma} = 0, \quad \frac{\partial \phi(\boldsymbol{r}, \bar{t})}{\partial n_\Gamma} = 0, \tag{15}$$

where n_Γ stands for the normal to the Γ.

3. Numerical methods

Governing equations from Section 2 require temporal and spatial discretization, presented in Sections 3.1 and 3.2, respectively.

3.1. Explicit Euler scheme

Simple explicit Euler scheme is used for time-marching of Eqs. (11) and (12). The partial derivative $\partial_{\bar{t}}\eta$ between two discrete times $\bar{t}_0$ and $\bar{t}_0 + \Delta\bar{t}$ is approximated as

$$\partial_{\bar{t}}\eta \approx \frac{\eta^{\bar{t}_0+\Delta\bar{t}} - \eta^{\bar{t}_0}}{\Delta\bar{t}}, \tag{16}$$

where $\eta = \phi$ or $\eta = u$ and $\Delta\bar{t}$ stand for the explicit time step. Linear stability analysis yields following stability criterion for the finite difference spatial discretization in 2D [5]

$$\Delta\bar{t} < \Delta\bar{t}_0 = \frac{1}{4}\frac{h^2}{\max(\bar{D}, 1/a(\boldsymbol{n}))}, \tag{17}$$

where h and $\Delta\bar{t}_0$ stand for the distance between two neighbouring computational points and critical time step, respectively. It turns out, that criterion from Eq. (17) can be also applied in the case, when LRBFCM is used for spatial discretization, however, formal linear stability analysis by using LRBFCM has not been performed yet.

3.2. Local radial basis function collocation method - LRBFCM

In this work LRBFCM is used for spatial discretization of PF equations. LRBFCM is finite-difference-like, i.e., the spatial differential operator of the field value in a computational point is approximated by the sum of the weighted field values from the local sub-domain. In the spatial discretization of Eqs. (11) and (12) only differential operators on the scalar fields have to be evaluated.

3.2.1. Local interpolation problem

For each ${}_l\boldsymbol{r} \in \Omega+\Gamma$, $l = 1, ..., N$, where N is number of points in $\Omega+\Gamma$, a local sub-domain ${}_l\Omega$, containing point ${}_l\boldsymbol{r}$ and its ${}_lN-1$ nearest points, is generated, as schematically shown in Fig. 1. Each sub-domain consists of ${}_lN = {}_lN_\Omega + {}_lN_\Gamma$ points, where ${}_lN_\Omega$ and ${}_lN_\Gamma$ stand for number of points in ${}_l\Omega$ from Ω and Γ, respectively. Number ${}_lN_\Gamma^{max}$, the maximum allowed value of ${}_lN_\Gamma$ in ${}_l\Omega$, has to be determined, when ${}_l\Omega$ is generated, since ${}_lN_\Gamma$ and ${}_lN$ crucially determine the stability and accuracy of LRBFCM.

LRBFCM is based on the interpolation of the field value over a local sub-domain by using multiquadric (MQ) radial basis function

$$ {}_l\Phi_i(\boldsymbol{r}) = \sqrt{\frac{{}_l\epsilon^2}{{}_lh^2}|\boldsymbol{r} - {}_l\boldsymbol{r}_i|^2 + 1}, \tag{18} $$

where ${}_l\Phi_i(\boldsymbol{r})$ and ${}_l\epsilon$ stand for MQ centered at ${}_l\boldsymbol{r}_i \in {}_l\Omega$, $i = 1, ..., {}_lN$, ${}_l\boldsymbol{r}_1 = {}_l\boldsymbol{r}$, and shape parameter, respectively. ${}_lh$ is the size of ${}_l\Omega$, defined as

$$ {}_lh = \sqrt{\sum_{i=2}^{{}_lN-1} \frac{|{}_l\boldsymbol{r}_i - {}_l\boldsymbol{r}|^2}{{}_lN-1}}. \tag{19} $$

The interpolation problem is augmented with m monomials $p_i(\boldsymbol{r})$, $i = 1, ..., m$, since only the use of MQs might result in ill-conditional problem. The arbitrary scalar field $\eta(\boldsymbol{r})$ is approximated as

$$ \begin{aligned} \eta(\boldsymbol{r}) &\approx \sum_{i=1}^{{}_lN} {}_l\alpha_i\, {}_l\Phi_i(\boldsymbol{r}) + \sum_{i=1}^{m} {}_l\alpha_{{}_lN+i} p_i(\boldsymbol{r}) = \\ &= \sum_{i=1}^{{}_lN+m} {}_l\alpha_i \Psi_i(\boldsymbol{r}), \end{aligned} \tag{20} $$

where the center of domain ${}_l\boldsymbol{r}$ is closest to $\boldsymbol{r}$. ${}_l\alpha_i$, $i = 1, ..., {}_lN + m$ are the coefficients, calculated by the interpolation of field values $\eta({}_l\boldsymbol{r}_j)$, $j = 1, ..., {}_lN$, while the function Ψ_i is either MQ or a monomial. The linear boundary condition $\mathcal{B}$ is applied to Eq. (20) if $\boldsymbol{r} \in \Gamma$, i.e., $\mathcal{B}\eta(\boldsymbol{r}) = b(\boldsymbol{r})$, where $b(\boldsymbol{r})$ is the right-hand side of boundary condition. The interpolation problem can be written in matrix form as

$$ \sum_{i=1}^{{}_lN+m} {}_lA_{ji}\, {}_l\alpha_i = {}_l\gamma_j, \tag{21} $$

where

$$ {}_lA_{ji} = \begin{cases} \Psi_i({}_l\boldsymbol{r}_j) & \text{if } {}_l\boldsymbol{r}_j \in \Omega \\ \mathcal{B}({}_l\boldsymbol{r}_j)\Psi_i({}_l\boldsymbol{r}_j) & \text{if } {}_l\boldsymbol{r}_j \in \Gamma \\ p_j({}_l\boldsymbol{r}_i) & \text{if } j > {}_lN \text{ and } i \le {}_lN \\ 0 & \text{otherwise} \end{cases}, \tag{22} $$

and

$$ {}_l\gamma_j = \begin{cases} \eta({}_l\boldsymbol{r}_j) & \text{if } {}_l\boldsymbol{r}_j \in \Omega \\ b({}_l\boldsymbol{r}_j) & \text{if } {}_l\boldsymbol{r}_j \in \Gamma \\ 0 & \text{otherwise} \end{cases}. \tag{23} $$

The value of shape parameter ${}_l\epsilon$ has a large impact on the accuracy and stability of the radial basis function methods [44]. In this work ${}_l\epsilon$ in each ${}_l\Omega$ is calculated according to the value of condition number c_{num} of matrix ${}_l\boldsymbol{A}$ from Eq. (22)

$$ c_{num} = \frac{\Sigma_{max}}{\Sigma_{min}}, \tag{24} $$

where Σ_{max} and Σ_{min} stand for maximum and minimum singular value of the matrix ${}_l\boldsymbol{A}$. ${}_l\epsilon$ is set according to the targeted condition number $c_{num}^{target} = 10^{20}$ by using quadruple precision.

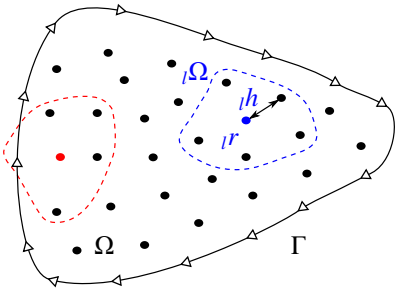

Figure 1: Scheme of domain Ω and boundary Γ. Filled circles and empty triangles represent the interior and boundary points, respectively. Blue and red dashed lines represent the boundaries of sub-domains, centered at the points denoted with blue and red color, respectively. Blue domain is example of sub-domain containing only interior points, while red domain contains a boundary point.

3.2.2. Evaluation of differential operators

The MQ approximation from Eq. (20) is used for evaluation of any linear differential operator $\mathcal{D}$ applying on a scalar field $\eta(\boldsymbol{r})$ in $\boldsymbol{r} \in \Omega + \Gamma$, while the boundary condition in $\boldsymbol{r} \in \Gamma$ is analytically satisfied in interpolation problem from Eqs.(21), (22) and (23). Applying $\mathcal{D}$ on Eq. (20) yields

$$ \mathcal{D}\eta(\boldsymbol{r}) \approx \sum_{i=1}^{{}_lN+m} {}_l\alpha_i \mathcal{D}\Psi_i(\boldsymbol{r}), \tag{25} $$

since ${}_l\alpha_i$ are constants. By calculating the inverse of matrix ${}_l\boldsymbol{A}^{-1}$ from Eq. (22), Eq. (25) in ${}_l\boldsymbol{r}$ can be rewritten as

$$\mathcal{D}\eta({}_l\boldsymbol{r}) \approx \sum_{k=1}^{{}_lN+m} {}_l\gamma_k \sum_{i=1}^{{}_lN+m} {}_lA^{-1}_{ik}\mathcal{D}\Psi_i({}_l\boldsymbol{r}). \tag{26}$$

Eq. (26) can be written in standard finite-difference manner as

$$\mathcal{D}\eta({}_l\boldsymbol{r}) = \sum_{k=1}^{{}_lN} {}_l\gamma_k\, {}_lw_k, \tag{27}$$

where ${}_lw_k$ are finite-difference-like coefficients, defined as

$${}_lw_k = \sum_{i=1}^{{}_lN+m} {}_lA^{-1}_{ik}\mathcal{D}\Psi_i({}_l\boldsymbol{r}). \tag{28}$$

Summation in Eq. (27) goes from $k = 1$ to $k = {}_lN$, since ${}_l\gamma_k = 0$ for $k > {}_lN$.

4. Numerical results

Numerical simulations are performed on a regular distribution of $N = M \times M$ computational points where local subdomains are determined by values ${}_lN = 6$ and ${}_lN_\Gamma^{max} = 2$. Non-dimensional spacing is set to $h = 0.3$ in all cases except in Fig. 6, where the spatial convergence of LRBFCM is verified. M is set to $M = 400$ in Figs. 2, 3 and 4, to $M = 500$ in Fig. 5, while different values of M are used in Fig. 6 according to the limitation $hM = const$. The center of initial circular nuclei with radius $R_i = 10h$ and preferential growth direction angle, respectively, are set to $\mathbf{r}_0 = (0, 0)$ and $\theta_0 = 0$ in the cases from Figs. 2, 3, 4 and 6, while $\mathbf{r}_0 = (M/2h, M/2h)$ is used in Fig. 5, where the dendritic morphology at three different values of θ_0 is studied. Time is discretized as $\bar{t} = n\Delta\bar{t}$, where n is the iteration number.

The spatial and temporal coordinates are scaled with $W_0 = 1$ and $\tau_0 = 1$, leaving $\bar{D}$ as only free parameter in the thin interface limit of PF model [24]. Parameters $\bar{D} = 6.267$, $\epsilon_4 = 0.06$ and $\Delta = 0.55$ are used in all cases except in Fig. 6, where the spatial convergence of LRBFCM is verified and parameters $\bar{D} = 1$, $\epsilon_4 = 0.05$ and $\Delta = 0.65$ are used. One can see in Fig. 2 how phase field is equal to $\phi = 1$ and $\phi = -1$, respectively, in the solid and liquid phase, while the solid-liquid interface is determined by the contour $\phi = 0$. The temporal evolution of the solid-liquid interface is shown in Fig. 4. The initial circular shape of nuclei eventually becomes unstable due to the anisotropic interface energy, yielding the evolution of dendrite. The dendrite tip velocity decreases with time and approaches the steady state solution as seen in Fig. 6. The velocity is rescaled as $\bar{V}_{tip} = V_{tip}d_0/\alpha$ in order to obtain numerical solution independent of PF parameters [24]. The analytical steady state solution $\bar{V}_{tip}^{Green}$ is obtained by the Green function method [45]. The numerical growth velocity is calculated at different values of h in order to assess the spatial convergence of LRBFCM. A very good agreement between analytical and numerical solution is observed at $h = 0.4$, where the relative error is equal to $\Delta\bar{V}_{tip}/\bar{V}_{tip} \approx 1\%$. The solid-liquid interface at different values of the preferential growth direction, determined by θ_0, is shown in Fig. 5, where one can see, how the dendrite morphology is independent of θ_0.

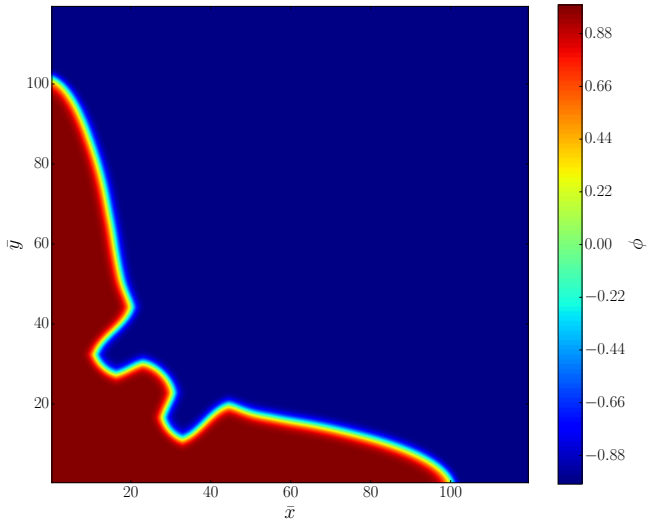

Figure 2: Phase field after 40000 time steps at the initial non-dimensional undercooling $\Delta = 0.65$ and the strength of anisotropy $\epsilon_4 = 0.06$.

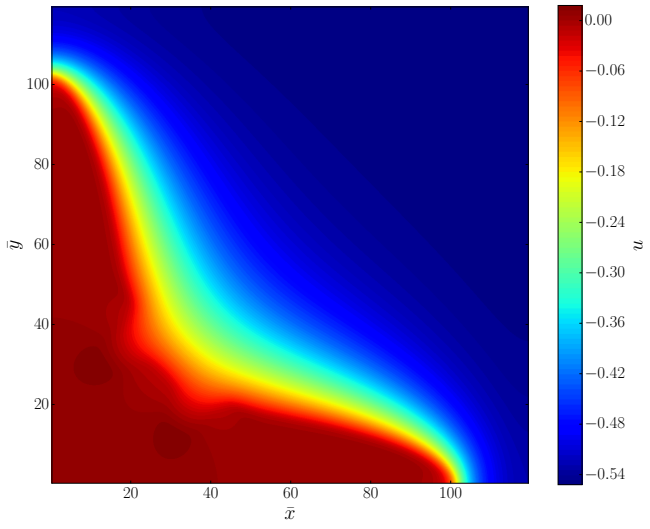

Figure 3: Temperature field after 40000 time steps at the initial non-dimensional undercooling $\Delta = 0.65$ and the strength of anisotropy $\epsilon_4 = 0.06$.

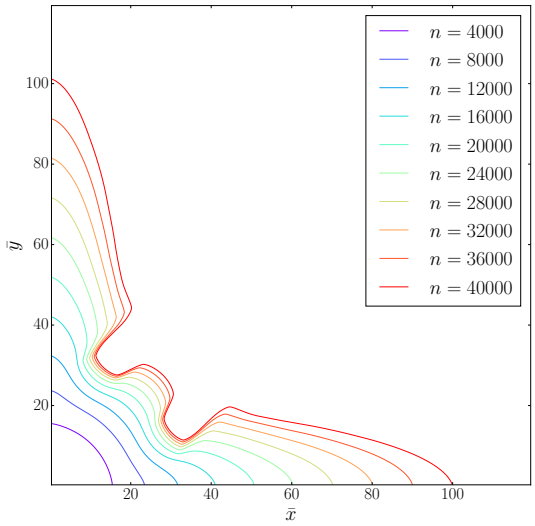

Figure 4: Solid-liquid interface evolution shown every 4000 iterations at the initial non-dimensional undercooling $\Delta = 0.65$ and the strength of anisotropy $\epsilon_4 = 0.06$.

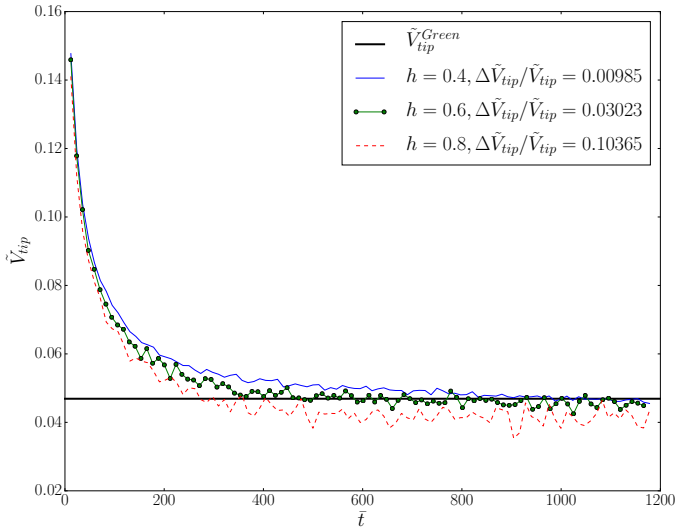

Figure 6: Rescaled non-dimensional tip velocity as a function of time at three different values of the spacing h. The black horizontal line corresponds to the velocity obtained by the Green function method at the non-dimensional undercooling far from the tip $\Delta = 0.65$ and the strength of anisotropy $\epsilon_4 = 0.06$. In the legend, the relative difference between numerically and analytically calculated tip velocity at each value of h is given.

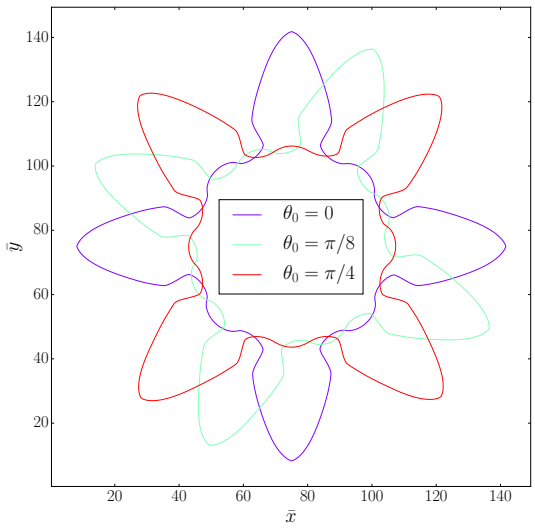

Figure 5: Solid-liquid interface after 25000 time steps at three different preferential growth directions θ_0, the initial non-dimensional undercooling $\Delta = 0.65$, and the strength of anisotropy $\epsilon_4 = 0.06$.

5. Conclusions

A two dimensional meshless PF model for the simulation of dendritic growth from a pure melt has been developed. Meshless solver is capable of solving highly non-linear PF equations and obtaining accurate results, comparable with the analytical steady state solution of dendritic growth. Also, dendritic morphology is independent of the preferential growth direction.

In the further work, the random noise will be firstly added to PF equations in order to analyze the evolution of the secondary dendrite arms. Also, the dendritic growth in binary and multicomponent alloys will be considered. An h-adaptive framework will be developed in order to assure high density of computational points only in the regions where the phase field varies. That way, computationally efficient and accurate results will be assured.

References

[1] J. Dantzig, M. Rappaz, Solidification, Engineering sciences, EFPL Press, 2009.
URL https://books.google.si/books?id=bl-5L7cL0zAC

[2] M. E. Glicksman, Principles of Solidification, Springer New York, New York, NY, 2011.
URL http://link.springer.com/10.1007/978-1-4419-7344-3

[3] W. Kurz, D. J. Fisher, Fundamentals of Solidification, 4th Edition, CRC Press, Uetikon-Zuerich, Switzerland ; Enfield, N.H, 1998.

[4] J. Campbell, Castings, Elsevier Science, 2003.
URL https://books.google.si/books?id=8yqaLGr-bIgC

[5] N. Provatas, K. Elder, Phase-Field Methods in Materials Science and Engineering, 1st Edition, Wiley-VCH, 2010.

[6] L.-Q. Chen, Phase-Field Models for Microstructure Evolution, Annual Review of Materials Research 32 (1) (2002) 113–140. doi:10.1146/annurev.matsci.32.112001.132041.
URL https://doi.org/10.1146/annurev.matsci.32.112001.132041

[7] W. J. Boettinger, J. A. Warren, C. Beckermann, A. Karma, Phase-Field Simulation of Solidification, Annual Review of Materials Research 32 (1) (2002) 163–194. doi:10.1146/annurev.matsci.32.101901.155803.
URL http://www.annualreviews.org/doi/10.1146/annurev.matsci.32.101901.155803

[8] G. J. Fix, Phase field methods for free boundary problems.

[9] J. B. Collins, H. Levine, Diffuse interface model of diffusion-limited crystal growth, Physical Review. B, Condensed Matter 31 (9) (1985) 6119–6122.

[10] J. S. Langer, Models of Pattern Formation in First-Order Phase Transitions, Directions In Condensed Matter Physics. Series: Series on Directions in Condensed Matter Physics, ISBN: 978-9971-978-42-6. WORLD SCIENTIFIC, Edited by G Grinstein and G Mazenko, vol. 1, pp. 165-186 1 (1986) 165–186. doi:10.1142/9789814415309_0005.
URL http://adsabs.harvard.edu/abs/1986SDCMP...1..165L

[11] J. D. Van der Waals, JD van der Waals, Verh.-K. Ned. Akad. Wet, Afd. Natuurkd., Eerste Reeks 1, 56 (1893)., Verh.-K. Ned. Akad. Wet., Afd. Natuurkd., Eerste Reeks 1 (1893) 56.

[12] J. S. Rowlinson, Translation of J. D. van der Waals' "The thermodynamik theory of capillarity under the hypothesis of a continuous variation of density", Journal of Statistical Physics 20 (2) (1979) 197–200. doi:10.1007/BF01011513.
URL https://link.springer.com/article/10.1007/BF01011513

[13] D. T. Haar, Collected Papers of L.D. Landau, Elsevier, 2013, google-Books-ID: epc4BQAAQBAJ.

[14] J. W. Cahn, J. E. Hilliard, Free Energy of a Nonuniform System. I. Interfacial Free Energy, The Journal of Chemical Physics 28 (2) (1958) 258–267. doi:10.1063/1.1744102.
URL https://aip.scitation.org/doi/10.1063/1.1744102

[15] J. W. Cahn, On spinodal decomposition, Acta Metallurgica 9 (9) (1961) 795–801. doi:10.1016/0001-6160(61)90182-1.
URL http://www.sciencedirect.com/science/article/pii/0001616061901821

[16] J. Cahn, S. Allen, A microscopic theory for domain wall motion and its experimental verification in Fe-Al alloy domain growth kinetics, Journal de Physique Colloques 38 (C7) (1977) C7–51–C7–54. doi:10.1051/jphyscol:1977709.
URL https://hal.archives-ouvertes.fr/jpa-00217210

[17] P. C. Hohenberg, B. I. Halperin, Theory of dynamic critical phenomena, Reviews of Modern Physics 49 (3) (1977) 435–479. doi:10.1103/RevModPhys.49.435.
URL https://link.aps.org/doi/10.1103/RevModPhys.49.435

[18] R. Kobayashi, Modeling and numerical simulations of dendritic crystal growth, Physica D: Nonlinear Phenomena 63 (3) (1993) 410–423. doi:10.1016/0167-2789(93)90120-P.
URL http://www.sciencedirect.com/science/article/pii/016727899390120P

[19] A. A. Wheeler, B. T. Murray, R. J. Schaefer, Computation of dendrites using a phase field model, Physica D: Nonlinear Phenomena 66 (1) (1993) 243–262. doi:10.1016/0167-2789(93)90242-S.
URL http://www.sciencedirect.com/science/article/pii/016727899390242S

[20] S. L. Wang, R. F. Sekerka, Computation of the dendritic operating state at large supercoolings by the phase field model, Physical Review. E, Statistical Physics, Plasmas, Fluids, and Related Interdisciplinary Topics 53 (4) (1996) 3760–3776.

[21] G. B. McFadden, A. A. Wheeler, R. J. Braun, S. R. Coriell, R. F. Sekerka, Phase-field models for anisotropic interfaces, Physical Review E 48 (3) (1993) 2016–2024. doi:10.1103/PhysRevE.48.2016.
URL https://link.aps.org/doi/10.1103/PhysRevE.48.2016

[22] S. L. Wang, R. F. Sekerka, A. A. Wheeler, B. T. Murray, S. R. Coriell, R. J. Braun, G. B. McFadden, Thermodynamically-consistent phase-field models for solidification, Physica D: Nonlinear Phenomena 69 (1) (1993) 189–200. doi:10.1016/0167-2789(93)90189-8.
URL http://www.sciencedirect.com/science/article/pii/0167278993901898

[23] A. Karma, W. J. Rappel, Phase-field method for computationally efficient modeling of solidification with arbitrary interface kinetics, Physical Review. E, Statistical Physics, Plasmas, Fluids, and Related Interdisciplinary Topics 53 (4) (1996) R3017–R3020.

[24] A. Karma, W.-J. Rappel, Quantitative phase-field modeling of dendritic growth in two and three dimensions, Physical review E 57 (4) (1998) 4323.
URL http://journals.aps.org/pre/abstract/10.1103/PhysRevE.57.4323

[25] A. Karma, D. Tourret, Atomistic to continuum modeling of solidification microstructures, Current Opinion in Solid State and Materials Science 20 (1) (2016) 25–36. doi:10.1016/j.cossms.2015.09.001.
URL http://www.sciencedirect.com/science/article/pii/S1359028615300061

[26] X.-l. Dong, H. Xing, K.-r. Weng, H.-l. Zhao, Current development in quantitative phase-field modeling of solidification, Journal of Iron and Steel Research, International 24 (9) (2017) 865–878. doi:10.1016/S1006-706X(17)30129-2.
URL http://www.sciencedirect.com/science/article/pii/S1006706X17301292

[27] N. Provatas, N. Goldenfeld, J. Dantzig, Efficient Computation of Dendritic Microstructures Using Adaptive Mesh Refinement, Physical Review Letters 80 (15) (1998) 3308–3311. doi:10.1103/PhysRevLett.80.3308.
URL https://link.aps.org/doi/10.1103/PhysRevLett.80.3308

[28] T. Shimokawabe, T. Aoki, T. Takaki, T. Endo, A. Yamanaka, N. Maruyama, A. Nukada, S. Matsuoka, Peta-scale Phase-field Simulation for Dendritic Solidification on the TSUBAME 2.0 Supercomputer, in: Proceedings of 2011 International Conference for High Performance Computing, Networking, Storage and Analysis, SC '11, ACM, New York, NY, USA, 2011, pp. 3:1–3:11. doi:10.1145/2063384.2063388.
URL http://doi.acm.org/10.1145/2063384.2063388

[29] M. Plapp, A. Karma, Multiscale Random-Walk Algorithm for Simulating Interfacial Pattern Formation, Physical Review Letters 84 (8) (2000) 1740–1743. doi:10.1103/PhysRevLett.84.1740.
URL https://link.aps.org/doi/10.1103/PhysRevLett.84.1740

[30] Z. Guo, J. Mi, P. S. Grant, Phase field simulation of multi-dendrite growth in a coupled thermal-solute-convective environment, IOP Conference Series: Materials Science and Engineering 33 (1) (2012) 012101. doi:10.1088/1757-899X/33/1/012101.
URL http://stacks.iop.org/1757-899X/33/i=1/a=012101

[31] P. C. Bollada, C. E. Goodyer, P. K. Jimack, A. M. Mullis, F. W. Yang, Three dimensional thermal-solute phase field simulation of binary alloy solidification, Journal of Computational Physics 287 (2015) 130–150. doi:10.1016/j.jcp.2015.01.040.
URL http://www.sciencedirect.com/science/article/pii/S0021999115000546

[32] M. Berghoff, M. Selzer, A. Choudhury, B. Nestler, Efficient techniques for bridging from atomic to mesoscopic scale in phase-field simulations, Journal of Computational Methods in Sciences and Engineering 13 (5-6). doi:10.3233/JCM-130476.
URL https://publikationen.bibliothek.kit.edu/1000041072

[33] B. Šarler, R. Vertnik, Meshfree explicit local radial basis function collocation method for diffusion problems, Computers & Mathematics with Applications 51 (8) (2006) 1269–1282. doi:10.1016/j.camwa.2006.04.013.
URL http://www.sciencedirect.com/science/article/pii/S0898122106000836

[34] A. I. Tolstykh, D. A. Shirobokov, On using radial basis functions in a "finite difference mode" with applications to elasticity problems, Computational Mechanics 33 (1) (2003) 68–79. doi:10.1007/s00466-003-0501-9.
URL https://link.springer.com/article/10.1007/s00466-003-0501-9

[35] C. K. Lee, X. Liu, S. C. Fan, Local multiquadric approximation for solving boundary value problems, Computational Mechanics 30 (5-6) (2003) 396–409. doi:10.1007/s00466-003-0416-5.
URL https://link.springer.com/article/10.1007/s00466-003-0416-5

[36] X. Liu, G. R. Liu, K. Tai, K. Y. Lam, Radial basis point interpolation collocation method for 2-d solid problem, in: Advances in Meshfree and X-FEM Methods, WORLD SCIENTIFIC, 2002, pp. 35–40. doi:10.1142/9789812778611_0008.
URL https://www.worldscientific.com/doi/abs/10.1142/9789812778611_0008

[37] R. Vertnik, B. Šarler, Local Collocation Approach for Solving Turbulent Combined Forced and Natural Convection Problems, Advances in Applied Mathematics and Mechanics 3 (3) (2011) 259–279. doi:10.4208/aamm.10-10s2-01.
URL https://www.cambridge.org/core/journals/advances-in-applied-mathematics-and-mechanics/article/local-collocation-approach-for-solving-turbulent-combined-forced-and-natural-convection-problems/F849EE2024F38919C76E5DA2786A687F

[38] K. Mramor, R. Vertnik, B. Šarler, Simulation of laminar backward facing step flow under magnetic field with explicit local radial basis function collocation method, Engineering Analysis with Boundary Elements 49 (2014) 37–47. doi:10.1016/j.enganabound.2014.04.013.
URL http://www.sciencedirect.com/science/article/pii/S0955799714000903

[39] G. Kosec, B. Šarler, Simulation of macrosegregation with mesosegregates in binary metallic casts by a meshless method, Engineering Analysis with Boundary Elements 45 (2014) 36–44. doi:10.1016/j.enganabound.2014.01.016.
URL http://www.sciencedirect.com/science/article/pii/S0955799714000290

[40] B. Mavrič, B. Šarler, Local radial basis function collocation method for linear thermoelasticity in two dimensions, International Journal of Numerical Methods for Heat & Fluid Flow 25 (6) (2015) 1488–1510. doi:10.1108/HFF-11-2014-0359.
URL https://www.emeraldinsight.com/doi/full/10.1108/HFF-11-2014-0359

[41] B. Mavrič, B. Šarler, Application of the RBF collocation method to transient coupled thermoelasticity, International Journal of Numerical Methods for Heat & Fluid Flow 27 (5) (2017) 1064–1077. doi:10.1108/HFF-03-2016-0110.
URL https://www.emeraldinsight.com/doi/abs/10.1108/HFF-03-2016-0110

[42] U. Hanoglu, B. Šarler, Multi-pass hot-rolling simulation using a meshless method, Computers & Structures 194 (2018) 1–14. doi:10.1016/j.compstruc.2017.08.012.
URL http://www.sciencedirect.com/science/article/pii/S004579491730038X

[43] V. P. Nguyen, T. Rabczuk, S. Bordas, M. Duflot, Meshless methods: A review and computer implementation aspects, Mathematics and Computers in Simulation 79 (3) (2008) 763–813. doi:10.1016/j.matcom.2008.01.003.
URL http://www.sciencedirect.com/science/article/pii/S0378475408000062

[44] X.-Y. Liu, A. Karageorghis, C. S. Chen, A Kansa-Radial Basis Function Method for Elliptic Boundary Value Problems in Annular Domains, Journal of Scientific Computing 65 (3) (2015) 1240–1269. doi:10.1007/s10915-015-0009-4.
URL https://link.springer.com/article/10.1007/s10915-015-0009-4

[45] D. I. Meiron, Selection of steady states in the two-dimensional symmetric model of dendritic growth, Physical Review A 33 (4) (1986) 2704–2715. doi:10.1103/PhysRevA.33.2704.
URL https://link.aps.org/doi/10.1103/PhysRevA.33.2704

Morphological characterization and chemical instability of the interface between Ag and Bi_2Se_3 topological insulator

Katja Ferfolja

University of Nova Gorica, Vipavska 13, SI-5000 Nova Gorica

Abstract

Understanding an interaction at an interface between a topological insulator and a metal is very important when designing electronic and spintronic devices or when such systems are used in catalysis. In this paper, we report on a chemical instability of the interface between Bi_2Se_3 and Ag. We present experimental evidence of a solid-state reaction occurring at the interface yielding Ag_2Se, $AgBiSe_2$ and Bi phase. The unexpected room-temperature chemical instability of the interface should be considered for all future theoretical and applicative studies involving the interface between Bi_2Se_3 and Ag.

Keywords: topological insulator, Bi_2Se_3, interface, Ag, redox reaction

1. Introduction

Topological insulators (TI) have been a subject of many studies during the past two decades due to their attractive electronic properties. The TI represent a new state of matter with a finite band gap in the bulk and gapless states at the boundaries (edges, surface)[1,2]. These topological surface states (TSS) cross the Fermi level and are linearly dispersed in a shape of a Dirac cone. The TSS are a result of a non-trivial topology of the bulk band structure usually caused by spin orbit coupling. Due to their origin, they are necessarily present at the surface of the solid unless a change in the bulk topology occurs. This makes them much more robust towards impurities and imperfections at the surface compared to ordinary surface

Email address: katja.ferfolja@ung.si (Katja Ferfolja)

states that are easily destroyed by contamination. Additionally, the TSS are also spin polarized meaning that an electron spin is locked to a crystal momentum, and therefore backscattering is suppressed. The described properties make the TI interesting for development of spintronic devices and quantum computing [3]. In majority of these technologies, quality of an interface between the TI and a metal is a relevant parameter. In addition, different metals, including Ag, have being deposited on TI catalytic substrates in order to improve the catalytic activity [4-6] or field emission properties [7]. For such use, it is important to know whether the deposited metal will remain stable in its metallic form.

Bi_2Se_3 belongs to a group of 3-dimensional TI along with Bi_2Te_3 and Sb_2Te_3 [8]. It is a well-known semiconductor with a narrow band gap of 0.3 eV and a single Dirac cone at the Γ point of the Brillouin zone. Bi_2Se_3 is a layered chalcogenide that crystallizes in a rhombohedral crystal structure and consists of quintuple layers (QL) arranged along the z-axis. Each QL is composed of five covalently bonded atomic layers of Bi and Se atoms. Van der Waals interactions are present between QL. A distance between the QL is 2.43 Å, which is wide enough to host intercalated metal atoms.

Some theoretical papers, involving the metal/TI systems, [9-14] have recently been published, while experimental studies are very rare. Mostly, they focus on systems with low coverage on a TI surface [15,16]. Only recently, Walsh et al. [17] has published first systematic research on Au, Pd, Ir and some transition metals interfaced with Bi_2Se_3. All deposited metal thin films, except Au, resulted in significant interaction with Bi_2Se_3 and produced an interfacial layer consisting of metal selenides (M_xSe_y), metallic Bi or intermetallic alloys ($M_xBi_ySe_z$).

So far, no articles have reported experimental studies on Ag, deposited on a Bi_2Se_3 single crystal. In a theoretical work by Xiao et al., [14] where a focus was on catalytic properties of metal clusters on Bi_2Se_3, Ag was modeled as stable clusters consisting of 7 atoms. In the work of Chang et al., [11] which focused on a new type of Rashba splitting at the metal/TI interface, Ag was modeled as an epitaxial overlayer. However, no experimental evidence of what happens when Ag is deposited on Bi_2Se_3 has been reported. Therefore, it remains unclear whether the modeled clusters and layers can really exist. Another theoretical article by Otrokov et al. [13] predicted a step-mediated intercalation of Ag atoms into the Bi_2Se_3 crystal. According to the article, the Ag atoms are expected to intercalate into the crystal at the steps and not through the QL due to a higher energy barrier for such diffusion.

Two experimental studies that have focused on the interaction of Ag

with Bi_2Se_3 presented contradictory results. While Das et al. [7] claimed that chemically deposited metal Ag cluster are stable on the surface of Bi_2Se_3 nanoflakes, Koski [18] claims that zerovalent Ag intercalates into Bi_2Se_3. A detailed inspection of their experimental data reveals some inconsistency and leaves quite few open questions.For that reason, no conclusive statement about their thermodynamic phase equilibrium can be made.

Here we report on a study of the Ag and Bi_2Se_3 interaction at room temperature. Opposite to the current believe, we show strong experimental evidence for chemical incompatibility of Bi_2Se_3 and metallic Ag. We show that already at room temperature a redox solid-state chemical reaction on the interface between these two phases occurs with significant kinetics. The described diffusion and reaction processes on the interface between Ag and Bi_2Se_3 have to be taken into account when such system is theoretically modeled or considered for applications.

2. Experimental section

All chemicals were used as received without further purification. For the synthesis of the Bi_2Se_3 single crystals the Bridgman method was used. 600 mg of selenium[1] ($\geq$99.999 wt.%) and 220 mg of bismuth[1] ($\geq$99.999 wt.%) were put in a quartz ampoule and sealed in vacuum. The ampoule was placed vertically in an oven at to 860 °C for 24 hours. Afterwards, the temperature was slowly (2 °/h) reduced to 650 °C. The ampoule was kept at this temperature for 7 days and then cooled down to room temperature.

The deposition of Ag on the Bi_2Se_3 single crystal was performed using precision etching coating system[2]. The Bi_2Se_3 crystal was cleaved by tape stripping immediately before insertion in the coating apparatus. After cleaving, the Bi_2Se_3 surface showed large, hundreds of μm, flat regions with a low density of steps. The deposition was performed in vacuum at room temperature and base pressure of 10^{-4} Pa at a rate of 0.08 nm/s for a nominal coverage of 4 and 5 nm and 0.15 nm/s for 10 nm coverage.

The synthesis of Bi_2Se_3 nanoparticles was performed by addition of 160 mg of NaOH[3] (98 wt.%) into 20 ml of ethylene glycol[2] (99 wt.%). The solution was kept at room temperature and stirred for 2 hours until NaOH was completely dissolved. Afterwards, 400 mg of polyvinylpyrrolidone -

[1] Sigma-Aldrich
[2] PECS (Gatan, Model 682) URL:http://www.glteam.com/pdf/682PECS(New).pdf
[3] Alfa Aesar

PVP[4] (M.W. 8.000) was added. The solution was stirred until all PVP dissolved. 233 mg of Bi_2O_3[1] (99.98%) and 119 mg of Se powder[5] (99.5 wt./%) were added to the reaction mixture. After two hours, the reaction mixture was sealed in a Teflon autoclave and put into an oven at 200 °C for 9 hours. When the reaction was completed, the formed solid particles were separated by centrifugation and washed several times with deionized water.

For the synthesis of Ag nanoparticles 600 mg of PVP was dissolved in 30 ml of ethylene glycol and heated to 150 °C. In another beaker, a solution of $AgNO_3$[4] (400 mg; >99.9 wt.%) in 23 ml of ethylene glycol was prepared. The solution of $AgNO_3$ was added drop-wise in the hot solution of PVP. The prepared mixture was stirred for half an hour and left to slowly cool down. The Ag particles were separated from the liquid by centrifugation and washed with water and acetone.

The synthesized products and the progress of the reaction between Ag and Bi_2Se_3 were analysed by an X-ray powder diffractometer[6] with Cu K_α radiation (λ=1,541 Å, 30 kV, 10 mA). A field emission scanning electron microscope[7] equipped with an energy dispersive X-ray spectrometer [8] was used for monitoring evolution of a Ag cluster morphology with time and elemental mappings of the powder mixture after the reaction. Elemental composition was additionally characterized using field emission Transmission Electron Microscope[9] operating in STEM mode using dispersive X-ray spectroscopy[10].

3. Results and discussion

Figure 1a shows a Scanning Electron Microscope (SEM) micrograph of the Bi_2Se_3 surface at the different coverage. At the 4-nm Ag coverage, we can see clusters with a size of a few nm on the flat regions and bigger agglomerates of about 1 μm at the surface steps (Fig. 1b). At the 5-nm nominal coverage, a density of the agglomerates increased (Fig. 1b), while the clusters on the flat parts grew to about 10 nm in diameter. At the 10-nm

[4]Alfa Aesar

[5]Sigma-Aldrich

[6]Rigaku MiniFlex; URL:https://www.rigaku.com/en/products/xrd/miniflex

[7]FESEM, JEOL JSM 7100 TTLS; URL:https://www.jeol.co.jp/en/news/detail/20120130.347.html

[8]EDX, Oxford X-Max80

[9]TEM JEOL JEM 2100UHR;URL:https://www.jeol.co.jp/en/products/detail/JEM-2100.html

[10]EDX, Oxford X-Max80T attached to JEOL JEM 2100UHR

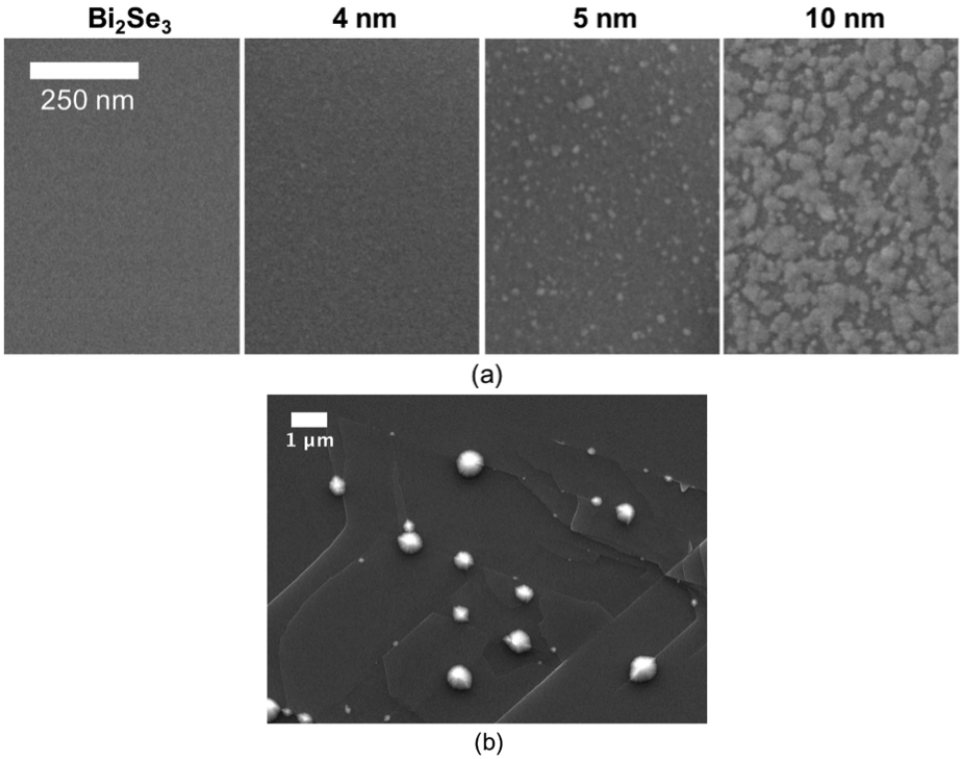

Figure 1: (a) SEM images of a surface of Bi_2Se_3 single crystal without any Ag and with nominal coverage of 4 nm, 5 nm and 10 nm Ag and, (b) Ag agglomerates on the surface steps at 5-nm coverage.

nominal coverage, about a half of the surface was covered with the Ag clusters. The results show that at room temperature the Ag atoms have enough energy to diffuse over the crystal surface and form the clusters and agglomerates. The surface steps represent nucleation sites where the Ag atoms agglomerate.

We have noticed that the morphology of the deposited Ag clusters and agglomerates was changing with time, which indicates on some sort of a diffusion process taking place. Figure 2a shows a Bi_2Se_3 single crystal with the 10-nm nominal Ag coverage immediately after the deposition, 3 days, 8 days and 70 days after the deposition. Immediately after the deposition, the surface was densely covered with the clusters. After eight days, the clusters mostly disappeared and after 70 days they were completely absent and only traces of the biggest agglomerates could be observed. Even

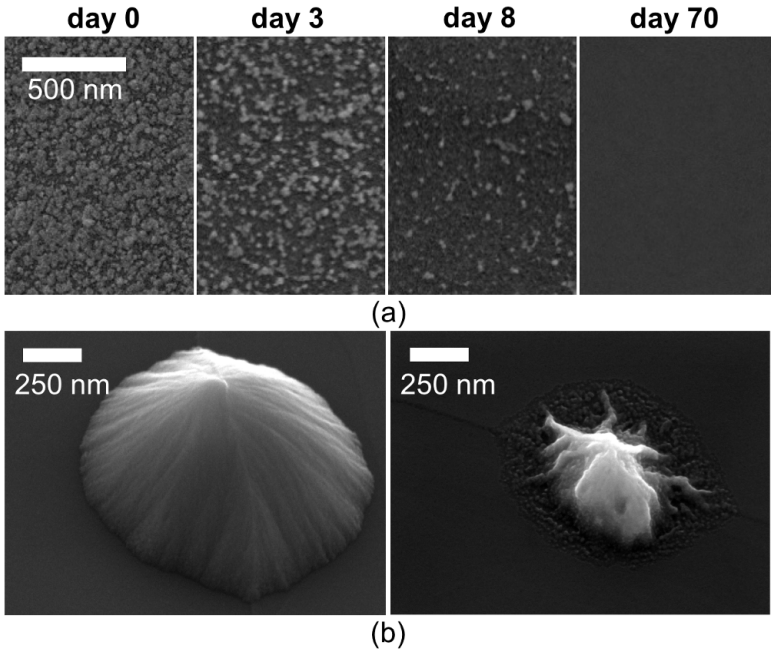

Figure 2: (a) Evolution of surface morphology of Bi_2Se_3 single crystal at 10 nm nominal coverage of Ag and, (b) morphology of big agglomerates immediately after deposition (left), and 3 days after deposition (right).

the morphology of the agglomerates has changed in this time. They have shrunk as shown in Figure 2b. EDX analysis, acquired on flat regions far from the steps and the agglomerates, showed that Ag was present over the whole surface with a signal intensity decreasing with time (Fig. 3). This result suggests that the shrinking of the clusters is due to diffusion of the Ag atoms into the crystal. After 70 days, the decrease in the intensity seems to have stopped at about 90 % of the initial signal, indicating that the diffusion has stopped.

The observed morphological changes show that the Ag and Bi_2Se_3 phases are not thermodynamically stable at room temperature. They indicate on the diffusion of the Ag atom into the Bi_2Se_3 crystal. The question is whether the Ag atoms intercalate into the crystal structure (maintaining the metallic oxidation state) as claimed by Koski et al. [18], form a solid solution or a chemical reaction with formation of new phases takes place. As the occurrence of these chemical processes is determined by thermodynamic phase equilibria and does not depend on a size or morphology of the initial

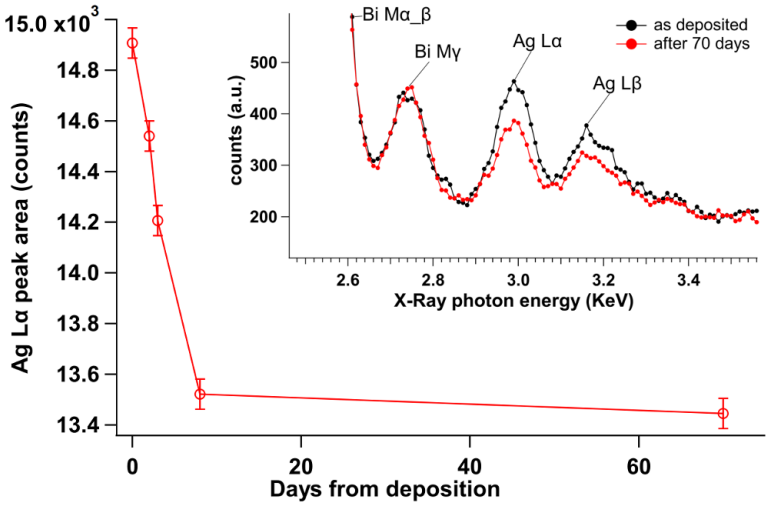

Figure 3: Reduction of the Ag signal intensity in the EDX analysis with time; the inset shows the EDX spectra taken from the Bi_2Se_3 crystal surface with the 10-nm nominal coverage immediately after the deposition and 70 days later.

phases (such as their kinetics), we can study them better in systems where higher interfacial surface area can be realized. For this reason, we carried out an experiment using Bi_2Se_3 and Ag in a form of nanopowders.

The solvothermal synthesis of Bi_2Se_3 yielded hexagonal nanoparticles with a spiral growth mode (Fig. 4), which were approximately 20 nm thick and measured up to 1 μm in diameter. The synthesized Ag powder consisted of 100 nm crystalline nanoparticles. According to the XRD analysis (Fig. 4) the synthesized powders were pure with no traces of secondary phases.

The experiment started with mixing and homogenizing the synthesized powders in a molar ratio Ag : Bi_2Se_3 = 2:1. The phase changes of such system were monitored by XRD. The first XRD analysis was taken right after the mixing. Afterwards, the system has been kept at room temperature and analyzed daily. Figure 5a shows the evolution of the phase composition with time. The XRD pattern at zero time shows diffraction lines at 2θ=30.3°, 33.4° and 34.7° which do not belong to Bi_2Se_3 or Ag phase. This means that the phase change has already occurred during the homogenization process. With time, intensities of these peaks increased, which allowed us to identify the new phases as $AgBiSe_2$ and Ag_2Se.

Undoubtedly, our experiments show that metal Ag and Bi_2Se_3 are not

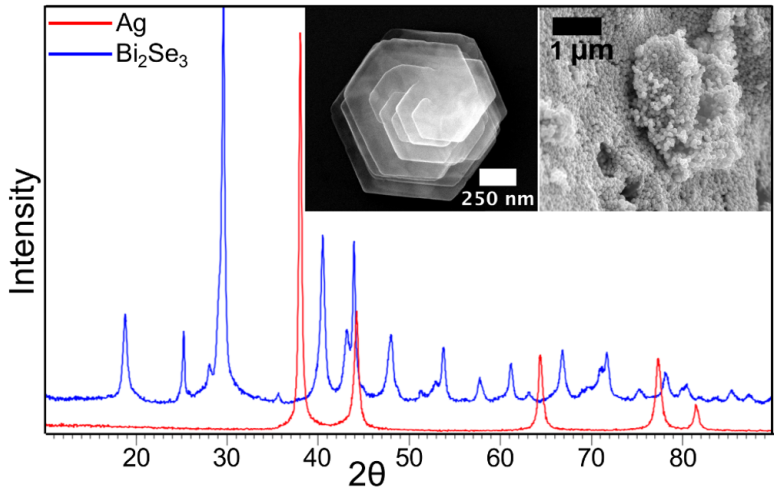

Figure 4: XRD pattern of Bi_2Se_3 nanoparticles (blue) and Ag nanoparticles (red). The diffraction lines fully correspond to 9011965 and 9008459 PDF reference patterns, respectively. The XRD patterns show no traces of secondary phases. The inset shows SEM images of both phases, on the left there is Bi_2Se_3 and on the right there is Ag.

chemically compatible. They chemically react already at room temperature, which is very uncommon for noble metals. Additionally, we tested the interaction during a chemical deposition of Ag in a suspension. This method has been chosen because it is a very common method for deposition of metal nanoclusters on particles (e.g. in catalysis). Ag was introduced into the suspension of the Bi_2Se_3 nanoparticles in ethylene glycol as $AgNO_3$. Ag ions were reduced to metallic Ag by ethylene glycol [19]. The XRD pattern of the resulting dry powder showed no diffraction lines of the metallic Ag (Fig. 5b). Instead, it clearly shows the occurrence of new diffraction patterns that were ascribed to Ag_2Se and $AgBiSe_2$ phases. Interestingly, the XRD analysis, based on the intensity of peaks, suggests that the reaction in suspension yielded two types of Ag_2Se, cubic and orthorhombic.

After the reactions in solid-state and suspension, no change in the position or of the Bi_2Se_3 diffraction lines occurred, which is inconsistent with the claim of Koski et al. [18] If the intercalation would be possible it would expand the unit cell and result in a change, not only in the position of a Bi2Se3 diffraction lines, but also in their profile. In our study, this was not observed.

Figure 6 above shows an EDX mapping of Se, Bi and Ag acquired on

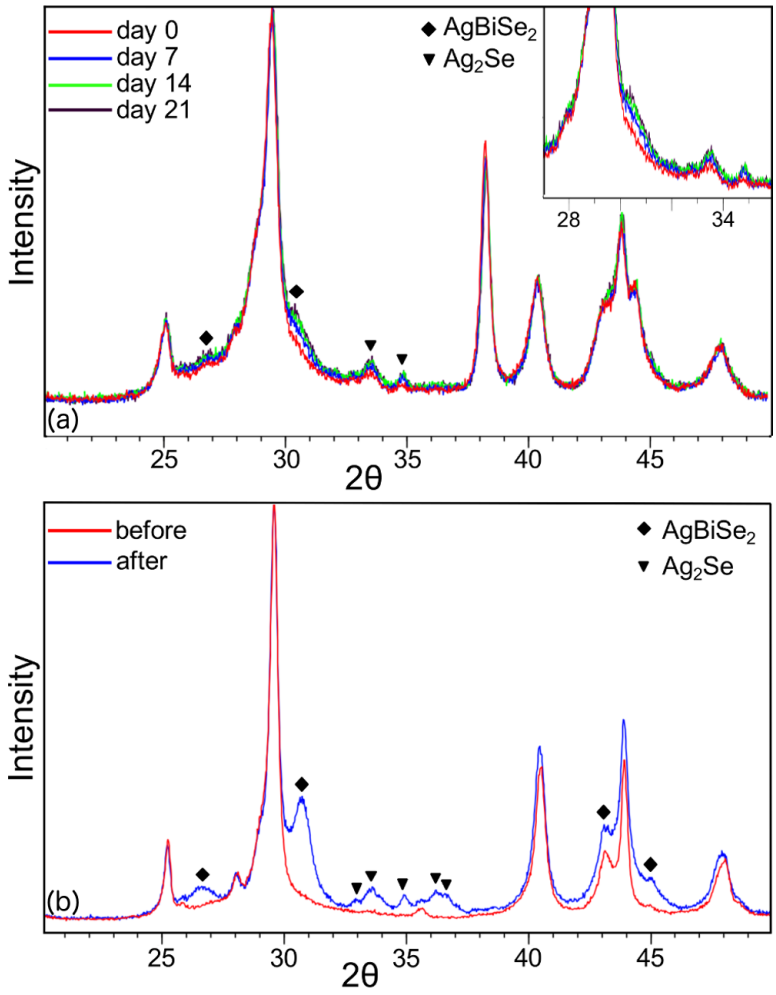

Figure 5: (a) XRD patterns of the phase evolution during a solid-state reaction of Bi_2Se_3 and Ag powders at room temperature with the inset showing a close-up of the area of interest, and (b) pure Bi_2Se_3 (red line) and product after chemical deposition of Ag in suspension (blue line). Peaks assigned with a diamond belong to $AgBiSe_2$ and peaks with triangle belong to Ag_2SeNot assigned peaks belong to Bi_2Se_3.

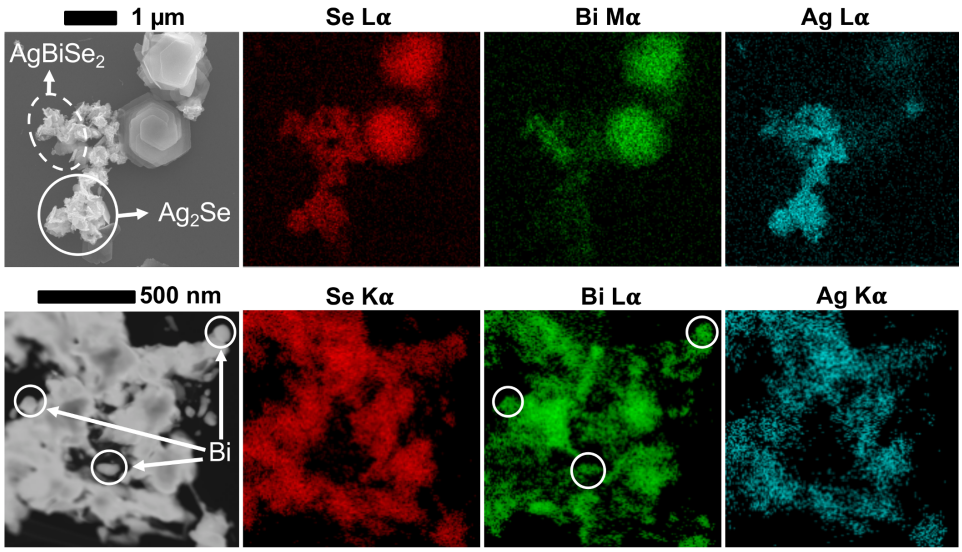

Figure 6: EDX mapping of the product after chemical deposition of Ag onto Bi_2Se_3 nanoparticles showing maps of Se, Bi and Ag made by SEM (above) and TEM (below).Circled areas show product of reaction between Ag and Bi_2Se_3

Bi_2Se_3 nanoparticles after chemical deposition of Ag by SEM. The unreacted Bi_2Se_3 particles can be easily recognized, as they do not contain any Ag. Some particles (see the white solid circle in Fig. 6) show presence of Ag and Se while the signal for Bi is almost negligible. These correspond to the Ag_2Se phase. The SEM image shows that their morphology significantly differs from that of the pristine Bi_2Se_3 nanoparticles. Also, particles of the $AgBiSe_2$ phase that contain all three elements were detected (see the white dashed circle in Fig. 6).

Our study revealed a solid-state redox chemical reaction occurring between Bi_2Se_3 and the noble Ag metal at room temperature, which is a rather unusual process. We propose the following solid-state reaction:

$3\,Ag + Bi_2Se_3 \longrightarrow AgBiSe_2 + Ag_2Se + Bi.$

Bi phase was not detected in the XRD pattern and by EDX on SEM. This could be due to the formation of amorphous phase or alloying with the remaining Ag. Further analysis was performed by Scanning Transmission Electron Microscope (STEM), which allows for better lateral resolution in EDX microanalysis if compared to SEM. By STEM/EDX mapping some Bi particles with size in the range of 100 nm were detected (Fig. 6 below), and their presence is in agreement with the proposed chemical reaction.

4. Conclusion

Many innovative technical solutions have been proposed based on the Bi_2Se_3 topological insulator interfaced with metal Ag as an electrode, functional layer or cocatalyst [7, 11, 14, 20]. All these initial investigations do not take into account aging of the systems due to possible chemical changes of the interfaces. Here we have proven that such interface is not thermodynamically stable and will, with time, undergo a chemical reaction already at room temperature. We have shown that a spontaneous redox solid-state reaction with kinetics that is significant already at the room temperature will occur and produce Bi_2Se_3 to yield $AgBiSe_2$, Ag_2Se and Bi phase.

5. References

[1] Kane, C. L.; Mele, E. J., Z(2) topological order and the quantum spin Hall effect. *Phys. Rev. Lett.* **2005**, *95*, 146802.

[2] Fu, L.; Kane, C. L., Topological insulators with inversion symmetry. *Phys. Rev. B* **2007**, *76*, 045302.

[3] Kong, D. S.; Cui, Y., Opportunities in chemistry and materials science for topological insulators and their nanostructures. *Nat. Chem.* **2011**, *3*, 845-849.

[4] He, Q. L.; Lai, Y. H.; Lu, Y.; Law, K. T.; Sou, I. K., Surface Reactivity Enhancement on a Pd/Bi2Te3 Heterostructure through Robust Topological Surface States. *Sci. Rep.* **2013**, *3*, 2497.

[5] Iizuka, K.; Wato, T.; Miseki, Y.; Saito, K.; Kudo, A., Photocatalytic Reduction of Carbon Dioxide over Ag Cocatalyst-Loaded ALa(4)Ti(4)O(15) (A = Ca, Sr, and Ba) Using Water as a Reducing Reagent. *J. Am. Chem. Soc.* **2011**, *133*, 20863-20868.

[6] Chen, H.; Zhu, W. G.; Xiao, D.; Zhang, Z. Y., CO Oxidation Facilitated by Robust Surface States on Au-Covered Topological Insulators. *Phys. Rev. Lett.* **2011**, *107*, 056804.

[7] Das, B.; Sarkar, D.; Maity, S.; Chattopadhyay, K. K., Ag decorated topological surface state protected hierarchical Bi2Se3 nanoflakes for enhanced field emission properties. *J. Mater. Chem. C* **2015**, *3*, 1766-1775.

[8] Zhang, H. J.; Liu, C. X.; Qi, X. L.; Dai, X.; Fang, Z.; Zhang, S. C., Topological insulators in Bi2Se3, Bi2Te3 and Sb2Te3 with a single Dirac cone on the surface. *Nat. Phys.* **2009**, *5*, 438-442.

[9] Aramberri, H.; Munoz, M. C., Gap and spin texture engineering of Dirac topological states at the Cr-Bi2Se3 interface. *Phys. Rev. B* **2016**, *93*, 245401.

[10] Spataru, C. D.; Leonard, F., Fermi-level pinning, charge transfer, and relaxation of spin-momentum locking at metal contacts to topological insulators. *Phys. Rev. B* **2014**, *90*, 085115.

[11] Chang, C. H.; Chang, T. R.; Jeng, H. T., Newtype large Rashba splitting in quantum well states induced by spin chirality in metal/topological insulator heterostructures. *NPG Asia Mater.* **2016**, *8*, e332.

[12] Yang, H.; Peng, X. Y.; Wei, X. L.; Liu, W. L.; Zhu, W. G.; Xiao, D.; Stocks, G. M.; Zhong, J. X., Quantum oscillation of Rashba spin splitting in topological insulator Bi2Se3 induced by the quantum size effects of Pb adlayers. *Phys. Rev. B* **2012**, *86*, 155317.

[13] Otrokov, M. M.; Borisova, S. D.; Chis, V.; Vergniory, M. G.; Eremeev, S. V.; Kuznetsov, V. M.; Chulkov, E. V., Efficient Step-Mediated Intercalation of Silver Atoms Deposited on the Bi2Se3 Surface. *JETP Lett.* **2013**, *96*, 714-718.

[14] Xiao, J. P.; Kou, L. Z.; Yam, C. Y.; Frauenheim, T.; Yan, B. H., Toward Rational Design of Catalysts Supported on a Topological Insulator Substrate. *ACS Catal.* **2015**, *5*, 7063-7067.

[15] Schlenk, T.; Bianchi, M.; Koleini, M.; Eich, A.; Pietzsch, O.; Wehling, T. O.; Frauenheim, T.; Balatsky, A.; Mi, J. L.; Iversen, B. B.; Wiebe, J.; Khajetoorians, A. A.; Hofmann, P.; Wiesendanger, R., Controllable Magnetic Doping of the Surface State of a Topological Insulator. *Phys. Rev. Lett.* **2013**, *110*, 126804.

[16] Noh, H. J.; Jeong, J.; Cho, E. J.; Park, J.; Kim, J. S.; Kim, I.; Park, B. G.; Kim, H. D., Controlling the evolution of two-dimensional electron gas states at a metal/Bi2Se3 interface. *Phys. Rev. B* **2015**, *91*, 121110.

[17] Walsh, L. A.; Smyth, C. M.; Barton, A. T.; Wang, Q. X.; Che, Z. F.; Yue, R. Y.; Kim, J.; Kim, M. J.; Wallace, R. M.; Hinkle, C. L., Interface Chemistry of Contact Metals and Ferromagnets on the Topological Insulator Bi2Se3. *J. Phys. Chem. C* **2017**, *121*, 23551-23563.

[18] Koski, K. J.; Wessells, C. D.; Reed, B. W.; Cha, J. J.; Kong, D. S.; Cui, Y., Chemical Intercalation of Zerovalent Metals into 2D Layered Bi2Se3 Nanoribbons. *J. Am. Chem. Soc.* **2012**, *134*, 13773-13779.

[19] Pomogailo, A. D.; Dzhardimalieva, G. I. *Nanostructured Materials Preparation via Condensation Ways. 1 ed.*; Springer Netherlands: **2014**, 26-27.

[20] Ren, X. C.; Singh, A. K.; Fang, L.; Kanatzidis, M. G.; Tavazza, F.; Davydov, A. V.; Lauhon, L. J., Atom Probe Tomography Analysis of Ag Doping in 2D Layered Material (PbSe)(5)(Bi2Se3)(3). *Nano Lett.* **2016**, *16*, 6064-6069.

Morphology of organic semiconductor Perylene Diimide on graphene deposited by molecular-beam epitaxy

Vadym Tkachuk

University of Nova Gorica, Vipavska 13, SI-5000 Nova Gorica

Abstract

In this paper, we report about growing of N,N'-1H,1H-perfluorobutil dicyanoperylene-diimide (PDIF-CN_2), organic semiconductor, by molecular-beam epitaxy (MBE) on graphene flakes under different conditions. Describe the morphology of material on graphene flakes and silicon dioxide using atomic force microscope and scanning electron microscope, also we report about the difference in the growth mechanism for layers of different orders.

Keywords: graphene, organic semiconductor, PDIF-CN_2, molecular-beam epitaxy

1. Introduction

To increase efficiency and to minimize the modern electronics, more engineers and scientists are trying to find the answer in organic compounds. And in recent years, one of the most popular areas of electronics is skin electronics, in which organic semiconductors are in high demand. Particularly interesting for researchers is PDIF-CN_2.

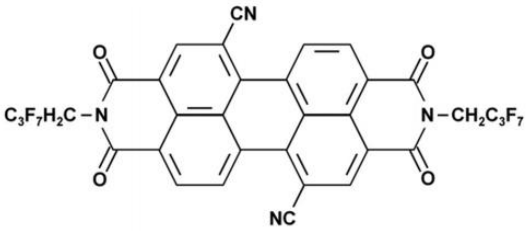

Figure 1: Molecular structures of PDIF-CN_2 semiconductor. Figure taken from [1].

This is organic n-type semiconductor with high carrier mobility [2, 3, 4], the highest charge carrier mobility of single crystal devices is about 6 $cm^2/V{\cdot}s$ [5, 6, 7], which makes

Email address: vadym.tkachuk@ung.si (Vadym Tkachuk)

this material very interesting for scientists. Another advantage is the excellent air-stability [8, 9], which expands the area of using of PDIF-CN_2. Studies on organic thin-film transistors (OTFTs) based on PDIF-CN_2 show that the electronic properties of organic semiconductor depend on the size of the crystals or fibers in the films and the structural quality. OTFTs, which are produced by spin-cast, with a fiber size of about 10 on 1.5 um, show the conductivity and mobility of carriers several times higher than that of conventional OTFTs [4]. Structural parameters and electronic properties are interrelated, future properties will depend on the formation of the coating, the type of deposition, the morphology and the microscope structure of the organic film. Molecular-beam epitaxy makes it possible to obtain films with a much higher structural quality and the larger the coverage area that gives more bonds between crystals, which in turn gives better electronic properties. Since heterostructures based on graphene and organic semiconductors will be in demand, it is necessary to study the behavior of these materials in order to create good samples. Therefore, we focused on studying the properties of a thin film of PDIF-CN_2 deposited with MBE on graphene.

2. Experimental setup

For the preparation of graphene, we have used natural graphite and mechanical exfoliation method. Flakes were prepared on 300nm-thick silicon dioxide (SiO_2) layer grown on silicon substrates. Cleaning of wafers took place in three stages: sonification in acetone, sonification in isopropanol alcohol and oxygen plasma cleaning. Below are images of some graphene flakes that were used in the experiment.

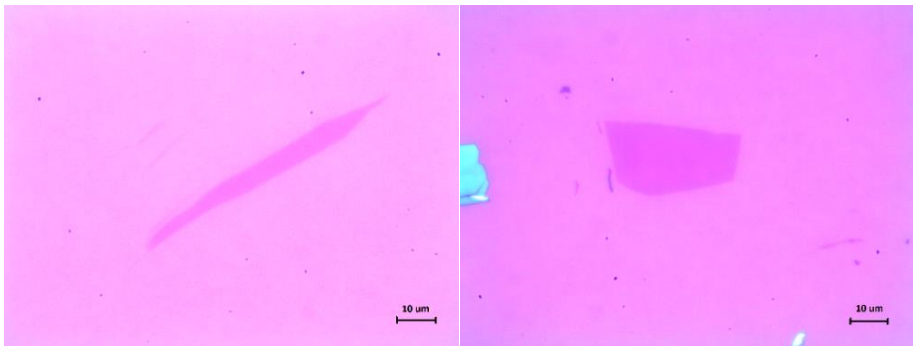

Figure 2: Optical microscopy images of graphene flakes on silicon dioxide wafers.

All the flakes were tested on atomic force microscope (AFM), each flake having a thickness of about ~1.2 nm, which means that we have single layer of graphene see AFM image and line profile on Figure 3.

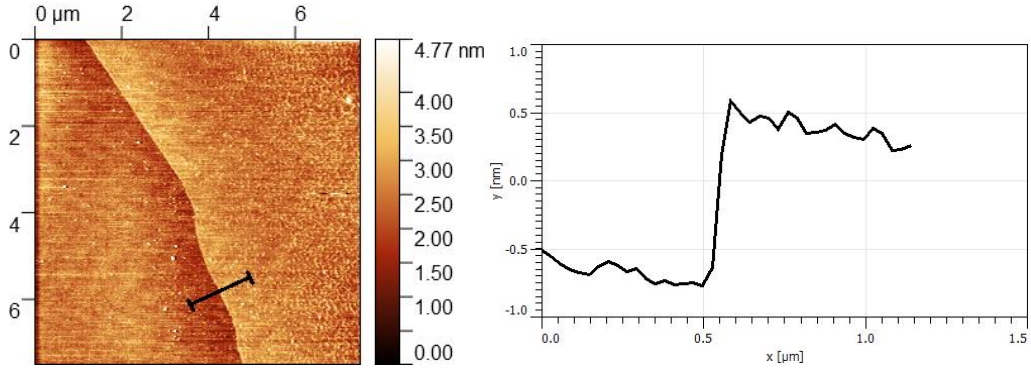

Figure 3: AFM image of graphene flake and the line profile acquired along the black line are shown.

PDIF-CN_2 powder was purchased from Polyera Corporation. For deposition of PDIF-CN_2 was used molecular-beam epitaxy (MBE) technique. All experiments were carried with vacuum in the chamber between 10^{-5} and 10^{-6} Pa. The temperature of the chamber was between 295 and 298 K during deposition, silicon substrates temperature was kipping at 318 K. The Rate of growing was controlled by quartz crystal microbalance. Evaporation was carried out at two temperatures of the evaporation cell, 468 K and 458 K with the different time of exposure.

Morphological characterizations of samples were performed also by AFM (A.P.E.Research A100 Atomic Force Microscope) in noncontact mode and Scanning Electron Microscope (SEM) (Jeol SSM-7100 F) techniques, which are described in the works [10,11]. Images were analyzed by Gwyddion open source software.

3. Results and discussion

The five samples were prepared with the different rate of coverage by PDIF-CN_2. In the first three cases, samples were covered with the same temperature of the evaporation cell 468 K, but with the different time of exposure 10 minutes, 3 minutes and 1 minute. Another two samples were covered with the temperature 458 K and with the time of exposition 3 minutes and 1 minute. All parameters about the samples are presented in Table 1.

Sample:	T_{cell} (K)	T_{sub} (K)	Time (min.)	Volume* (um^3)	Coverage (%)
#1	468	318	10	0.035	100**
#2	468		3	0.007	100**
#3	468		1	7.1×10^{-7}	49.2
#4	458		1	3.2×10^{-7}	24.5
#5	458		3	11.1×10^{-7}	73.6

Table 1. Description and statistical parameters of the samples (* - volume of material on 9 um^2 area, ** - in this case, on samples are few layers of PDIF-CN_2, so coverage is 100%).

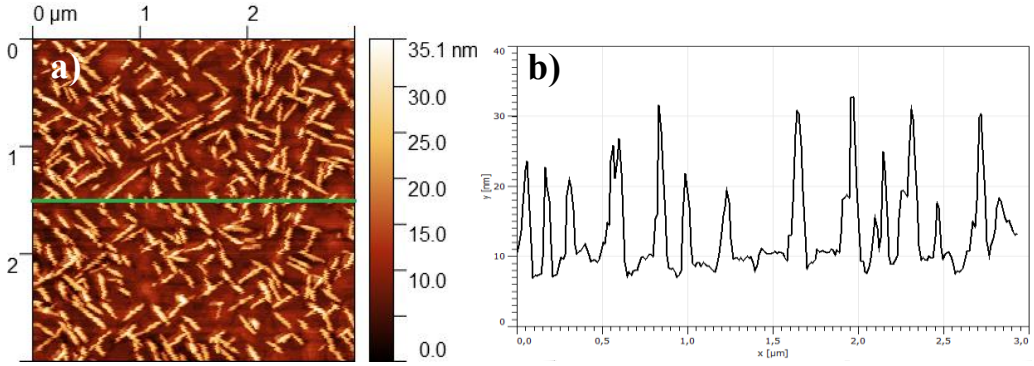

Figure 4: AFM image of the graphene flake with PDIF-CN_2 on the first sample (a) with the line profile, obtained along the green line (b).

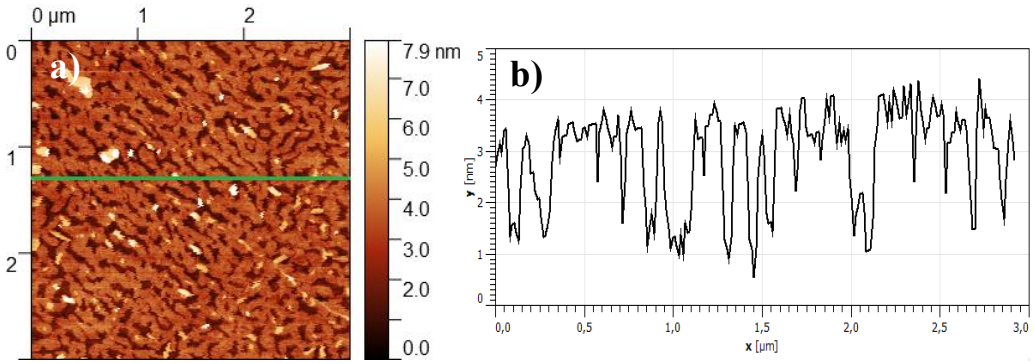

Figure 5: AFM image of the graphene flake with PDIF-CN_2 on the second sample (a) with the line profile (b).

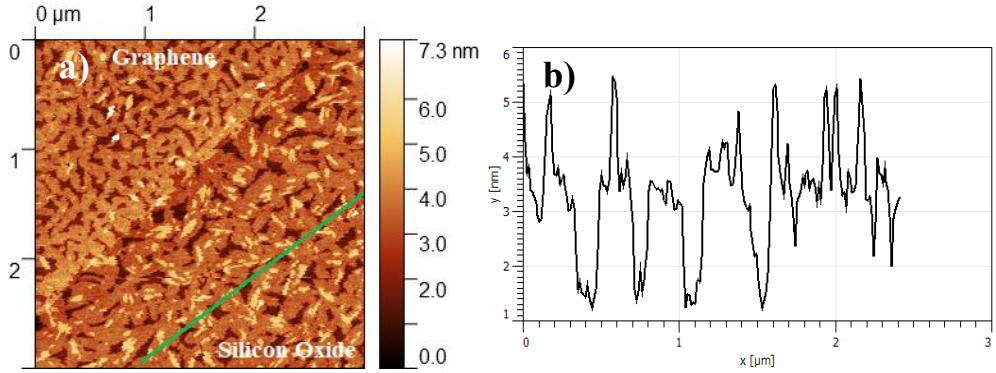

Figure 6: AFM image of the edge of graphene flake with PDIF-CN_2 on the second sample (a) with the line profile (b).

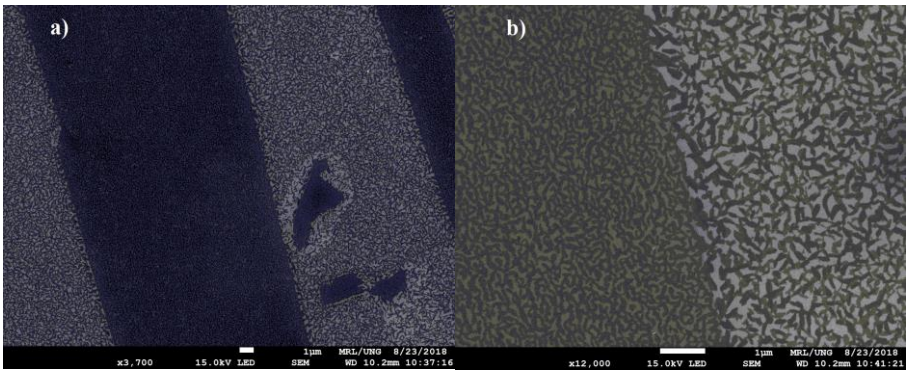

Figure 7: SEM images of the graphene flake (dark grey) with PDIF-CN_2 on SiO_2 (light grey) a) and edge of graphene flake b).

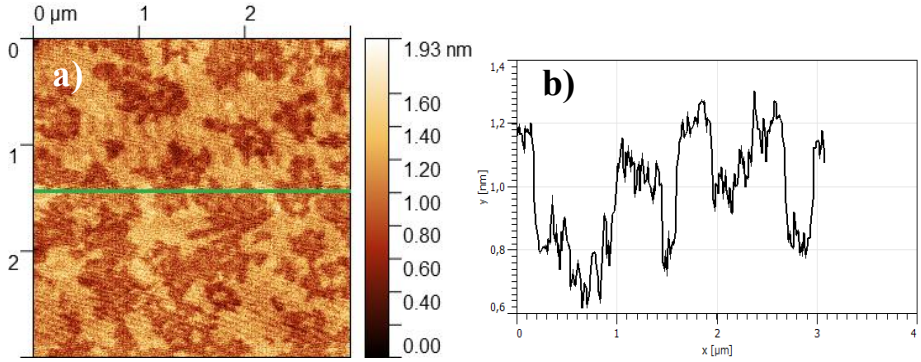

Figure 8: AFM image of the graphene flake with PDIF-CN_2 on the third sample (a) with the line profile (b).

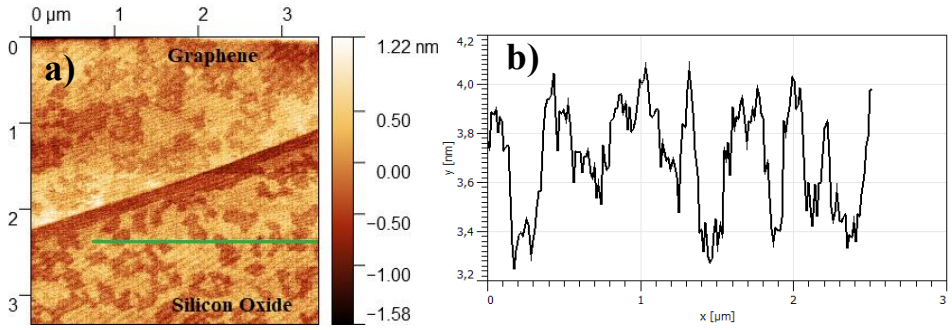

Figure 9: AFM image of the edge of graphene flake with PDIF-CN_2 on the third sample (a) and the line profile (b).

Now, if we compare all the results from Figure 4, 5 and 8, we will see that in one of the three cases we have a completely different result, the morphology of the surface looks different. In the first case, the sample has an islet morphology, probably because the exposure time (10 min.) was too long, the islands was growing higher and higher, from which it can be concluded that the main process here was the growth of the Volmer-Weber type. The most interesting to compare second sample (Figure 5) and third sample (Figure 8), on the second sample, the average thickness of one layer of PDIF-CN_2 is about ~ 2.2 nm, when the average thickness of the layer on the second sample is about ~ 0.58 nm, see Figure 10.

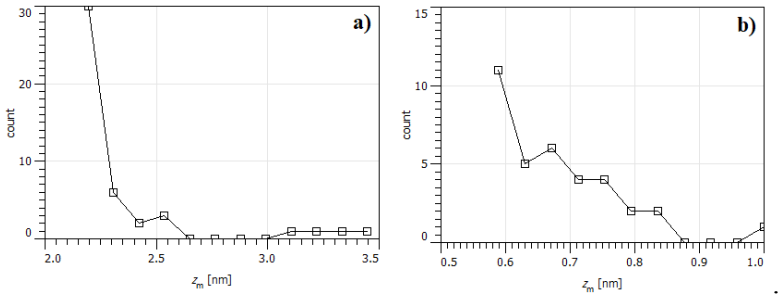

Figure 10: Statistical distribution of the height of the second sample a) and the third sample b).

The same temperature of the evaporation cell (468 K) gave the same flow of material on the sample in all the first three experiments, the difference is only in exposure time. From this we can make conclusion that first few layers of PDIF-CN_2 grow differently in comparison with the next layers. The PDIF-CN_2 has two isomers, PDIF-CN_2-1,6 and PDIF-CN_2-1,7, in our experiment we have used second isomer. This isomer PDIF-CN_2-1,7 has triclinic crystal structure and unit cell parameters: a = 0.513 nm, b = 0.738 nm, c = 1.959 nm, $\alpha = 92.35°$,$\beta = 82.22°$, $\gamma = 93.25°$ [12]. Knowing the parameters of the crystal lattice of PDIF-CN_2, we can say that the first layer with a thickness of 0.6 nm has a "horizontal" orientation of the molecules, and the following layers have a "vertical" orientation of the

molecules, which converges with the a-axis 0.51 nm length and c-axis 2 nm crystal structure.

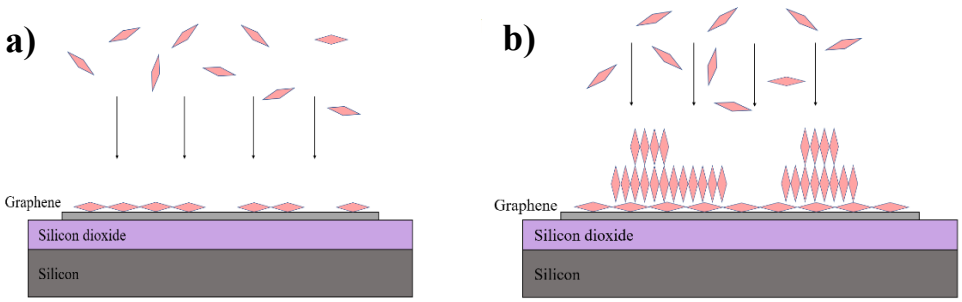

Figure 11: Schematic sketch of the formation by molecules of the first layer a) and the following layers b).

In Figure 11 shows the stages of growing PDIF-CN_2, the molecules of the first layer are structured in a lying down configuration, and after the first layer is fully formed, another type of growth takes place, here the molecules are in a standing position. The first layer shows Frank-van der Merwe type of growth but in the following layers is Volmer-Weber type of growth. It can be explained that the relaxation process depends on the wetting region around the islands on graphene flake, this region is similar to some adhesive layer around, where the diffusion of molecules is much higher [13].

Now, if we compare the morphology of PDIF-CN_2 with flakes of graphene and SiO_2, we see that there are no big differences, the thickness of the first layer of material on SiO_2, Figure 9, is about 0.6 nm, as well as on graphene. The following layers have a thickness of about 2 nm, Figure 6. Difference is only in that the islands on SiO_2 look larger, and in some places the second layer of material begins to grow. Therefore, after this we can conclude that the growth of PDIF-CN_2 on the flake of graphene and on SiO_2 goes the same way, but on silicon dioxide it goes a little faster.

Also, was done evaporation with cell temperature of about 458 K and an exposure time of 3 minutes and 1 minute, bellow are presented AFM images of this samples. A lower temperature gives a lower flow of material and lower growth rate of the layers.

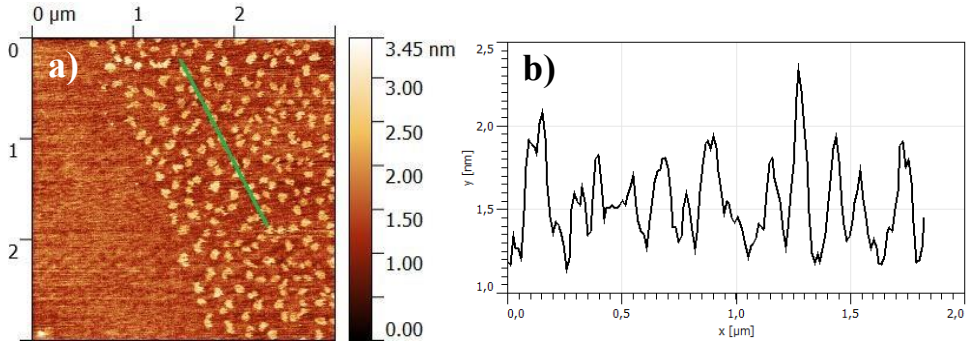

Figure 12: AFM image of the edge of graphene flake with PDIF-CN_2 on the fourth sample (a) and the line profile (b).

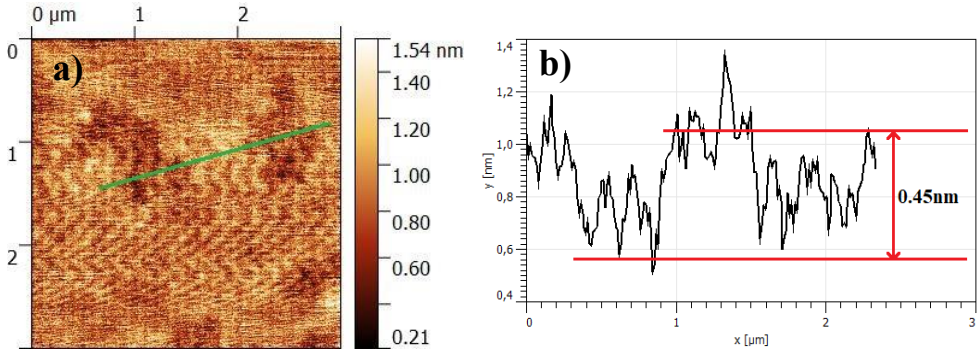

Figure 13: AFM image of the graphene flake with PDIF-CN_2 on the fifth sample (a) with the line profile (b).

Figure 12 shows that the graphene layer has only islands of PDIF-CN_2, 1 minute with a material flow at 458 K is not enough to form a complete layer, the height of these islands is about 0.4-0.6 nm, which still converges with the a-axis of the crystal structure of PDIF-CN_2. In Figure 13 shows the topography of PDIF-CN_2 on a graphene flake with the same temperature, but with a longer exposure time, 3 minutes, now we see almost complete layer just with the holes in material, thickness of layer in this case is about 0.45 nm. As we see in these two cases, the thickness of the layer is about 0.5 nm, it tells us that the molecules in the first layer are also in lying down position, like in first three cases. At different deposition rates, we observe the same growth mechanism for the first and subsequent layers, i.e. this mechanism does not depend on the rate of deposition of the material.

4. Conclusion

In this study, we describe the morphology and structural parameters of an organic semiconductor as PDIF-CN_2 on a single-layered graphene deposited by molecular beam epitaxy. We found a fundamental difference in growth mechanism for the bottom and

following layers, that is due to the peculiarity of the structure of PDIF-CN_2 molecule. The growth mechanisms of PDIF on graphene and SiO_2 are identical, and the layers have the same properties.

References

[1] H. Zhengran et al. *Air-stable solution-processed n-channel organic thin film transistors with polymer-enhanced morphology*. Applied physics letters 106, 183301, **2015**.

[2] F. Chiarella et al. *Spontaneous Wetting Dynamics in Perylene Diimide n-Type Thin Films Deposited at Room Temperature by Supersonic Molecular Beam*. The Journal of Physical Chemistry. 120 (45), pp 26076–26082, **2016**.

[3] R. Colle et al. *Structural, electronic and vibrational properties of N,N'-1H,1H-perfluorobutyl dicyanoperylenecarboxydiimide (PDI-FCN_2) crystal*. The journal of Chemical Physics 139, 114507, **2013**.

[4] A. Jones et al. *Substrate-induced and thin-film phases: Polymorphism of organic materials on surfaces*. Advanced Functional Materials 26, 2233–2255, **2016**.

[5] F. Leroy et al. *How to control solid state dewetting: A short review*. Surface Science Reports 71, 391–409, **2016**.

[6] C. Newman et al. *Introduction to organic thin film transistors and design of n-channel organic semiconductors*. Chemistry of Materials 16, 4436, **2004**.

[7] S. Jacob et al. *High performance printed n and p-type {OTFTs} enabling digital and analog complementary circuits on flexible plastic substrate*. Solid-State Electronics 84, 167, **2013**.

[8] S. Steudel et al. *50 mhz rectifier based on an organic diode*. Nature Materials 4, 597, **2005**.

[9] A. Molinari et al. *High electron mobility in vacuum and ambient for PDIF-CN_2 single-crystal transistors*. Journal of the American Chemical Society 131, 2462, **2006**.

[10] J. Goldstein et al. *Scanning Electron Microscopy and X-Ray Microanalysis*.

[11] S. Yongho et al. *Atomic force microscopy and spectroscopy*. Reports on progress in physics 71, 016101, **2008**.

[12] R. Colle et al. *Structure and x-ray spectrum of crystalline poly(3-hexylthiophene) from dft-Van der Waals calculations*. Physica status solidi (b) 248, 1360, **2011**.

[13] R. Colle et al. *Anisotropic molecular packing of soluble C_{60} fullerenes in hexagonal nanocrystals obtained by solvent vapor annealing*. Carbon 50, 1332, **2012**.

Orbital selective ultrafast electron dynamics in Fe-pnictide superconductors

Tanusree Saha

Laboratory of Quantum Optics, University of Nova Gorica, Ajdovščina 5270, Slovenia

Abstract

Femtosecond spectroscopy is used to investigate the time evolution of the electronic structure in Fe-based high temperature superconductors. We have studied the orbital-selective dynamics of electrons in one of these systems, $EuFe_2As_2$, and observed two different relaxation time scales for d_{xz}/d_{yz} and d_{xy} electrons of Fe atoms. The d_{xz}/d_{yz} electrons relax faster through the electron-electron scattering channel, showing an itinerant character, while d_{xy} electrons relax much slower, since they form a quasiequilibrium state with the lattice due to their localised character. Our findings suggest that electron correlation is an important property in these systems which should be taken into careful account when describing the electronic properties of both parent and carrier-doped compounds, and therefore establish a strong connection with cuprate superconductors.

Keywords: Superconductors, relaxation time, electron correlation

1. Introduction

The parent compounds of Fe-based superconductors are paramagnetic metals and undergo structural and magnetic transitions exhibiting a spin density wave (SDW) state as the ground state is anti-ferromagnetic [1] with Fe atoms possessing magnetic moments close to a Bohr magneton [2, 3, 4, 6]. These materials exhibit varied unusual phenomena involving competing interactions related to magnetic order and superconductivity [7, 8]. The suppression of anti-ferromagnetic ordering by doping or pressure leads to the emergence of superconductivity. Thus, understanding the role of the magnetic ground state and the coupling between low-energy excitations

Email address: tanusree.saha1992@gmail.com (Tanusree Saha)

like spin fluctuations and lattice vibrations may be an important step towards the understanding of superconductivity in the high temperature superconductors.

One promising approach to study such interactions is to analyse the excited states of optically excited materials and their subsequent relaxation in the energy phase space employing femtosecond spectroscopy. In typical metals, this involves electron-electron (e-e) and electron-phonon (e-ph) scattering rates [9, 10], but in more complex materials with ordered states emerging in competition with thermal fluctuations, e.g., superconducting, charge density wave (CDW), or magnetically ordered materials, excitations specific to the ordered nature become essential [11]. Metallic anti-ferromagnet like Fe-pnictide parent compounds now offer the opportunity to analyse the interaction of low-energy electrons with spin fluctuations in an anti-ferromagnet and to probe transient changes of the electronic band structure intimately connected to anti-ferromagnetic order.

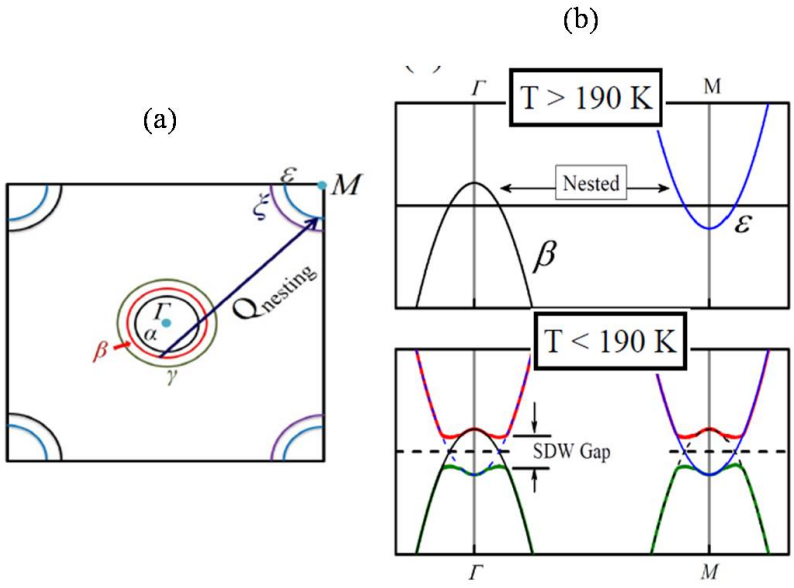

Figure 1: (a) Fermi surface nesting in 2D k-space between the β band (hole pocket) at Γ-point and the electron pocket at M-point. The arrow indicates the nesting vector $\mathbf{q}$= (π, π). (b) Energy band diagram showing the formation of spin density wave (SDW) gap in the anti-ferromagnetic phase below 190 K.

The generic electronic structure of Fe-based superconductors consists of three hole bands at the Brillouin zone center (Γ point), and two electron bands at the Brillouin zone corner (M point). The inner two hole bands, named α and β, have primary contributions from d_{xz} and d_{yz} orbitals , whereas the outer hole band, named γ, has the main contribution from d_{xy} orbitals. The strong nesting of the inner hole pocket (β band) at Γ point with an electron pocket at M point along the vector **q**= (π, π) leads, at low temperatures, to anti-ferromagnetic ordering of Fe magnetic moments and the formation of a spin density wave (SDW), which is accompanied or preceded by a structural transition from tetragonal to orthorhombic structure [12, 13]. The band picture is shown in Figure 1.

In this work, we studied the orbital selective dynamics of the photoexcited electrons in $EuFe_2As_2$, a parent compound of Fe-based high temperature superconductors, at temperatures above and below the magnetic and structural transitions. We employ time- and angle-resolved photoelectron spectroscopy (trARPES) as a tool to investigate the relaxation dynamics of the electrons from different orbitals in these systems.

2. Experimental Methods

Single crystals of $EuFe_2As_2$ were grown using a high temperature solution growth method as described in [14, 15] in the Crystal Growth Lab at Tata Institute of Fundamental Research, INDIA. The composition and structure were verified by energy dispersive analysis of X-rays and X-ray diffraction. Single crystallinity was ensured by a sharp Laue pattern. Angle-resolved photoemission (ARPES) measurements were carried out in the Laboratory of Quantum Optics (LKO), University of Nova Gorica, using a VG Scienta R3000 electron analyser with an energy resolution of 20 meV and angular resolution of $\approx 0.4^o$. Time-resolved photoemission spectroscopy was carried out using a mode-locked Ti:sapphire laser system delivering pulses at 1.5 eV (800 nm), with 50 fs duration and 5 kHz repetition rate. The beam intensity was split into two parts. The major part of the intensity was used to generate high-order harmonics, spanning the energy range 10-50 eV, in Argon [16]. The second part of the beam was used as a pump, whose intensity was controlled with a variable attenuator based on a half wave-plate and a polariser. We could select the desired harmonics and control their flux by means of a specially-designed grating set-up, which preserves the pulse duration. The probe energy was set to 29 eV. The samples were cleaved *in situ* at pressure 6.67 X 10^{-8} Pa, yielding mirror like clean surfaces. The measurements were done at 1.33 X 10^{-8} Pa. The probe

polarization was fixed to s-pol and the pump polarization was adjusted using a polarizer. Thus, by changing the polarisation of the pump beam in time resolved photoemission spectroscopy, we are able to capture the time scales of the various orbital dependent electronic processes and reveal the underlying coupling phenomena during the different transitions.

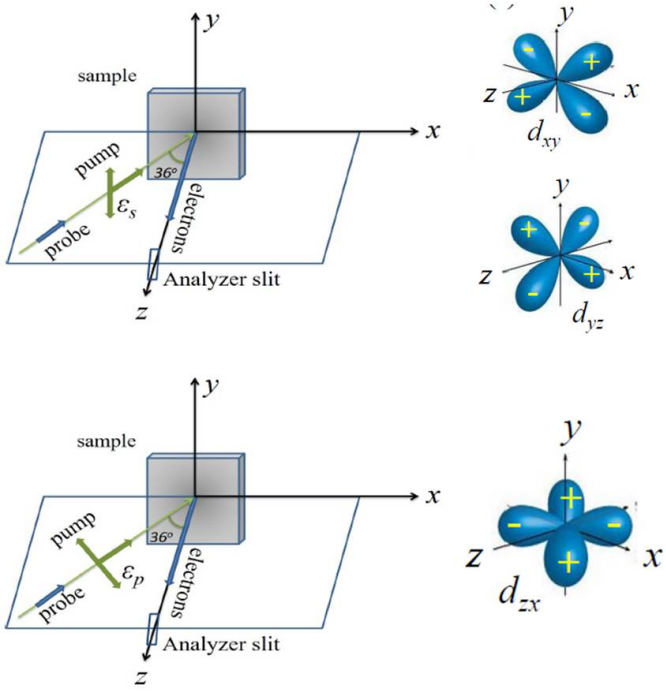

Figure 2: Geometry of the experimental configuration s-polarisation and p-polarisation of the pump pulse. The direction of the pump and probe beams have been indicated by green and blue colours, respectively.

In a time-resolved ARPES (trARPES) experiment, the dynamics of photoexcited electrons can be tracked by varying the delay between the low-energy (visible or infrared) pump and the high-energy (extreme ultraviolet) probe beam. This gives information about different coupling phenomena, excitation modes and relaxation processes. The different electronic states can be probed selectively by adjusting the polarisation of the excitation pulse as shown in Figure 2. The s-polarised pump beam has electric field vector parallel to the surface, whereas the electric field vector of p-polarised beam, making an angle of around 36^o with the sample surface, is directed

out of plane of the sample surface. In the s-polarised configuration, the pump beam mainly excites the d_{xy} and d_{yz} orbitals, while in the p-polarised configuration the excitation cross-section will be higher for electrons in the out-of-plane d_{xz} orbitals.

3. Results and Discussion

In Figure 3(a) and 3(b), we have shown the the time-resolved photoemission (trPES) spectra as a function of the delay between pump and probe beams at 210 K, i.e above the SDW transition temperature T_N = 190 K, for both the polarisations of the pump pulse. We observe that the intensity of

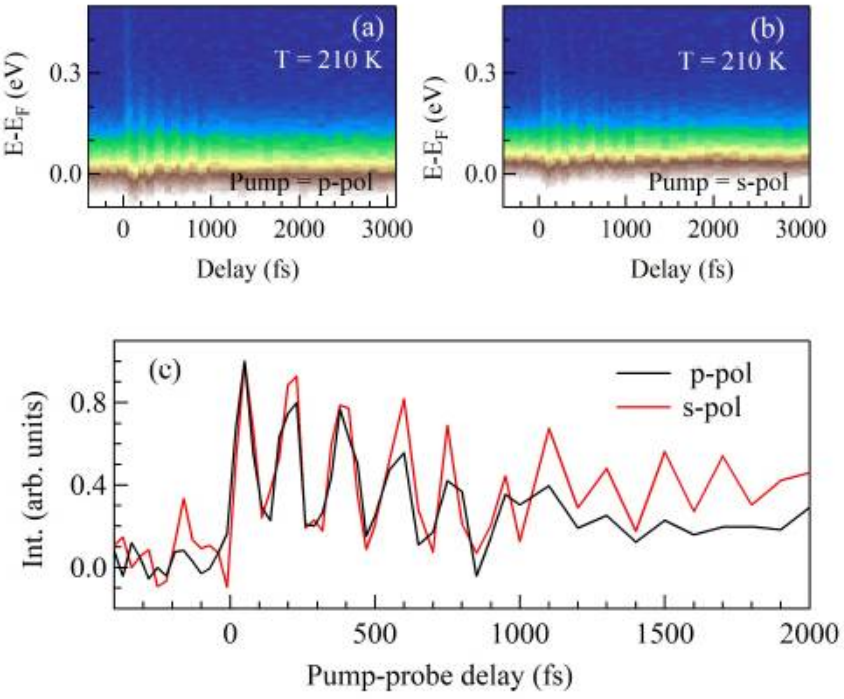

Figure 3: Time resolved photoemission (tr-PES) spectra as a function of the pump-probe delay at 210 K for (a) s-polarisation and (b) p-polarisation of the pump. (c) Intensity of the electrons, integrated within binding energy window 0.1-0.2 eV, as a function of the delay between pump and probe beams.

hot electrons, integrated within the binding energy window 0.1 eV to 0.2 eV, shows a sharp rise after t_0 (time at which there is temporal overlap between the pump and probe pulses) followed by coherent oscillations and

then there is a decay of the signal on a time scale of a few picoseconds, as shown in Figure 3(c). After optical excitation of electrons to unoccupied states, there is a thermal redistribution of energy among the electrons (e-e thermalisation), which happens within tens of femtoseconds, after which there are electron-lattice interactions giving rise to different coherent collective excitation modes such as phonons and magnons within hundreds of femtoseconds. The frequency of oscillations is 5.6 THz (around 23 meV), for both polarizations, which, as reported earlier [17], corresponds to the fully symmetric A_{1g} phonon mode, triggered by the breathing of As atoms along c-axis. From Figure 3(c), we find that the electron relaxation dynamics is significantly different for the two polarisations. Though there are coherent oscillations in both cases, but the electrons excited by the p-polarised pump decay faster as compared to the decay of the electrons excited by s-polarised pump. Also, the spectral intensity for p-polarised pump shows faster damping than that for s-polarised pump.

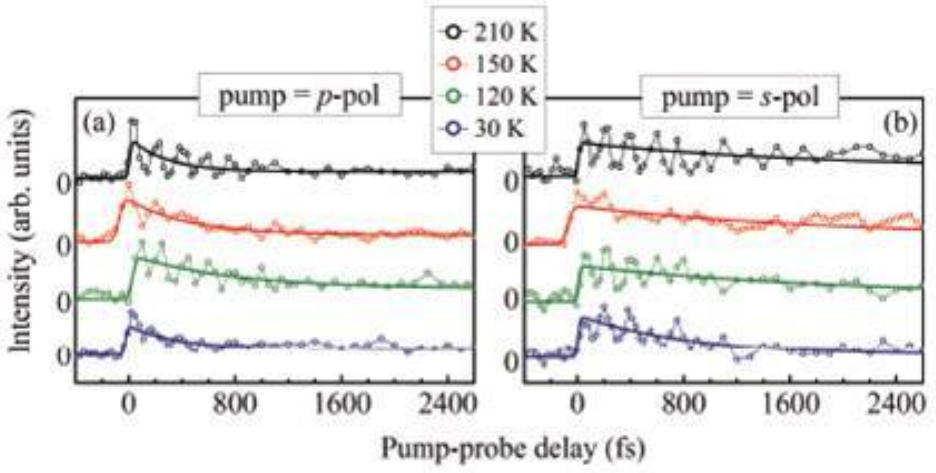

Figure 4: (color online) Spectral intensity of the hot electrons as a function of pump-probe delay time, Δt for (a) p-polarized and (b) s-polarized pump beam at different sample temperatures. Solid lines represent single exponential fits.

The intensity of the hot electrons, I_+ are shown in Figure 4 for both p-pol and s-pol pump excitations. To analyse the temporal dynamics of the hot holes, the intensity (I_-) was integrated within an energy window of 0.1 eV below the Fermi level. The time-dependent intensity profiles of the hot holes for p- and s-polarizations of the pump at different temperatures are

shown in Figure 5. The data has been normalised and fitted with an exponential decay function, $I_{+,-}$ = A$e^{-t/\tau_{+,-}}$+B, to extract the time constants for the decay of the excited states. Here, A is the amplitude of the excitation, $\tau_{+,-}$ is the decay time constant of the electrons or holes, respectively, and B accounts for the background originating from electron phonon scattering. The fitting function was multiplied by a step function at (Δt) = 0 and convoluted with a Gaussian function to account for finite durations of the pump and probe pulses.

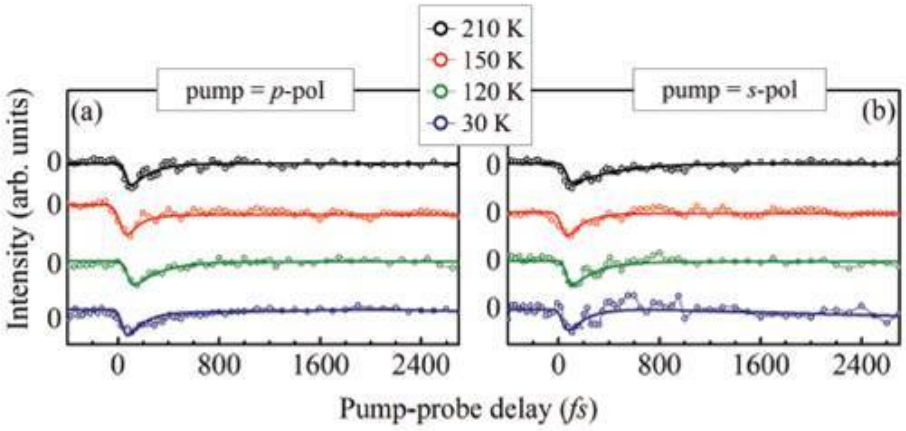

Figure 5: (color online) Spectral intensity of the hole excitations as a function of pump-probe delay time, Δt for (a) p-polarized and (b) s-polarized pump beam at different sample temperatures. Solid lines represent single exponential fits.

The extracted decay constants as a function of temperature have been shown for electrons in Figure 6 and for holes in Figure 7, for both polarisations of pump pulse. We observe that the relaxation time constants for hot electrons are significantly different for the two pump polarisations while for the hole excitations, they are similar for $T < T_N$. At 210 K, however, the decay time for the hole created by s-polarized light is longer than that for p-polarized case. For the hot electrons, when excited by p-polarised light, the electrons are observed to relax faster with time constant of the order of 500 fs but they relax quite slowly with time constant of 1-2 ps when excited by s-polarised beam. Now, for p-polarisation, we see that the relaxation is slower for $T < T_N$, i.e, in the SDW state, than that at 210 K (above SDW transition) while for s-polarisation, there are no significant changes with temperature. In the p-polarised configuration (primarily the d_{xz} orbitals are excited), the fast relaxation dynamics can be explained by

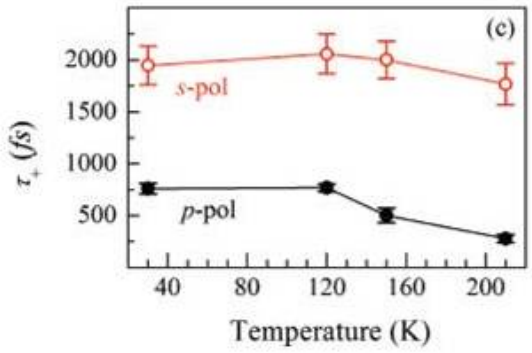

Figure 6: Decay time constants of the hot electrons, τ_+, as a function of temperature for p-polarised and s-polarised pump beam.

the inter-band scattering between the β band and the electron pocket at the M-point, which is possible due to Fermi surface nesting between the two pockets. This fast relaxation can be attributed to the itinerant nature of the d_{xz} electrons. But the relaxation dynamics observed for s-polarised case is complex. It appears to follow a trend similar to the p-polarised case for short time delays but at longer delay times, it is different. The data in the shorter delay time seem to have influence from d_{yz} states while the longer delay time is predominantly contributed by the decay of d_{xy} electrons. This shows the localised character of the d_{xy} electrons. As the γ band

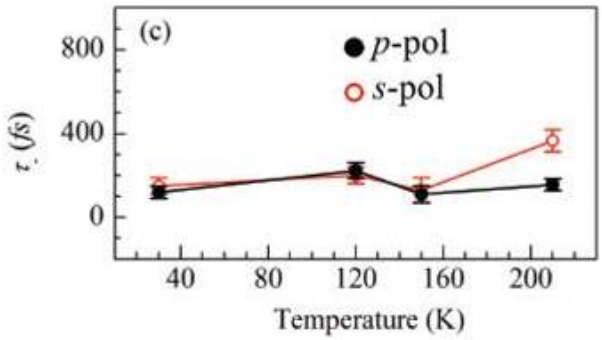

Figure 7: Decay time constants of the holes, τ_-, as a function of temperature for p-polarised and s-polarised pump beam.

has no nesting condition with any other band, d_{xy} electrons can only decay through intra-band scattering and hence are longer lived. Because of the

absence of nesting for the γ band, the d_{xy} electrons do not participate in the SDW transition. For the dynamics of the holes, similar scenario can be seen in the paramagnetic phase at 210 K where the time constant is more for the hole excitations in s-polarised case than that for p-polarised case. In the SDW phase ($T < T_N$), the local character of d_{xz} states enhances significantly due to the SDW gap and the difference in decay time for s-polarised and p-polarised cases becomes insignificant. We can thus say, that, the d_{xz} and d_{yz} electrons participate in the magnetic (SDW) transition and are itinerant while the d_{xy} electrons are localised and also do not contribute in the magnetic transition. Since there is also a structural transition at about the same transition temperature of 190 K, it can be predicted that the d_{xy} electrons contribute in this structural transition. This is a part of our future studies on how we can decouple the different transitions by changing the polarisation of the pump beam and to estimate their decay times.

4. Conclusions

In this study, we have used a different kind of technique to probe the orbital selective electronic behaviour in strongly correlated systems. We have observed that the time scales of electron relaxation for d_{xy} and d_{xz}/d_{yz} orbitals are different in $EuFe_2As_2$. The d_{xz}/d_{yz} electrons relax faster through electron-electron scattering channel, which shows their itinerant behaviour. But, d_{xy} electrons have longer relaxation time scales since they form a quasi-equilibrium state with the lattice and are, thus, localised. Although the ratio between effective masses of electrons belonging to d_{xz}/d_{yz} and d_{xy} orbitals measured with different techniques, such as ARPES and quantum oscillations, is ~ 1 [18, 19, 20], our results show that electron dynamics is dependent on the orbital geometry and there are strong electron correlation effects in this system.

References

[1] P. Dai, Rev. Mod. Phys. 87, 855 (2015).

[2] N. Ni, S. Nandi, A. Kreyssig, A. I. Goldman, E. D. Mun, S. L. Budko, and P. C. Canfield, Phys. Rev. B 78, 014523 (2008).

[3] A. I. Goldman, D. N. Argyriou, B. Ouladdiaf, T. Chatterji, A. Kreyssig, S. Nandi, N. Ni, S. L. Budko, P. C. Canfield, and R. J. McQueeney, Phys. Rev. B 78, 100506 (2008).

[4] K. Maiti, Pramana 84, 947 (2015).

[5] Q. Huang, Y. Qiu, W. Bao, M. A. Green, J. W. Lynn, Y. C. Gasparovic, T. Wu, G. Wu, and X. H. Chen, Phys. Rev. Lett. 101, 257003 (2008).

[6] C. de La Cruz, Q. Huang, J. W. Lynn, J. Li, W. Ratcliff, II, J. L. Zarestky, H. A. Mook, G. F. Chen, J. L. Luo, N. L. Wang, and P. Dai, Nature (London) 453, 899 (2008).

[7] D. Parker, M. G. Vavilov, A. V. Chubukov, and I. I. Mazin, Phys. Rev. B 80, 100508 (2009).

[8] G. Adhikary, N. Sahadev, D. Biswas, R. Bindu, N. Kumar, A. Thamizhavel, S. K. Dhar, and K. Maiti, J. Phys.: Condens.Matter 25, 225701 (2013).

[9] N. Del Fatti et al., Phys. Rev. B 61, 16956 (2000).

[10] E.V. Chulkov et al., Chem. Rev. 106, 4160 (2006).

[11] H. Schafer et al., Phys. Rev. Lett. 105, 066402 (2010).

[12] C. de la Cruz et al., Nature (London) 453, 899 (2008).

[13] Q. Huang et al., Phys. Rev. Lett. 101, 257003 (2008).

[14] N. Kumar, R. Nagalakshmi, R. Kulkarni, P. L. Paulose, A. K. Nigam, S. K. Dhar, and A. Thamizhavel,Phys.Rev.B79, 012504 (2009).

[15] R. Mittal, L. Pintschovius, D. Lamago, R. Heid, K. P. Bohnen, D. Reznik, S. L. Chaplot, Y. Su, N. Kumar, S. K. Dhar, A. Thamizhavel, and Th. Brueckel, Phys. Rev. Lett. 102, 217001 (2009).

[16] C. Grazioli, C. Callegari, A. Ciavardini, M. Coreno, F. Frassetto, D. Gauthier, D. Golob, R. Ivanov, A. Kivimaki, B. Mahieu, B. Bucar, M. Merhar, P. Miotti, L. Poletto, E. Polo, B. Ressel, C. Spezzani, and G. De Ninno, Rev. Sci. Instrum. 85, 023104 (2014).

[17] I. Avigo, R. Cortes, L. Rettig, S. Thirupathaiah, H. S.Jeevan, P. Gegenwart, T. Wolf, M. Ligges, M. Wolf, J.Fink, and U. Bovensiepen, J. Phys.: Condens. Matter 25, 094003 (2013).

[18] S. L. Skornyakov, A. V. Efremov, N. A. Skorikov, M. A. Korotin, Yu. A. Izyumov, V. I. Anisimov, A. V. Kozhevnikov, and D. Vollhardt, Phys. Rev. B 80, 092501 (2009).

[19] J. G. Analytis, R. D. McDonald, J.-H. Chu, S. C. Riggs, A. F. Bangura, C. Kucharczyk, M. Johannes, and I. R. Fisher, Phys. Rev. B 80, 064507 (2009).

[20] S. E. Sebastian, J. Gillett, N Harrison, P. H. C. Lau, D. J. Singh, C. H. Mielke, and G. G. Lonzarich, J. Phys.: Condens. Matter 20, 422203 (2008).

Synthesis of Bi_2Se_3 plates by means of hydrothermal method

Zipporah Rini Benher

Materials Research Laboratory, University of Nova Gorica, Vipavska 11c, SI-5270 Ajdovščina, Slovenia

Abstract

New methodology for producing high quality Bi_2Se_3 plates has been developed. Bi_2Se_3 plates were prepared with hydrothermal method. Different reaction conditions have been investigated to obtain plates having a diameter of ~ 500 nm. The Bi_2Se_3 plates were characterized using x-ray diffraction, scanning electron micropscopy with energy-dispersive x-ray spectroscopy and transmission electron microscopy.

Keywords: hydrothermal method, topological insulator, x-ray diffraction, scanning electron micropscopy, transmission electron microscopy.

1. Introduction

Topological Insulators (TIs) have developed the great concern in the field of science due to its interesting nature such as insulating bulk gap and metallic surface states. Bismuth selenide (Bi_2Se_3) being one of the TIs has a rhombohedral crystal structure, each quintuple layer (QL) has been combined by the weak van der Waals interaction [1]. Due to the topology of their electronic band structure, TIs have insulating bulk and conducting surfaces (or edges) due to the presence of some special surface states that are also spin polarized. In the presence of non-magnetic impurities, topological surface states (TSS) are immune to backscattering and this characteristic makes this class of materials particular interest in the field of nano- electronics and spintronics. TI based nano devices can have better performance in terms of speed, high cut-off frequency and low power consumption [2-7]. The fabrication of such nano-devices requires high-quality TI that can be produced under easy and robust synthesis conditions.

At present, there are different methods for the preparation of Bi_2Se_3. Bi_2Se_3 can be prepared by exfoliation methods, which have been widely used to produce nano sheets from the single crystals. High quality single crystals of Bi_2Se_3, are grown by Bridgman method [8,9]. Mechanical exfoliation can be done by adhesive tape peeling or by lithium intercalation, a chemical exfoliation method that could produce high quality nano sheets from the single crystals [10,11] even though lithium intercalation method has found to be less effective for selenide and telluride families of materials [12-14]. Exfoliation is an easy fabrication method, but has some disadvantages like poor controllability, low yield and irregular shapes which could not be used widely in studies and applications. Another method is a Chemical Vapor Deposition (CVD) method, an easily accessible method used for the production of high quality nanoribbons, nanowires and nano plates in large scale with large surface to volume ratio, which might significantly decrease the conduction in bulk carriers. However, the CVD has low deposition rate [15]. Metal Organic Chemical Vapor Deposition (MOCVD) method, developed by the vapor phase epitaxy where the organic compounds and the hydrides are used as the source materials. MOCVD produces high purity material in large scale with less defects and has good controllability over thickness. Expensive equipment and harmful source materials being a limitation in MOCVD [16]. Another widely used method is Molecular Beam Epitaxy (MBE), used to produce highly pure thin films with the source materials which are condensed on the wafer as gaseous elements to form the desired compound materials on the films. Despite being more advantageous with respect to uniform thickness, accurate composition, good crystal integrity and slow growth rate, MBE requires high maintenance cost and high vacuum [17-18]. Bi_2Se_3 can be prepared by solvothermal synthesis due to its simple procedure where the reactions take place in the steel autoclaves at high temperature and pressure with organic solvents [19]. Solvothermal synthesis is a low cost method to produce high quality crystalline platelets, allows to control the size and the shape of the plates by changing solvent type, temperature, reaction time and precursor type. The disadvantages of solvothermal synthesis is that as-synthesized particles are coated with an amorphous layer, due to the use of the organic solvents. This amorphous layer on the surface of the particles acts as a barrier in some applications, where the direct contact between the Bi_2Se_3 and other material is required (e.g. spintronic devices).

To overcome this problem, in this article we demonstrate, for the first time, that high quality Bi_2Se_3 plates can be obtained by an hydrothermal

method [20]. The new technique consist of a solvent free procedure similar to that used during the solvothermal sythesis. The synthesized Bi_2Se_3 plates were characterized using x-ray diffraction (XRD), scanning electron micropscopy (SEM) with energy-dispersive x-ray spectroscopy and transmission electron micorscopy (TEM). No signature of organic coating was found on the surface of Bi_2Se_3 plates prepared by hydrothermal method. The tuning of the particles size has been obtianed by changing the concentration of reducing agent and the duration of reaction [19].

2. Experimental details

In order to compare the two different methods, Bi_2Se_3 plates were prepared with both solvothermal and hydrothermal methods.

For the preparation of Bi_2Se_3 plates with solvothermal method, 0.5 mmol of bismuth oxide (Bi_2O_3), 1.5 mmol of selenium (Se), 0.02 mmol of polyvinylpyrrolidone (PVP) and 4 mmol of sodium hydroxide (NaOH) were dissolved in 20 ml of ethylenglycol $(CH_2OH)_2$ and mixed. After one hour of mixing, the obtained slury was transfered and sealed in a teflon lined autoclave and heated to 200^o C for 10 h. After the reaction was completed, the suspension has been washed for five times with H_2O in a centrifuge at 7600 rpm for 15 mins. The suspended particles have been dried and prepared for further characterization.

For the hydrothermal synthesis of Bi_2Se_3 particles, we used the same experimental procedure as in the case of solvothermal synthesis, except that instead of Bi_2O_3 we used bismuth III nitrate pentahydrate ($Bi(NO_2)_3 \times 5H_2O$) of 0.61 mmol. To maintain the reductive conditions, the hydrazine (N_2H_4) was added (0.8 ml or 1.6 ml) with 0.026 ml of hydrochloric acid (HCl). The slury was then sealed in the teflon lined autoclave and heated to 200^o C for different time period, varying from 24 h to 48 h, except in the case of synthesis where we added 1.6 ml of N_2H_4, where the reaction was prolonged to 72 h.

$(CH_2OH)_2$ was purchased from Fisher BioReagents, HCl was purchased from Sigma Aldrich wheareas Bi_2O_3, Se, NaOH, PVP, $Bi(NO_2)_3 \times 5H_2O$, N_2H_4 were purchased from Alfa Aesar and used without further purification.

The synthesized Bi_2Se_3 plates were characterized using XRD (Rigaku Miniflex600 XRD Instrument), SEM with EDXS (Jeol SSM-7100 F) and TEM (JEM 2100-F).

3. Results and discussion

The comparison of the morphology and chemical composition of the synthesized particles by solvothermal and hydrothermal methods is done with SEM (Fig. 1) and EDXS.

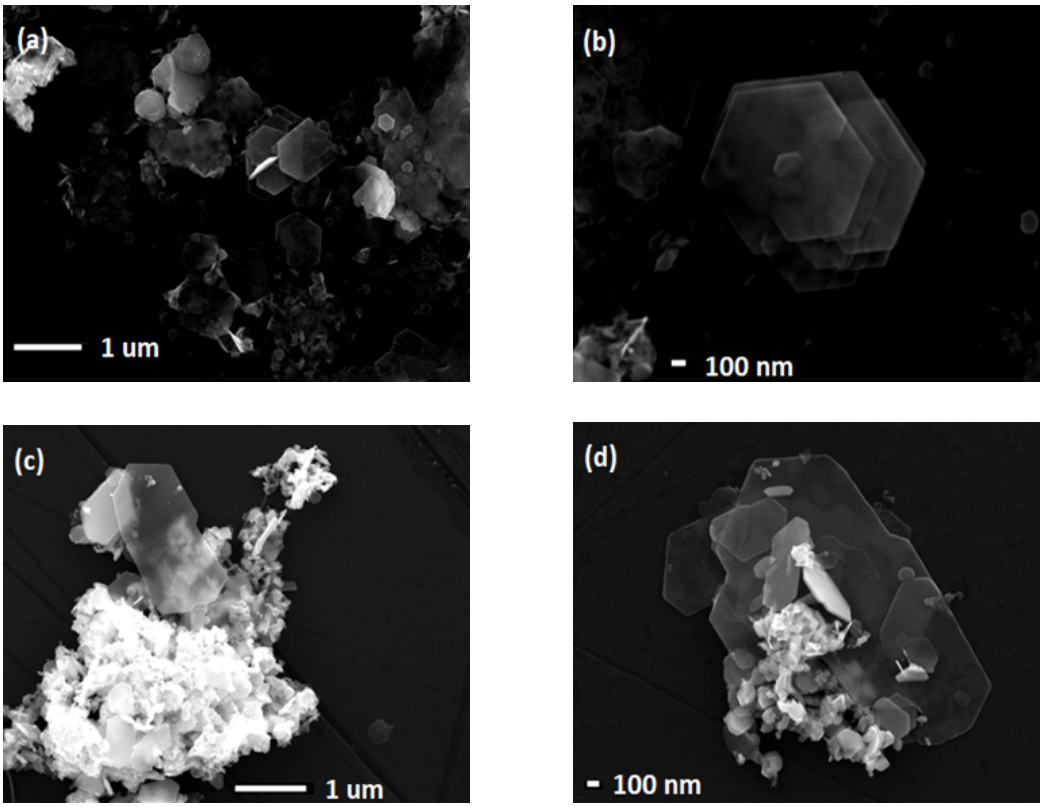

Figure 1: SEM images of Bi_2Se_3 plates at low magnification and high magnification, prepared by (a)-(b) solvothermal method at 200^0 C/10 h and (c)-(d) hydrothermal method at 200^0 C/42 h with 1.6 ml of N_2H_4 respectively.

The analysis reveals that particles prepared with both methods are hexagonal and are assembled in spherical agglomerate. The EDXS analysis on a hexagonal plate prepared by solvothermal and hydrothermal methods shows the presence of Bi and Se in an atomic percentage ratio $39.3 \pm 2.4 : 60.7 \pm 1.4$ and $40.4 \pm 0.3 : 59.6 \pm 0.3$ respectively, which corresponds to the expected stoichiometric ratio of Bi_2Se_3. In addition to hexagonal plates there are spherical particles, whose composition will be discussed below.

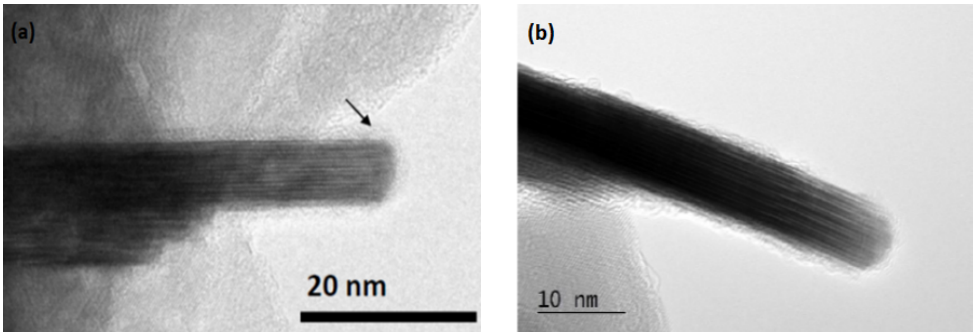

Figure 2: TEM images of Bi_2Se_3 plates prepared by (a) solvothermal method at 200^0 C/10 h and (b) hydrothermal method at 200^0 C/24 h with 0.8 ml of N_2H_4.

More detailed information about the structure of the Bi_2Se_3 particles has been obtained by TEM characterization. Fig. 2 (a) reports the structure of a Bi_2Se_3 plate obtained by solvothermal method. The particle is oriented with its crystallographic c-axis perpendicular to the electron beam, and the arrow indicates the presence of a thin amorphous layer. This layer is attributed to a coating of an organic layer as a results of the use of solvents during the solvothermal synthesis. Whereas for the particle prepared by hydrothermal method (Fig. 2 (b)), the particles are crystalline, but the coating of amorphous layer is not observed. SEM with EDXS and TEM measurements demonstrate that crystalline Bi_2Se_3 plates, having the correct chemical composition, can be obtained with both solvothermal and hydrothermal methods. In the case of hydrothermal sythesis the particles do not show any additional coating as is the case of solvothermal sythesis.

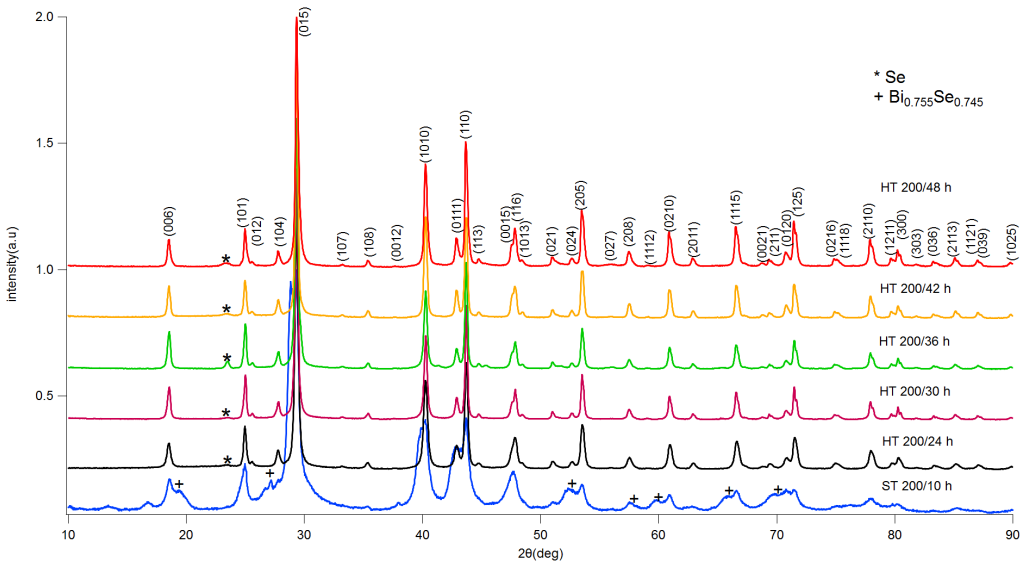

Figure 3: XRD spectra of Bi_2Se_3 particles prepared by hydrothermal method at 200^0 C using solvothermal method (ST) and hydrothermal method (HT), after different reaction time where addition of the N_2H_4 was 0.8 ml.

To gain an insight about the role played by the reaction time and amount of reducing agent during the hydrothermal reaction, different samples were systematically prepared and characterized. In Fig. 3 are reported the XRD specra of the samples prepared by hydrothermal (denoted by HT) method by varing the reaction time and keeping the amount of N_2H_4 constant at 0.8 ml and the reaction temperature at T=200^0 C . As a term of comparison, in the same figure, the XRD spectrum measured on sample prepared with solvothermal method (denoted by ST) is included. The XRD pattern of the samples prepared by solvothermal method reveals that the peaks corresponds to the structure of Bi_2Se_3. However, in addition to the peaks expected for pure crystalline Bi_2Se_3 (Card No.9011965), there are additional peaks (denoted by +) which are indexed according to the structure of $Bi_{0\cdot755}$ $Se_{0\cdot745}$ (Card No.9012066). The presence of these extra peaks are due to an incomplete reaction between the Bi and Se during the formation of Bi_2Se_3. The XRD pattern of samples prepared by hydrothermal method also reveals the peaks that correspond to the structure of Bi_2Se_3. However, there are also additional peaks (denoted by *) that can be ascribed to the structure of Se (Card No.9008581). The peaks of Se are always present independently from

the reaction time. The Se in these samples is most probably due to a low amount of N_2H_4, which is required to reduce Se^0 to Se^{2-} [20]. Moreover, the presence of concetrated HCl also reduces the activity of the N_2H_4 [19]. The unreacted Se is visible in the SEM images in the form of spherical particles (see Fig. 4 (a)) and has been confirmed by EDXS measurements done on that structures. In order to reduce the quantity of non-reacted Se, the amount of N_2H_4 was increased from 0.8 ml to 1.6 ml in a second batch of samples prepared with hydrothermal method (see EXPERIMENTAL DETAILS).

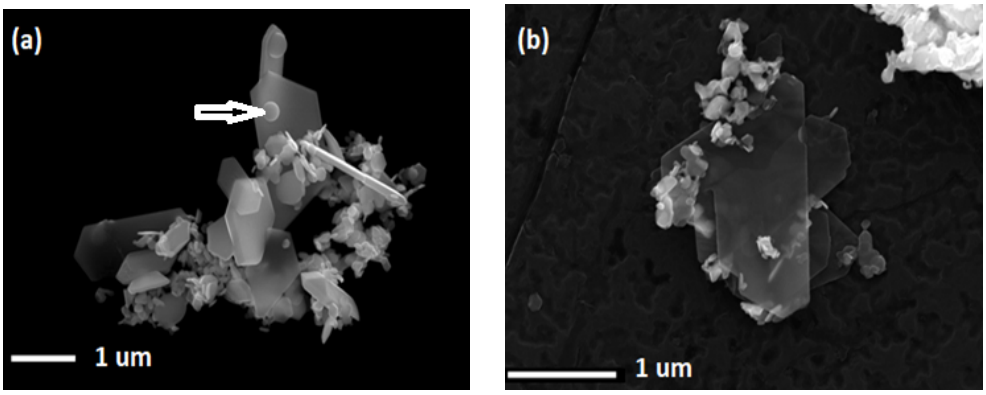

Figure 4: The SEM images of Bi_2Se_3 plates prepared by hydrothermal method at 200^0 C/42 h (a) with 0.8 ml of N_2H4 (b) with 1.6 ml of N_2H_4.

The increase of N_2H_4 resulted to be beneficial for the complete reaction of Se. SEM image (see Fig. 4 (b)) shows only hexagonal plates, no spherical particles are visible and the EDXS measured on hexagonal plates confirms to be pure Bi_2Se_3 plate.

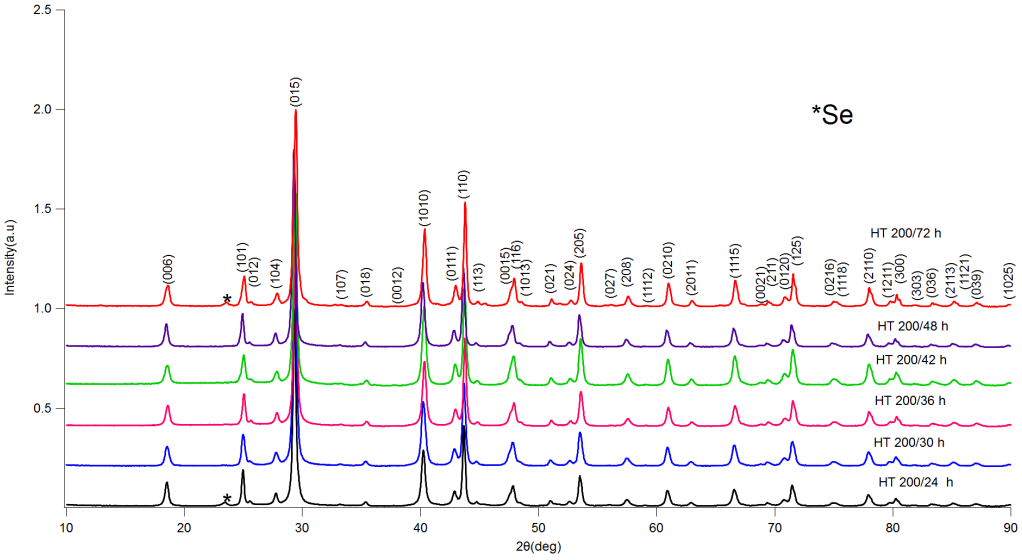

Figure 5: XRD spectra of Bi_2Se_3 particles prepared by hydrothermal method at 200 C after different time of reaction with addition of 1.6 ml of N_2H_4.

The results obtained with SEM are confirmed by XRD measurements reported in Fig. 5. The XRD pattern of the samples prepared by hydrothermal method with an increased amount of N_2H_4 (Fig. 5) clearly shows the presence of the peaks that correspond to the structure of Bi_2Se_3. However, the additional peaks (denoted by *) ascribed to Se are present on the samples obtained after 24 h and 72 h of reaction. In the first case Se is most probably present beacuse of a too short reaction time, while in the second case because of an insufficient amount of N_2H_4 for such long reaction time. These observations, together with the SEM analysis with EDXS, clearly shows that an increased amount of N_2H_4 is necessary for the complete reaction of Se and a good compromise between reaction time and quantity of reducting agent must be found in order to obtain pure crystalline Bi_2Se_3 particles.

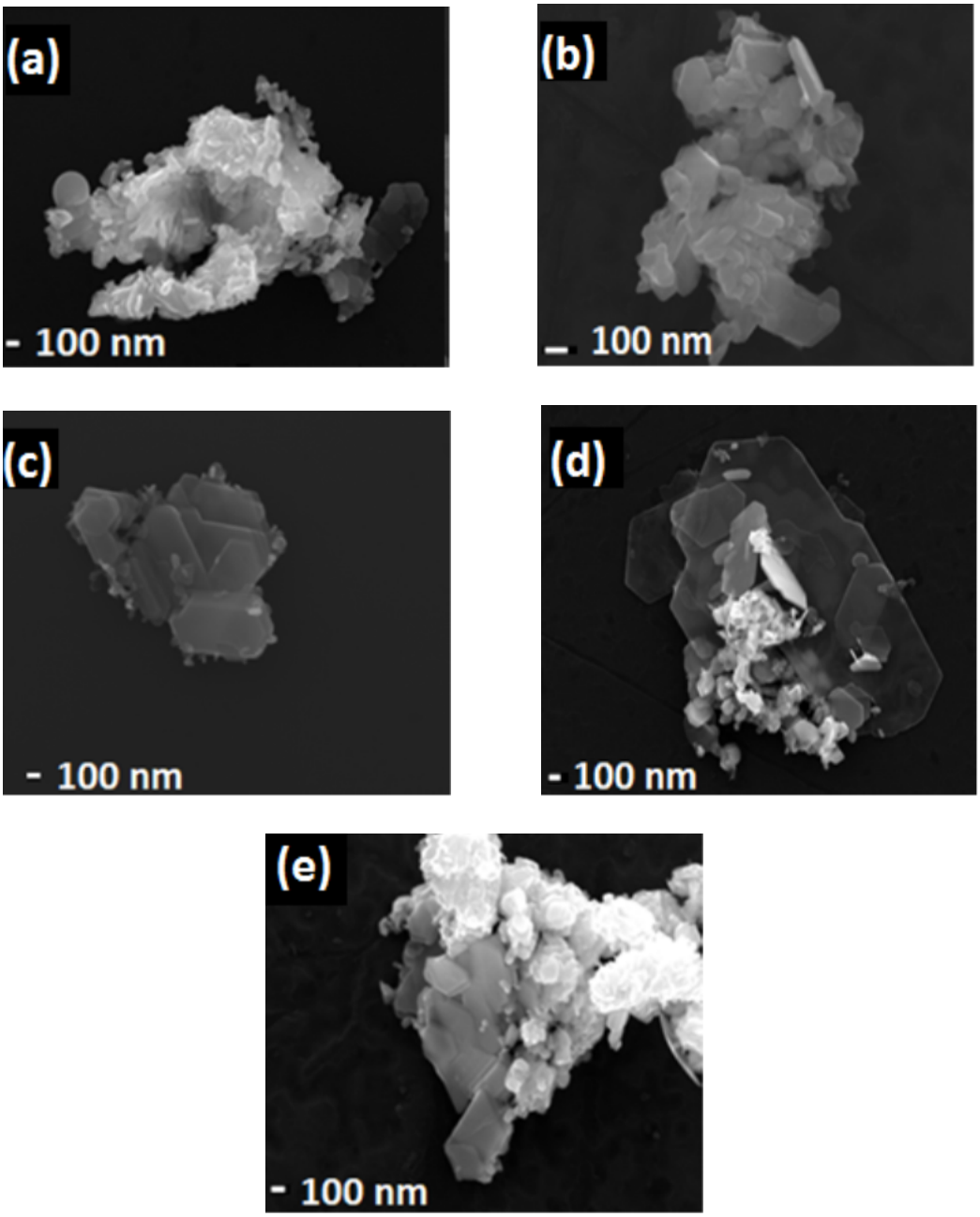

Figure 6: The SEM images of Bi_2Se_3 plates prepared by hydrothermal method with 1.6 ml of N_2H_4 at 200^0 C after (a) 24 h (b) 30 h (c) 36 h (d) 42 h and (e) 48 h of reaction time.

In Fig. 6 are reported the SEM images of the particles prepared by hydrothermal method with 1.6 ml of N_2H_4 after different reaction time. At 24 h of reaction the diameter of the particles is less than 100 nm, as the reaction time increases the diameter of the particles increases. After 42 h of reaction the larger plates are observed to be $\sim$ 500 nm in diameter. From the observation of SEM image it is evident that the size of the plate increases with respect to an increase in the reaction time.

4. Conclusion

With the results reported here we demonstrated, for the first time, that crystalline Bi_2Se_3 plates can be prepared by means of hydrothermal method. SEM with EDXS,TEM and XRD characterizations confirm that the crystalline Bi_2Se_3 plates obtained with hydrothermal method are very similar to that produced with solvothermal method, but without any additional coating on their surface. An increased amount of N_2H_4 (0.8 ml to 1.6 ml) and an optimal reaction time, have been demonstrated to be beneficial for the complete Se consumption during the hydrothermal sythesis. The increase in reaction time results in an increase of the size of the Bi_2Se_3 plates, which is from less than 100 nm up to $\sim$ 500 nm in diameter. The knowledge gained about the new synthesis method for the preparation of Bi_2Se_3 particles, with tunable diameter size, is of great importance for the realization of TI based devices which require a cheap production method, the direct contact between Bi_2Se_3 and the other materials, the exploitation of electronic properties that depends on the size of Bi_2Se_3 particles such as minimized bulk conduction and scattering caused by natural defects and/or band gap enhancement by quantum size effects.

References

[1] R. J. Cava et al. *Crystal structure and chemistry of topological insulators*, J. Mater. Chem. C, vol.1,no. 19, p. 3176,**2013**.

[2] K. Kadel et al. *Synthesis and Thermoelectric Properties of Bi_2Se_3 Nanostructures*, Nanoscale Res Lett,6:57,pp. 17, **2013**.

[3] S. K. Mishra et al. *Electronic structure and thermoelectric properties of bismuth telluride and bismuth selenide*, J. Physics-Condensed Matter, vol. 9, no. 2, pp. 461470, **1997**.

[4] N. Xu et al. *Topological insulators for thermoelectrics*, npj Quantum Mater., vol. 2, no. 1, p. 51, **2017**.

[5] S. Augustine et al. *Structural, electrical and optical properties of Bi_2Se_3 and $Bi_2Se_{(3-x)}Te_x$ thin films*, Mater. Res. Bull., vol. 40, no. 8, pp. 13141325 ,**2005**.

[6] X. Yang et al. *Synthesis and optical properties of single-crystalline bismuth selenide nanorods via a convenient route*, J. Cryst. Growth, vol. 276, no. 34, pp. 566570, **2005**.

[7] W. Tian et al. *The property, preparation and application of topological insulators: A review*, Materials (Basel)., vol. 10, no. 7, **2017**.

[8] J. Li et al. *Single crystal growth and transport properties of Cu-doped topological insulator Bi_2Se_3*, Phys. Procedia, vol. 36, pp. 638643, **2012**.

[9] M. P. Deshpande et al. *Transport property measurements of Bi_2Se_3 crystal grown by Bridgman method*, Turk J Phys, vol. 33, pp. 139148, **2009**.

[10] O. Chiatti et al. *2D layered transport properties from topological insulator Bi_2Se_3 single crystals and micro flakes*,Sci. Rep., vol. 6, no. 1, p. 27483, **2016**.

[11] Z. Dingi et al. *Lithium intercalation and exfoliation of layered bismuth selenide and bismuth telluride*,J. Mater. Chem., vol. 19, no. 17, p. 2588, **2009**.

[12] J. R. Brent et al. *Synthetic approaches to two-dimensional transition metal dichalcogenide nanosheets*,Prog. Mater. Sci., vol. 89, pp. 411478, **2017**.

[13] H. S. S. Ramakrishna Matte et al. *Graphene analogues of layered metal selenides*,Dalton Trans., 40, 10322, **2011**.

[14] O. Neill et al. *Preparation of High Concentration Dispersions of Exfoliated MoS_2 with Increased Flake Size*,J. Mater. Chem. Chem. Mater. Coleman al. Sci., vol. 22, no. 24, pp. 1761917624, **2012**.

[15] M. Liu et al. *Multi-layered nanostructure Bi_2Se_3 grown by chemical vapor deposition in selenium-rich atmosphere*,Appl. Surf. Sci., vol. 317, pp. 257261, **2014**.

[16] J. Y. Park et al. *Topological insulator Bi_2Te_3 films synthesized by metal organic chemical vapor deposition*,Appl. Phys. Lett., vol. 101, no. 16, p. 162104, **2012**.

[17] J. Y. Park et al. *Molecular beam epitaxial growth and electronic transport properties of high quality topological insulator Bi_2Se_3 thin films on hexagonal boron nitride*,2D Mater., vol. 3, no. 3, p. 035029, **2016**.

[18] T. Ginley et al. *Topological Insulator Film Growth by Molecular Beam Epitaxy: A Review*, Crystals, vol. 6, no. 11, p. 154, **2016**.

[19] X. Liu et al. *One-pot synthesis of Bi_2Se_3 nanostructures with rationally tunable morphologies*,Nano Res., vol. 8, no. 11, pp. 36123620, **2015**.

[20] J. R. Ota et al. *A simple hydrothermal method for the growth of Bi_2Se_3 nanorods*,Nanotechnology, vol. 17, no. 6, pp. 17001705, **2006**.

SIMPLE AND FAST HPLC-DAD METHOD FOR DETERMINATION OF HYDROXYCINNAMATE DECARBOXYLASE ACTIVITY AND FORMATION OF VINYLPHENOL IN *SACCHAROMYCES* AND NON-*SACCHAROMYCES* YEAST.

***Topić Jelena*[1], *Butinar Lorena*[2], *Dorota Korte*[1], *Branka Mozetič Vodopivec*[2]**

[1]*Laboratory for Environmental and Life Sciences, University of Nova Gorica, Vipavska 13, Nova Gorica, Slovenia*

[2]*Wine Research Centre, University of Nova Gorica, Glavni trg 8, Vipava, Slovenia*

jelena.topic@ung.si

Abstract

Although in production of yeast species *Saccharomyces cerevisiae* are usually used, other yeast species are being investigated in terms of using them for improvement of wine aroma and colour. Colour of the wine can be affected with the usage of yeast with high hydroxycinnamate decarboxylase activity. 96 different yeast strains belonging to 27 species were selected for the assessment of HCDC activity. In some cases the difference in *p*-coumaric acid metabolism rate between two strains exceeded 70%. Saccharomyces paradoxus strains showed more than 40% conversion rate. Strains with the highest HCDC activity were two *Pichia guillermondii* strains. The results showed that HCDC activity is highly strain dependent. The proposed method is very simple and does not require special sample preparation prior to HPLC analysis. Furthermore, the proposed fermentations in deep well microtiter plates allow the screening of high number of strains. The method could be used for routine screening, to determine which strain has high HCDC activity and produces high concentration of vinylphenols and can therefore be used in future for determination of strains ability to synthesize vinylphenolic pyranoanthocyanins.

Key words: *yeast, hydroxycinnamate decarboxylase, 4-vinylphenol, 4-ethylphenol, p-coumaric acid*

1. INTRODUCTION

Conventionally, alcoholic fermentation in the production of wine is performed by yeast species *Saccharomyces cerevisiae*. There are numerous starters available, however because of the growing demand for wines with specific characteristics, other Saccharomyces and non-Saccharomyces species are being investigated for potential use as starters (Masneuf-Pomarede et al. 2016). Yeast selection has involved the development of techniques for detecting strains that might improve wines in terms of aroma, structure, colour and other technological properties (Suárez-Lepe and Morata 2012). Colour of the wine can be affected is colour as some metabolites produced by yeast during fermentation may react with grape anthocyanins to produce highly stable pyranoanthocyanins such as vitisin A and vitisin B. Formation of stable pyranoanthocyanins is desirable as the wines are less susceptible to gradual colour loss with the wine ageing. Furthermore, they are less susceptible to the loss of colour after the addition of SO_2, which is used as antimicrobial agent (Antonio Morata et al. 2016). Similar to vitisins, vinylphenolic pyranoanthocyanin adducts also show great colour stability (Antonio Morata, González, and Suárez-Lepe 2007; Benito et al. 2011). As vinylphenols act as precursors of ethylphenols in wines, which are considered off-smells and are undesirable because they degrade the quality of wine, formation of vinylphenolic pyranoanthocyanins during fermentation can provide a natural way of preventing or reducing possible ethylphenol precursors in wine (Antonio Morata, Loira, and Suárez Lepe 2016). The pathway of vinylphenolic pyranoanthocyanins formation is presented in the Figure 1.

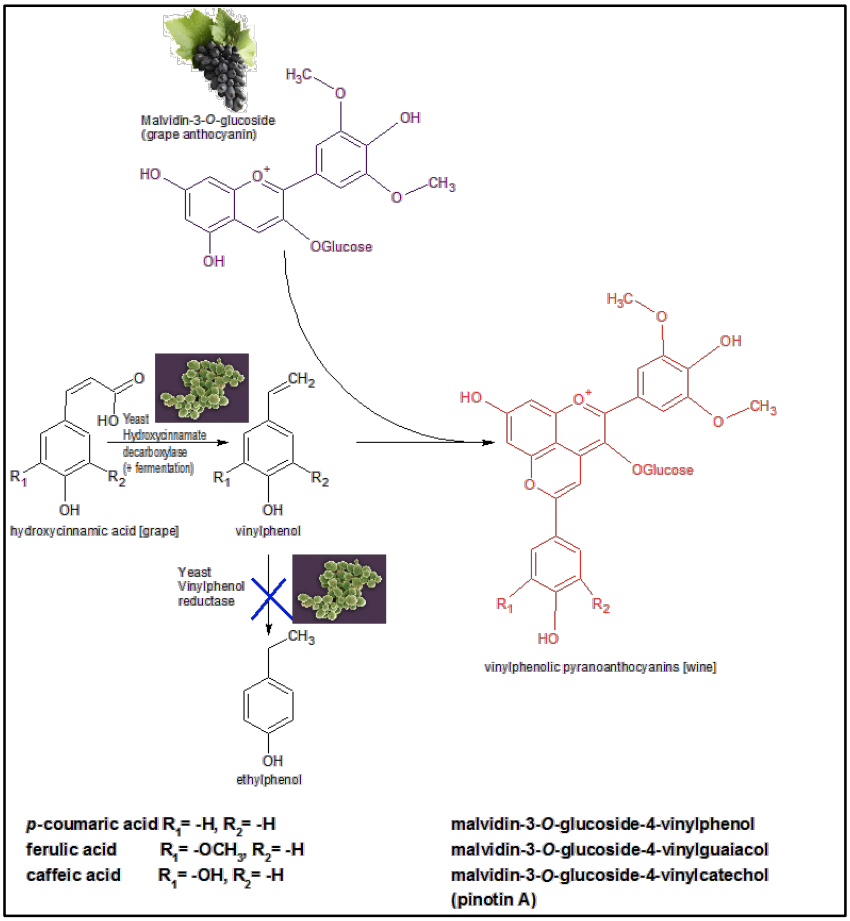

Figure 1: Vinylphenolic pyranoanthocyanins pathway formation.

For the facilitation of formation of vinylphenolic pyranoanthocyanins, yeast strains with high hydroxycinnamate decarboxylase (HCDC) activity are used. The mechanism of reaction is decarboxylation of hydroxycinnamic acids and formation of vinylphenols that condense with grape anthocyanins and form stable vinyphenolic pyranoanthocyanin adducts (Figure 1). (Escott et al. 2016). It has been demonstrated that some non-*Saccharomyces* strains (*Pichia guillermondii*, *Schizosaccharomyces pombe*) have positive HCDC activity and that they can produce vinylphenolic pyranoanthocyanins in higher concentrations than *S. cerevisiae*. When non-*Saccharomyces* strains are used for the must fermentation, they should be used with *Saccharomyces* strains either in the form of co-fermentation or sequential fermentation as non-*Saccharomyces* strains cannot finish fermentation by themselves as they are sensitive to ethanol content (Benito et al. 2011; Antonio Morata et al. 2016).

A simple way of determining whether the yeast strain has HCDC activity or not, is the use of media with the addition of hydroxycinnamic acids, such as *p*-coumaric acid. The degradation of *p*-coumaric acid and transformation into 4-vinylphenol (and possibly in 4-ethylphenol) can be checked by LC-DAD (Benito, Palomero, Morata, Calderón, et al. 2009). HCDC active yeast strain transforms hydroxycinnamic acids into vinylphenols and later a vinylphenol reductase enzyme induces the reduction of vinylphenols in ethylphenols.The pathway of 4-vinylphenol (and 4-ethylphenol) formation from *p*-coumaric acid is presented in the Figure 2.

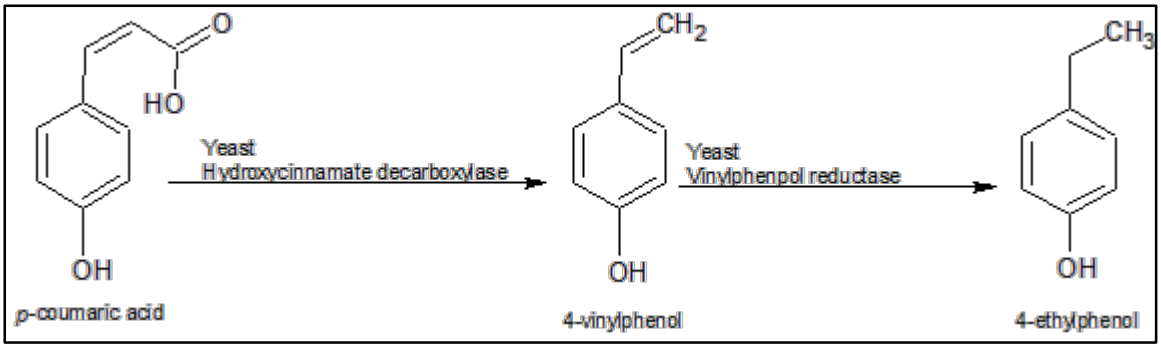

Figure 2: *Formation of 4-vinylphenol and 4-ethylphenol from p-coumaric acid.. The biosynthesis of volatile phenols is related to the activity of two enzymes. First step is decarboxyalation of p-coumaric acid which is catalyzed by hydroxycinnamate decarboxylase enzyme. The second step occurs if the strain has vinylphenol reductase activity which catalyzes the reduction of 4-vinylphenol into 4-ethylphenol.*

The yeast strain can be considered HCDC positive, when it transform more than 10% of *p*-coumaric acid into 4-vinyphenol. The greater the degradation of *p*-coumaric acid and resulting formation of 4-vinylphenol is, the higher HCDC activity of the yeast. Subsequently yeast with high HCDC activity are expected to form higher concentrations of vinylphenolic pyranoanthocyanins during fermentation of must (Antonio Morata, Loira, and Suárez Lepe 2016).

Morata et al. (A. Morata et al. 2013) tested 12 commercial *S. cerevisiae* strains for HCDC activity and degradation rate ranged from 60 – 99%. Furthermore, the activity of four experimental strains isolated ranged from 60-80%. Benito et al. measured the HCDC activity of two *S. cerevisiae* strains and strains *Dekkera bruxellensis, Pichia membranifaciens*, and *Candida pulcherrima* strain. The obtained results showed that only *D. bruxellensis* and *S. cerevisiae* 7V were able to transform *p*-coumaric acid. *D. bruxellensis* metabolized nearly all of *p*-coumaric acid, while S. cerevisiae 7V transformed 15%. Both strains were able to produce 4-vinylphenol, however only *D. bruxellensis* produced significant amounts of 4-ethylphenol (Benito, Palomero, Morata, Calderón, et al. 2009). Ecribano et al. tested 97 non-Saccharomyces wine yeast strains belonging to 10 different genera for HCDC activity. The detection was performed on yeast-peptose-dextrose (YPD) plates, and HCDC positive strains were detected by a colour shift of the media from yellow to purple due to the alkalization of media. Of all the strains tested only 50% of *Metschnikowia pulcherrima* strains were positive, while *P. kluyveri, Torulaspora delbrueckii, Lachancea thermotolerans, Debaromyces hanseniii* and *Candida* spp. strains did not present HCDC activity. No data was provided about the *p*-coumaric transformation rate and 4-vinyl phenol and 4-ethyl phenol production (Escribano et al. 2017).

The aim of our work was to develop simple method for the screening of Slovenian in-house yeast collection, comprising of native isolates that mostly originated from Vipava valley and Karst region, and therefore try to determine strains with high HCDC activity. These strains can be used for wine fermentations in order to produce more stable pyranoanthocyanins; which is especially important in wines that has less anthocyanin concentration already from the grape, such as Pinot Noir.

2. MATERIALS AND METHODS

Yeast strains and fermentation media

96 different yeast strains belonging to 27 species were selected for the assessment of HCDC activity. Selected species were taken from Wine Research Centre of University of Nova Gorica (Vipava, Slovenia) yeast collection and Collection of Industrial Microorganisms (ZIM) (Biotechnical Faculty, University of Ljubljana, Slovenia). Two commercial *S. cerevisiae* strains were also tested – Fermol Premier Cru (FPC) (AEB Group) and Lalvin EC1118 (Lallemand, Canada). Strains chosen for this experiments and their origin are presented in the Supplementary Information (Table S1).

Yeast strains were stored at -80 °C in 15% glycerol and were streaked on Wallerstein-Lab (WL) plates and incubated for 48h at 25 °C. Single colonies were used to inoculate 3 mL of yeast-peptone-dextrose (YPD) media in 15 mL sterile centrifuge tubes. Precultures were incubated for 24h at 25 °C with shaking at 250 rpm. The growth of yeast cultures was checked with measuring the absorbance at 600 nm (OD600). OD600 of yeast cultures was adjusted to OD600=1 with 0.85% sterile saline solution, if necessary. The fermentation media used was composed of 0.67% (w/v) commercial yeast nitrogen base (YNB) media with $(NH_4)_2SO_4$, 2% glucose (w/v) and 100 ppm of *p*-coumaric acid dissolved in double distilled water and filtered through 0.2 µm PES filter.

To the deep well microtiter plate 1.35 mL fermentation media was added. The media was inoculated with 150 µL of yeast culture (OD600=1), to achieve final OD=0.1. The deep well plate was covered with sterile cover to prevent evaporation during fermentation. Fermentations spanned for 10 days and were done in four replicates.

Detection of p-coumaric acid, 4-vinylphenol and 4-ethylphenol by high performance liquid chromatography with photodiode array detection (HPLC-DAD)

The compounds were analysed using Agilent Technologies 1100 (Palo Alto, California, USA) HPLC chromatograph equipped with a quaternary pump, an autosampler and photo-diode array detector. Isocratic elution of mobile phase A (0.2% trifluoroacetic acid in water) and mobile phase B (0.2% trifluoroacetic acid in methanol) was used in the ratio 80/20 (mobile phase A/ mobile phase B). The column used for separation was reverse-phase Phenomenex Luna C_{18} PFP (250x4.6 mm, 5 µm i.d.) with matching guard column. Wavelengths used for detection were 320 nm, 280 nm and 260 nm. Time of analysis was 15 min. Quantification was performed by comparison of external standard at 320 nm (*p*-coumaric acid), 280 nm (4-ethylphenol) and 260 nm (4-vinylphenol).

Samples were centrifuged after the end of fermentation for 10 min at 6000 rpm. The supernatant was analysed on HPLC-DAD. The injection volume was 40 µL.

3. RESULTS AND DISCUSSION

Detection and quantification of p-coumaric acid, 4-vinylphenol and 4-ethylphenol

Figure 3 shows chromatogram of *p*-coumaric acid, 4-vinylphenol and 4-ethylphenol and the wavelengths used for their detection and quantification. Usage of deep-well microtiter plates for fermentations and short time of analysis needed for each sample (15 min) allowed for the testing of high number of strains. The proposed HPLC-DAD method in combination with microtiter deep-well plates is applicable as screening method for selection of strains with high HCDC activity that could be potentially used as starters. HCDC activity was expressed as the ratio of p-coumaric acid concentration of the strain at the end of fermentation and p-coumaric acid concentration in the control sample. Limit of detection (LOD) was calculated as the ratio

between 3xSTDEV of the blank sample and slope of the regression curve. Limit of quantification (LOQ) was calculated as the ratio between between 10xSTDEV of the blank sample and slope of the calibration curve. Information about calibration curve, coefficient of multiple determination (R2), LODs and LOQs are presented in the table 1.

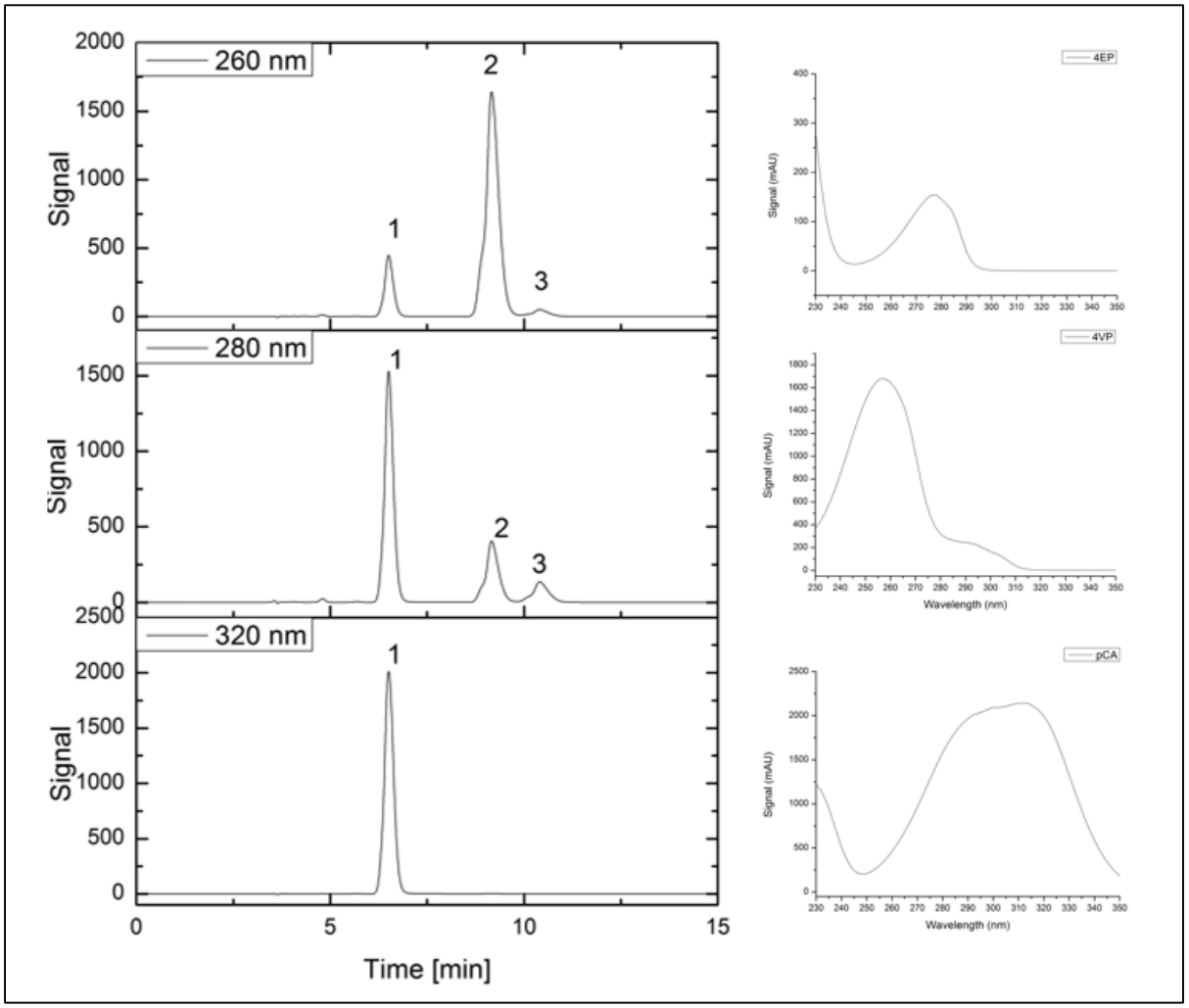

Figure 3: *Chromatogram of 4-ethylphenol (3), 4-vinylphenol (2) and p-coumaric acid (1) with their spectrums. 4-EP (4-ethylphenol) λ_{max} = 260 nm; 4-VP (4-vinylphenol) λ_{max} = 280 nm, p-CA (p-coumaric acid) λ_{max} = 320 nm.*

Table 1: Calibration parameters for p-coumaric acid, 4-vinylphenol and 4-ethylphenol.

Compound	Detection wavelength [nm]	Calibration curve	R^2	LOD [ppb]	LOQ [ppb]
p-coumaric acid	320	y=223.41x + 87.207	0.9996	20	50
4-vinylphenol	260	y=238.77x + 542.48	0.9989	50	180
4-ethylphenol	280	y= 26.059x + 5.8728	0.9998	160	700

HCDC activity of tested yeast strains

In Table 2, HCDC activity of tested strains is presented. HCDC activity of yeast strains was expressed as p-coumaric acid conversion rate. The results show that HCDC activity varies greatly within species.

Table 2: HCDC activity of tested yeast strains.

Genus	Species	N°strains tested	TR [%] (average)
Torulaspora	*T. delbrueckii*	8	0.8 – 72.2 (19.7)
Starmella	*S. bacillaris*	2	13.1-16.0 (14.5)
Saccharomyces	*S. servazii*	1	0.7
	S. paradoxus	10	40.6-66.6 (50.4)
	S. kudriavzevii	6	2.6-9.1 (6.8)
	S. cerevisiae	17	5.1-66.0 (31.7)
	S. bayanus	2	27.0-30.9 (28.9)
Pichia	*P. sp*	1	8.4
	P. membranifaciens	3	7.2-20.6 (12.6)
	P. manshurica	4	0-66.9 (26.0)
	P. kudriavzevii	1	0
	P. kluyveri	5	1.0-19.4 (13.4)
	P. guillermondii	2	88.5-88.7 (88.6)
	P. anomala	1	9.9
Metschnikowia	*M. pulcherrima*	6	12.9-23.9 (19.2)
	M. fructola	1	1.7
	M. reukafii	1	86
Lachancea	*L. thermotolerans*	4	0-16.2 (9.8)
Kregervanrija	*K. fluxum*	1	29.1
Kluyveromyces	*K. dobzhanskii*	1	0
Issatchenkia	*I. terricola*	1	11.8-22.6 (17.2)
Hanseniaspora	*H. uvarum*	10	0-99.9 (19.7)
	H. osmophilia	1	3.1
Debaromyces	*D. hansenii*	3	16.8-41.3(27.3)
Candida	*C. sake*	1	1.6
	C. rugosa	1	18.2
	C. diversa	1	17.2

Of the tested 96 strains, 72.9% of them were HCDC positive, as they transformed more than 10% of *p*-coumaric acid. It was observed that HCDC activity is strain dependent, as in some cases the difference in *p*-coumaric acid metabolism rate between two strains exceeded 70% (Table 1). HCDC activity of *S. cerevisiae* strains which is the species most commonly used in fermentation, varied between 5.1 and 66.1%. Commercial strains tested, FPC and EC118 showed 43.9 and 21.5% degradation rate, respectively. It was observed that some native strains had higher HCDC activity than commercial ones, with strain ZIM2180 showing the highest HCDC activity among tested *S. cerevisiae strains* (66.0%). Benito et al. (2011) tested 16 *S. cerevisiae* strain and the *p*-coumaric acid conversion rate varied, with only three strains

able to convert more than 50% of *p*-coumaric acid (Benito et al., 2009b, 2011b), however published data from Morata et al. showed high HCDC activity of tested *S. cerevisiae* strains, as *p*-coumaric acid transformation rate was above 60% (Morata et al., 2013). The published data also confirms that HCDC activity is strain dependent. *M. reukafii* strain tested showed high HCDC activity, however other *Metschnikowia* species tested had less than 24% conversion rate. *M. pulcherrima* strains had an average of 19.2% conversion rate. Others authors have also reported about positive HCDC activity of *M. pulcherrima* strains (Shinohara et al., 2000; Escribano et al., 2017;). Escribano et al. (2017) tested six *M. pulcherrima* strains and 50% of the tested strain showed HCDC activity, however, no data was provided about the conversion rates of *p*-coumaric acid (Escribano et al., 2017). Of the 22 strains showing more than 40% HCDC activity (Figure 4), 50% of them were *Saccharomyces paradoxus* strains, which means that all of tested *S. paradoxus* strains had HCDC activity above 40%, with Sut85 strain having the highest HCDC activity (66.6%). Other species with more than 40% HCDC activity were four strains of *S. cerevisiae* (ZIM2180, ZIM3253, Sm58RT, FPC), *T. delbrueckii* strain (ZIM2749), *D. hansenii strain* (Sut116RT), *P. manshurica* (M49) strain, *M. reukafii* (ZIM2019) and two strains of *P. guillermondii* (Ca81, ZIM624).

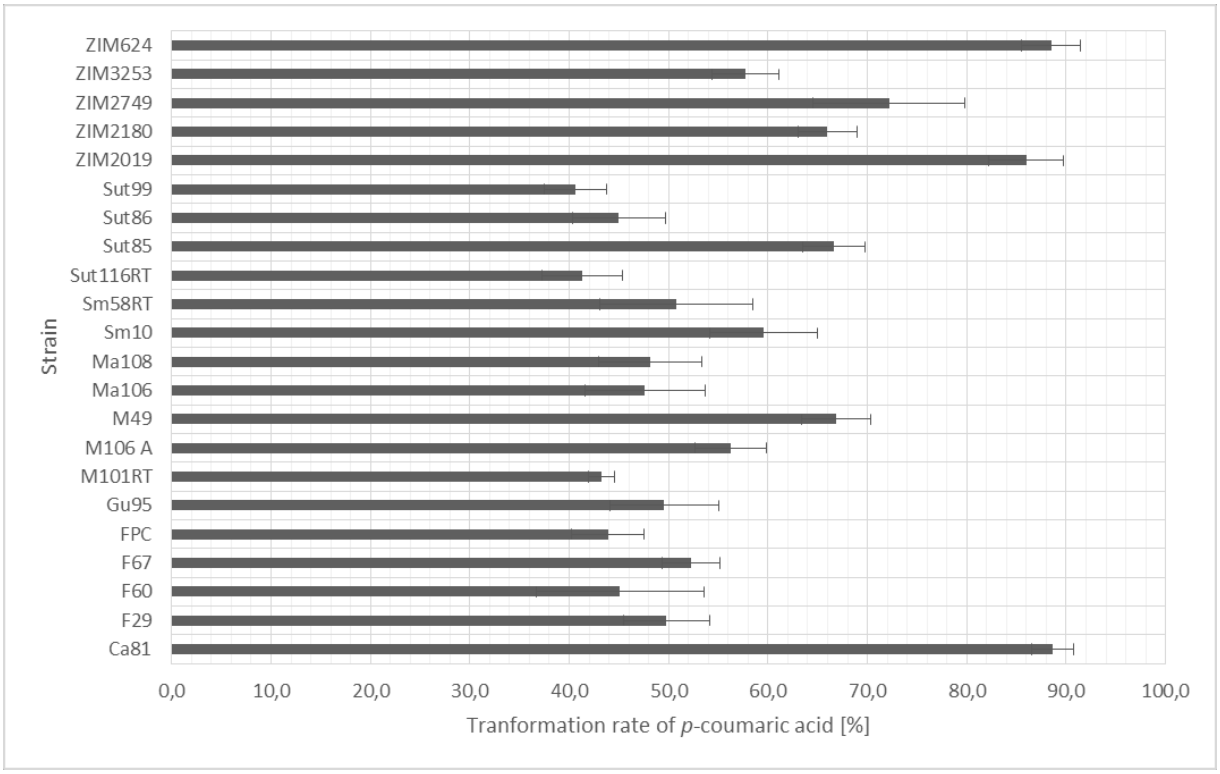

Figure 4: *Strains with HCDC activity higher than 40%. HCDC activity of yeast strain is expressed as ratio between concentration of p-coumaric acid in sample after 10 days of incubation and in control sample with RSD values added. Initial concentration was 100 ppm.*

Formation of 4-vinylphenol and 4-ethylphenol

The highest concentration of 4-vinylphenol was produced by *P. guillermondii* strains and S*. paradoxus* (Sut85) producing more than 50 ppm of 4-vinylphenol (Figure 5). *P. guillermondii* strains had also the highest conversion rate of *p*-coumaric acid. In general species with the high conversion rate of p-coumaric acid synthesized 4-vinylphenol in the highest concentrations, with the exception of strain *T. delbrueckii* ZIM2749 which although having more than 72% conversion rate of *p*-coumaric acid, synthesized only 20 ppm of 4-vinylphenol. The strains with less than 40% of HCDC activity rate synthesized less than 15 ppm of 4-

vinylphenol. The high HCDC activity could result in the formation of stable pyranoanthocyanins through a reaction between anthocyanins from grapes and vinylphenols released during fermentations through decarboxylation of hydroxycinnamic acids (Morata et al., 2007). As hydroxycinnamic acids act also as a precursors for the formation of ethylphenols by *Dekkera/Bretanomyces*, which are undesirable in wines, usage of yeast strains with high HCDC activity could thus prevent the formation of ethylphenols during aging in barrels (Benito et al., 2009b).

Two of the strains were able to synthesize 4-ethylphenol, which shows that they have also vinylphenol reductase enzyme activity. Both were *P. guilliermondii* strains (Ca81, ZIM624). They produced 15.0 and 32.1 ppm of 4-ethylphenol, respectively. Considering these results, ZIM624 had higher vinylphenol reductase enzyme activity. The *P. guillermondii* ability to produce 4-ethylphenol was previously reported in grape juices (Dias et al., 2003; Barata et al. 2006; Jensen et al., 2009). Three of the tested strains produced more than 50 mg/L of 4-ethylphenol after the addition of 100 ppm of *p*-coumaric acid (Dias et al., 2003). The same author reported also that *D. hansenii* was able to produce 4-ethylphenol, although in concentrations lower than 0.3 ppm (Dias et al., 2003). All three tested *D. hansenii* strains were HCDC positive, however only Sut116RT produced more than 15 ppm of 4-vinylphenol and none of the tested strains produced 4-ethylphenol.

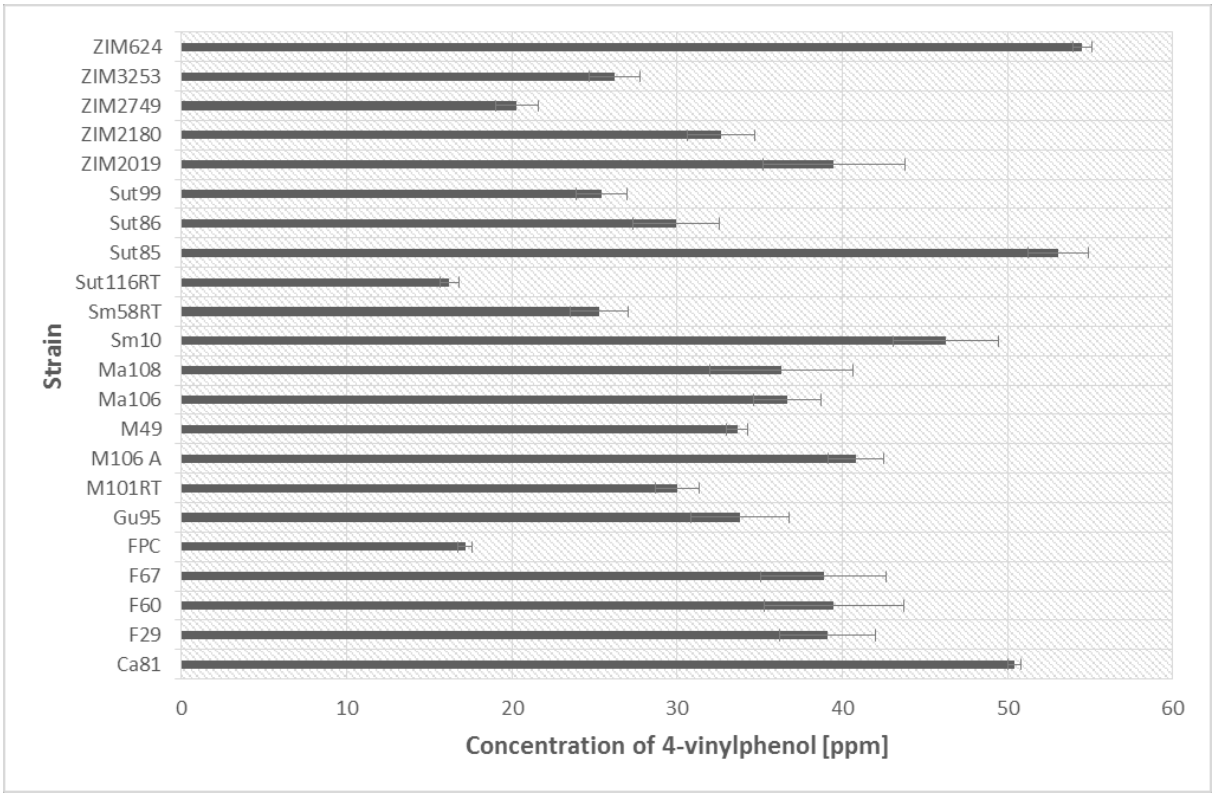

Figure 5: *The concentration of 4-vinylphenol produced after 10 days of experiment with STDEV values added.*

Concentrations of 4-vinylphenol are presented in Figure 4. Three strains produced vinylphenol in concentration higher than 50 ppm, two of them being *P. guillermondii* and another strain being *S. paradoxus* (Sut85). In general, strain with high HCDC activity also produced high concentration of 4-vinylphenol, with some exceptions. In some cases 4-vinylphenol was transformed further to 4-ethylphenol. This was the case for ZIM624 and Ca81 (*P. guilermondii*) which sysnthesized 10.5 and 11.1 ppm, respectively.

4. CONCLUSION

The proposed method with using microtiter deep well plates for fermentations allowed for testing of high number of yeast strains. Furthermore, with the use of HPLC-DAD, the information about the HCDC strain activity and the ability to form 4-vinylphenol and 4-ethylphenol was obtained. Although HCDC activity could be inspected using YEPD plates supplemented with *p*-coumaric acid it would only give us limited information about HCDC activity of yeast strains – as the test would not give information about the rate of HCDC activity of the strains and about the formation of 4-vinylphenol and 4-ethylphenol. The results showed that HCDC is highly strain dependent.

Although *S. cerevisiae* strains are commonly used for the fermentations in winemaking, several other species have been interesting to work with because with the selection of yeast, wine aroma and colour profile can be influenced. Based on the results obtained in this study, some non-*Saccharomyces* yeast could be used for fermentations. For a greater synthesis of pyranoanthocyanins yeast strains with high HCDC activity such as ZIM2794 (*T. delbrueckii*), ZIM2019 (*M. reukafii*), M49 (*P. manshurica*) and Ca81 and ZIM624 (*P. guillermondii*) can be used in co-fermentations or sequential fermentations. Furthermore, instead of using commercially available *S. cerevisiae* strains, native isolate with higher HCDC activity (ZIM2180) could be used for future fermentations. Future work will involve testing of these strain for vinylphenolic pyranoanthocyanins formation.

5. REFERENCES

Benito, S., F. Palomero, A. Morata, F. Calderón, and J.A. Suárez-Lepe. 2009. “A Method for Estimating *Dekkera/Brettanomyces* Populations in Wines.” *Journal of Applied Microbiology* 106 (5). Blackwell Publishing Ltd: 1743–51. doi:10.1111/j.1365-2672.2008.04137.x.

Benito, S, A Morata, F Palomero, M C González, and J A Suárez-Lepe. 2011. “Formation of Vinylphenolic Pyranoanthocyanins by Saccharomyces Cerevisiae and Pichia Guillermondii in Red Wines Produced Following Different Fermentation Strategies.” *Food Chemistry* 124 (1): 15–23. doi:10.1016/j.foodchem.2010.05.096.

Benito, S, F Palomero, A Morata, C Uthurry, and J A Suárez-Lepe. 2009. “Minimization of Ethylphenol Precursors in Red Wines via the Formation of Pyranoanthocyanins by Selected Yeasts.” *International Journal of Food Microbiology* 132: 145–52. doi:10.1016/j.ijfoodmicro.2009.04.015.

Escott, C., A. Morata, I. Loira, W. Tesfaye, and J.A. Suarez-Lepe. 2016. “Characterization of Polymeric Pigments and Pyranoanthocyanins Formed in Microfermentations of Non-*Saccharomyces* Yeasts.” *Journal of Applied Microbiology* 121 (5): 1346–56. doi:10.1111/jam.13255.

Escribano, Rocío, Lucía González-Arenzana, Patrocinio Garijo, Carmen Berlanas, Isabel López-Alfaro, Rosa López, Ana Rosa Gutiérrez, and Pilar Santamaría. 2017. “Screening of Enzymatic Activities within Different Enological Non-Saccharomyces Yeasts.” *Journal of Food Science and Technology* 54 (6): 1555–64. doi:10.1007/s13197-017-2587-7.

Masneuf-Pomarede, Isabelle, Marina Bely, Philippe Marullo, and Warren Albertin. 2016. “The Genetics of Non-Conventional Wine Yeasts: Current Knowledge and Future Challenges.” *Frontiers in Microbiology* 6 (JAN): 1–15. doi:10.3389/fmicb.2015.01563.

Morata, A., R. Vejarano, G. Ridolfi, S. Benito, F. Palomero, C. Uthurry, W. Tesfaye, C. González, and J.A. Suárez-Lepe. 2013. “Reduction of 4-Ethylphenol Production in Red

Wines Using HCDC+ Yeasts and Cinnamyl Esterases." *Enzyme and Microbial Technology* 52 (2). Elsevier: 99–104. doi:10.1016/J.ENZMICTEC.2012.11.001.

Morata, Antonio, Carmen González, and José Antonio Suárez-Lepe. 2007. "Formation of Vinylphenolic Pyranoanthocyanins by Selected Yeasts Fermenting Red Grape Musts Supplemented with Hydroxycinnamic Acids." *International Journal of Food Microbiology* 116 (1): 144–52. doi:10.1016/j.ijfoodmicro.2006.12.032.

Morata, Antonio, Iris Loira, José María Heras, María Jesús Callejo, Wendu Tesfaye, Carmen González, and José Antonio Suárez-Lepe. 2016. "Yeast Influence on the Formation of Stable Pigments in Red Winemaking." *Food Chemistry* 197: 686–91. doi:10.1016/j.foodchem.2015.11.026.

Morata, Antonio, Iris Loira, and Jose Antonio Suárez Lepe. 2016. "Influence of Yeasts in Wine Colour." In *Grape and Wine Biotechnology*. InTech. doi:10.5772/65055.

Suárez-Lepe, J.A., and A. Morata. 2012. "New Trends in Yeast Selection for Winemaking." *Trends in Food Science & Technology* 23 (1). Elsevier: 39–50. doi:10.1016/J.TIFS.2011.08.005.

Supplementary Information: Table S1

Table S1: *Strain designation and origin of the yeast used in this study.*

Species	Strain designation	Origin
T. delbrueckii	Sut94	Vineyard, Oak, Podraga, SI
	Ma1L	Grape, Mance, SI
	Ma10L	Vineyard, vine, Mance, SI
	Ma1D	Grape, Mance, SI
	S192	Soil, Cormons, IT
	S193	Soil, Cormons, IT
	ZIM2124	Must, Dolenjska, SI
	ZIM2794	Vineyard cellar, Brje, SI
S. bacillaris	ZIM1876	Must, Primorska, SI
	ZIM2121	Must, Dolenjska, SI
S. servazii	F48	Oak, Nanos, SI
S. paradoxus	Sut99	Vineyard, Oak, Podraga, SI
	F67	Oak, Nanos, SI
	F60	Oak, Nanos, SI
	Ma108	Vineyard, Oak, Mance, SI
	Sm10	Vineyard, Brje, SI
	Sut86	Vineyard, Oak, Podraga, SI
	Sut85	Vineyard, Oak, Podraga, SI
	Gu95	Vineyard, Oak, Planina, SI
	Ma106	Vineyard, Oak, Mance, SI
	F29	Oak, Nanos, SI
	M101RT	Grape, Dobravlje, SI
S. kudriavzevii	SV80	Oak, Sinji Vrh, SI
	Ca127	Vineyard, Oak, Goriska Brda, SI
	F45	Oak, Nanos, SI
	Sut196RT	Vineyard, Oak, Podraga, SI
	Ma101	Vineyard, Oak, Mance, SI
	M94	Vineyard, Oak, Dobravlje, SI
S. cerevisiae	FPC	Commercial (AEB)
	EC1118	Commercial (Lallemand, Canada)
	Ca39	Vineyard, Oak, Goriska Brda, SI
	Gu60RT	Vineyard, Oak, Planina, SI
	ZIM2180	Must, Institute of Agriculture, SI
	Sm76RT	Grape, Brje, SI
	Gu36	Must, Planina, SI
	Ca15	Vineyard, Oak, Goriska Brda, SI
	Sm58RT	Vineyard, Brje, SI
	Lj59RT	Vine, Lijak, SI
	Sut127	Wine, Podraga, SI
	S153	Soil, Manzano, IT
	ZIM1927	Must, Primorska, SI
	ZIM3253	Must, Planina, SI
	ZIM804	Must, Goriska Brda, SI
	Re7	Must, Dutovlje, SI
	SV21	Vineyard, Must, Guerilla, SI
	M106A	Must, Goriska Brda, SI
S. bayanus	ZIM2122	Must, Dolenjska, SI
	ZIM2114	Must, Dolenjska, SI
P. sp	Re16L	Vineyard, Dutovlje, SI

P. membranifaciens	ZIM707 S127 ZIM1908	Must, Goriska Brda, SI Grape, Gramogliano, IT Must, Primorska, SI
P. manshurica	Ma11L M49 Ca29L Sut91.2	Vineyard, Mance, SI Vineyard, Oak, Dobravlje, SI Vineyard, Oak, Goriska Brda, SI Vineyard, Oak, Podraga, SI
P. kudriavzevii	Ma40	Vineyard, Mance, SI
P. kluyveri	Sut45.1 ZIM2031 S163 S129	Vineyard, Oak, Podraga, SI Grape, Nemska Gora, SI Soil, Cero, IT Grape, Gramogliano, IT
P. guillermondii	ZIM624 Ca81	Grape, Goriska Brda, SI Vineyard, Goriska Brda, SI
P. anomala	S126	Grape, Gramogliano, IT
M. pulcherrima	ZIM2043 S118 S139 S158 S189 ZIM0722	Grape, Trska Gora, SI Grape, Manzano, IT Grape, Zuccole, IT Soil, Gramogliano, IT Soil, Cormos, IT Must, Goriska Brda, SI
M. fructola	Sut104RT	Vineyard, Oak, Podraga, SI
M. reukafii	ZIM2019	Grape, Pleterje, SI
L. thermotolerans	Gu81 S115 S132 S124	Grape, Planina, SI Grape, Manzano, IT Grape, Novacuzzo, IT Grape, Gramogliano, IT
K. fluxum	Sm66	Vineyard, Oak, Brje, SI
K. dobzhanskii	Re19L	Vineyard, Dutovlje, SI
I. terricola	ZIM1852 ZIM0691	Must, Primorska, SI Must, Goriska Brda, SI
H. uvarum	Ca147RT Lj40.2 S116 S117 S119 S120 S121 ZIM2057 ZIM1846	Vineyard, Goriska Brda, SI Grape, Lijak, SI Grape, Manzano, IT Grape, Manzano, IT Grape, Manzano, IT Grape, Manzano, IT Grape, Manzano, IT Grape, Hom, SI Must, Primorska, SI
H. osmophilia	ZIM2818	Vineyard, Podraga, SI
D. hansenii	Sut116RT ZIM717 ZIM2025	Vineyard, Cellar, Podraga, SI Must, Goriska Brda, SI Grape, Pleterje, SI
C. sake	Gu5D	Vineyard, Oak, Planina, SI
C. rugosa	ZIM1681	Must, Karst, SI
C. diversa	ZIM2110	Must, Dolenjska, SI

* SI = Slovenia; IT = Italy